FIRST-PRINCIPLES STRAIN ANALYSIS OF ATOMICALLY-THIN ELECTRENE MATERIALS

by

Ethan Gysbertsen

Submitted in partial fulfillment of the requirements
for the degree of Master of Science

at

Dalhousie University
Halifax, Nova Scotia
December 2023

Table of Contents

List of Tables

List of Figures

Abstract

Electrides are ionically bonded materials that have delocalized electrons serving as anions. When electrides have a layered crystal form, the electrons are confined within the 2D gaps between the atomic layers and operate as high-mobility, low-scattering charge carriers with remarkably low work functions. The atomically-thin form of layered electrides, called electrenes, retain these 2D electron gas-like states at the surface and interlayer regions.

In this work, density functional theory is used to explore if the conduction properties and work functions of monolayer and bilayer electrenes can be improved using biaxial strain loading, up to ±5%. The electron transport characteristics are indirectly examined by calculating the state density of electrons near the Fermi level, and the average distance of surface states from the atomic lattice, $\langle z \rangle$, to approximate the electron-phonon coupling. The electrenes of interest are those from the alkaline earth sub-pnictogenide family of inorganic layered electrenes: Ca_2N, Sr_2N, Sr_2P, Ba_2N, Ba_2P, Ba_2As, and Ba_2Sb.

The manipulation of electronic states in electrenes is found to be highly variable, with some electrenes experiencing minimal changes, while others see a definitive increase in state density near the Fermi level, mostly originating from near the edge of the Brillouin zone. The biggest improvement is in monolayer Ba_2N, where surface state density increases by 56% under 2% compressive strain. However, state density and $\langle z \rangle$ do not necessarily correlate, so low electron-phonon coupling of these states is not guaranteed. The bilayer electrenes show the largest $\langle z \rangle$ and the most variation with strain. Bilayer Ba_2Sb is expected to have the lowest electron-phonon coupling with a $\langle z \rangle$ of 2.2 Å at 5% tensile strain. Work function sees a consistent reduction in all cases under tensile strain, with bilayer electrenes having lower values than their monolayer counterparts. The lowest work function value observed in bilayer Ba_2Sb, which starts at 2.38 eV when unstrained, and drops to 2.24 eV under 5% tensile strain. These findings indicate that strain can be used to manipulate and enhance the electronic transport properties of electrenes.

Chapter 1

Introduction

In ionically bonded materials, atoms transfer electrons to fill their respective valence shells, and this leaves the atoms with net opposing charges. Cations are atoms which have donated electrons and anions are those atoms which accept electrons. The traditional example is NaCl. Na is an alkali metal and has one valence electron, and chlorine is a halogen with one vacancy in its valence shell. When the electron is transferred between them, it leaves Na with a positive charge and Cl with a negative charge ($[\mathrm{Na}]^+$, $[\mathrm{Cl}]^-$). The resulting polarization due to this electron distribution induces an electrostatic attraction between ions which is the source of the bonding in the material. This is the simplest model of ionic bonding and it holds when the excess number of electrons in the donating atoms match the required electrons in the valence shells of the receiving atoms.

However, there are cases where the material has a surplus of donated electrons that cannot be taken up by the anions. It then becomes possible for these excess electrons to spill out from the cation and fill whatever empty space is available in the atomic lattice, and thereby act as the anion. Such materials with anionic electrons are called electrides, and are of great interest for their electrical properties [2, 3]. Electrides are classified based on the dimensionality of the space the anionic electrons occupy. Zero-dimensional (0D) electrides have electrons surrounded on all sides by the lattice, and are localized to that region in the material. One-dimensional (1D) electrides means there are channels present in the lattice that allow the electrons to occupy the length of the channel and move freely along it. Two-dimensional (2D) electrides confine the electrons in only one direction, allowing them to move freely in a plane.

The first ever confirmed 2D electride, the ionic crystal $\mathrm{Ca_2N}$, was reported by Lee et al. in 2013 [4]. Calcium is an alkaline earth metal with two s-orbital valence electrons, while nitrogen is able to accept three electrons in its p-orbital valence shell. By the stoichiometry of the compound, this leads to nitrogen taking three of the four electrons donated by the two calcium atoms, leaving one remaining to serve as the anionic electron; $[Ca_2N]^+{\cdot}e^-$. Because Ca_2N is a layered material, comprised of 3-atom thick atomic slabs (with a thickness of 2.5 Å) separated by 3.9 Å of interstitial space, the excess electron fills this interlayer space. As a result, the atomic slabs act as the cation and the interlayer electrons act as the anion.

Figure 1.1 shows the atomic structure and electron density of Ca_2N. Also shown is the band structure of bulk Ca_2N representing the electron eigenstates, where a single band crosses the Fermi level; this band corresponds to the interlayer states.

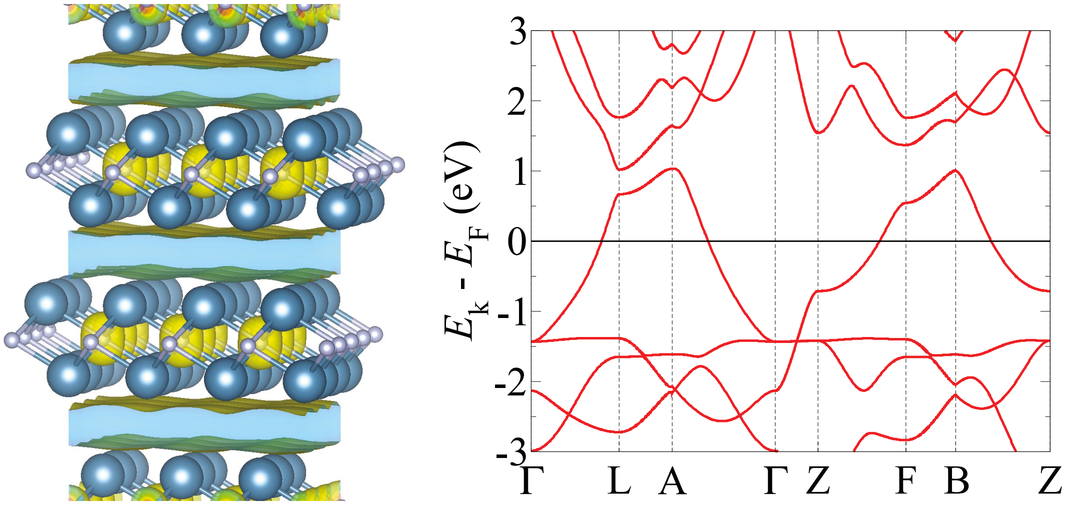

Figure 1.1: Atomic lattice with overlaid electron density (left) and band structure (right) of Ca_2N. Electron density in calculated for an energy range from $E_F - 1$ eV to E_F. These first-principles results are courtesy of Dr. Vahid Askarpour.

In this study, the authors confirmed the single-crystal phase of their Ca_2N sample and from electrical measurements determined that it is a highly conductive metal. At room temperature it had a resistivity of 2.8 $\mu\Omega$cm, which is smaller than that of pure calcium metal (3.6 $\mu\Omega$cm) and similar to aluminium (2.7 $\mu\Omega$cm). Hall effect measurements found that the electron mobility was 160 $cm^2V^{-1}s^{-1}$ at 300 K with a carrier concentration of $1.39{\times}10^{22}$ cm^{-3}, and that mobility increases to 520 $cm^2V^{-1}s^{-1}$ at a low temperature of 2 K. These mobility values are many times larger than that of common metals, which are often in the tens of $cm^2V^{-1}s^{-1}$. The higher mobility of Ca_2N is believed to arise from low electron-phonon coupling, originating from how the conducting interlayer electrons are spatially separated from the lattice and thus less sensitive to atomic motion.

From the low-temperature transport properties, the mean scattering time and mean free path are calculated to be 0.6 ps and 120 nm. According to the authors, these large values, which are similar to those observed in 2D electronic systems, is evidence that conduction in Ca_2N is mainly by the interlayer anionic electrons.

The paper also reports on the work function of Ca_2N in both a single crystal and polycrystalline pellets determined using ultraviolet photoelectron spectroscopy (UPS). The work function was found to be anisotropic due to the confinement of the free carriers in the interstitial region between the atomic layers. The measured out-of-plane and in-plane work functions are 3.5 eV and 2.6 eV, respectively. This is in agreement with the ab initio calculations of a previous study [5]. The in-plane work function is very low compared to other metals, which typically have values above 4 eV, owing to the loosely-bound nature of the electrons at the Fermi level.

The second confirmed 2D electride to be synthesized was polycrystalline Y_2C in 2014 [6]. It has the same crystal structure as Ca_2N, but possesses a different stoichiometric arrangement. Yttrium is a transition metal with three valence electrons (2 s-orbital, 1 d-orbital) while carbon requires four electrons to fill its p-shell, meaning that the chemical formula for the ionic electride should be $[Y_2C]^{2+}\cdot 2e^-$. What the study found however was that unlike Ca_2N, a first-principles calculation predicted that while the anionic electrons do generally reside in the interstitial region between the atomic planes, they also extend into the lattice and do not form a continuous uniform 2D sheet of charge in the interlayer, as is seen in Ca_2N. As a result, the chemical formula was deemed closer to $[Y_2C]^{1.8+}\cdot 1.8e^-$.

Polycrystalline Y_2C has a resistivity of 217 $\mu\Omega$cm at 300 K, a value comparable to polycrystalline Ca_2N [4], though it is characterized as a semi-metal. The study doesn't report the mean free path or scattering time, but it does conclude that the effective mass of charge carriers (6.2 m_e for electrons) is much greater than that reported for Ca_2N, which in the 2013 paper was found to be 1.9 m_e or 2.5 m_e, depending on the method of measurement, where m_e is the mass of an electron in free space. The study also reports the electron-phonon coupling constant of Y_2C, a dimensionless metric that describes the average strength of the electron-phonon coupling. The study gives a coupling constant of λ=0.21 for Y_2C.

The work function of polycrystalline Y_2C was determined using UPS to be 2.9 eV, while calculations performed using density functional theory (DFT) found an out-of-plane work function of 3.72 eV. Single crystal Y_2C has since been synthesized [7] and it was found to have a carrier concentration of around 1.25×10^{22} cm^{-3}, about the same as single crystal Ca_2N (1.39×10^{22} cm^{-3}), and an electron mobility of 0.8 cm^{2}V^{-1}s^{-1}, which is two hundred times less than that of Ca_2N (160 cm^{2}V^{-1}s^{-1}). In all regards it seems that Y_2C is second to Ca_2N as both an electron source and a conductive material, but a distinctive feature of Y_2C is that it is paramagnetic in polycrystalline form, and expected to be ferromagnetic when in single crystal form [8]. The study that synthesized the single crystal Y_2C didn't report ferromagnetism, but did observe an anisotropic magnetization that favored the out-of-plane direction [7].

Since the discovery of 2D electrides, there have been numerous high-throughput studies attempting to find new electrides with improved transport properties and even lower work functions. These studies used computational methods to search for thermodynamically stable forms of layered electrides by seeking to model materials with unbalanced oxidation numbers.

The starting point was tests of materials similar to Ca_2N, drawing from the same families of elements to see if electride behavior was reproducible in heavier elements with similar valence shells. Calculations predicted that Sr_2N and Ba_2N were also electrides [9] (Ca_2N, Sr_2N, and Ba_2N had all been previously synthesized as stable materials [10]), and so then large batches of possible compounds were analyzed, eventually revealing Sr_2P, Ba_2P, and Ba_2As were all 2D electrides like Ca_2N [11]. Layered electrides of this type were called alkaline earth sub-pnictogenides.

Y_2C was initially predicted to be a layered electride in an early version of one of these studies along with several other materials, including Gd_2C, Tb_2C, Dy_2C, Ho_2C, and Er_2C [12]. The paper established a new family of layered inorganic electrides called the layered rare earth sub-carbides. All but Y_2C were predicted to be ferromagnetic by the computational paper, and in fact Gd_2C, Tb_2C, Dy_2C, and Ho_2C had all been synthesized and confirmed to be ferromagnetic by experiment before they'd been identified as electrides [13, 14, 15]. The weaker magnetic properties of Y_2C seems to be due to yttrium being a transition metal, as the other carbide materials are composed of lanthanoids. In 2020, Gd_2C was synthesized as a single crystal, and like Y_2C, it's anionic electrons were shown to be more localized than in Ca_2N [16].

As computational studies continued, a third family of electrides was discovered called the alkaline earth monofluorides. This family has the form MF, with the three initial members being CaF, SrF, and BaF. These materials have a slightly different crystal structure than the alkaline earth sub-pnictogenides and the rare earth sub-carbides, and they are more difficult to study as they are less energetically favorable than MF_2. Though calculations pointed to the possibility of metastability, no samples of an alkaline earth monofluoride have been synthesized to date [11]. Calculated electron density maps indicate that these materials have anionic electron distribution more similar to alkaline earth sub-pnictogenides rather than the rare earth sub-carbides, as their interlayer states are more delocalized from the cations and better contained between the atomic slabs [17].

Since the three initial electride families were identified, high-throughput computational searches have discovered hundreds of electride candidate materials [18, 19]. Moreover, recent computational screening methods have lead to the discovery and synthesis of a semiconducting electride, Sc_2C, with a theoretically calculated 0.305 eV indirect band gap and 0.476 eV direct band gap [20]. As more discoveries are made, the parameters for these computational searches changes to accommodate new forms of electride crystals, which lead to further discoveries.

A major step in the advancement of electride research was the synthysis of atomically thin samples of Ca_2N in 2016 [21]. It's commonly understood that nanoscale materials can develop properties that do not appear in their bulk counterparts; for example, MoS_2 is an indirect band gap semiconductor, but when its thickness is reduced down to a monolayer it becomes a direct band gap semiconductor [22]. Thus, the demonstration of few-layer Ca_2N creates the opportunity for new and unique electronic characteristics. Following the common lexicon of 2D materials study, the 2D versions of electrides were dubbed electrenes.

We note there can be confusion about terminology in the literature, since it can be unclear whether a 2D electride is referring to a layered bulk electride with 2D confined electrons or an electride of nanoscale thickness. To avoid any ambiguity, in this thesis "electride" is reserved for the bulk crystal and "electrene" is reserved for the few-layer material.

Due to Ca_2N's large interlayer distance and relatively low cleavage energy [4, 23], it was an obvious choice for exfoliation of single or few layers. Several computational studies had previously predicted the existence of a monolayer Ca_2N [23, 24] and made predictions about its electrical properties, but it wasn't until the 2016 study that an experimental sample had been exfoliated. Those studies predicted that in the absence of contained interlayer regions, the anionic electrons of the electride would reside on the surfaces of the material, and the experimental results support this with confirmation of a metallic, crystalline nature which preserves the delocalized anionic electrons.

The presence of the electron gas environment on the surface of the material makes electrenes highly reactive, and only stable in a nitrogen atmosphere or immersed in an organic solvent. Even then, the exfoliation and handling process leaves the material prone to oxidation [21]. This is a limitation it shares with bulk electrides, though its readiness as an electron donor opens up applications as a catalyst material for desired reactions, an application for which electrides are already being considered [25].

Possibly due to the difficulty in handling and preserving them, there are no other experimental studies of alkaline earth sub-pnictogenide electrenes to date, though many theoretical studies have been performed to identify candidates and determine their properties. From the alkaline earth sub-pnictogenides family of electrides, the following have been theoretically confirmed as stable: Ca_2N, Sr_2N, Sr_2P, Ba_2N, Ba_2P, Ba_2As, Ba_2Sb [24, 26, 1].

A key feature in the electrical structure of the alkaline earth sub-pnictogenide electrenes is the presence of two partially-filled conduction bands that cross the Fermi level (see Fig. 1.2). These bands are associated with the anionic electron gas states on the surfaces of the material [23, 24]. These surface state bands have different energies due to the interaction between the top and bottom surfaces [27]. In the case of a bilayer electrene, instead of a monolayer, a third lower-energy band cuts through the Fermi level, which is associated with the 2D delocalized anionic electron states confined to the interstitial region between the two atomic slabs. As more atomic layers are added, each will introduce an additional interlayer band, and the two surface bands will eventually become degenerate as the distance between the top and bottom surfaces increases and their interaction decreases [24].

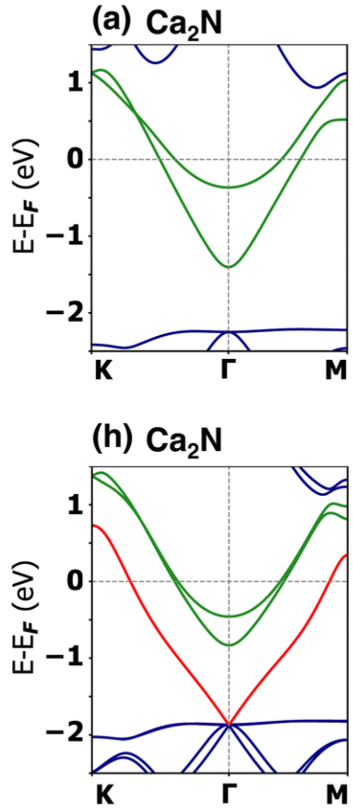

Figure 1.2: Band structure of monolayer (top) and bilayer (bottom) Ca_2N with Fermi level set to 0 eV [1].

A computational study by Zeng et al. [28] investigated the theoretical electron-phonon coupling and carrier mobility of monolayer Ca_2N. As would be expected for delocalized electrons, the electron-phonon coupling matrix elements were found to be small compared to common metals and graphene, though this conflicted with the electron-phonon coupling constant of λ=0.78 they determined, which was high compared to ordinary metals.

The electron mobility of monolayer Ca_2N was calculated to be 189 $cm^2V^{-1}s^{-1}$ at 300 K, which is an improvment on the mobility of bulk at room temperature (160 $cm^2V^{-1}s^{-1}$ [4]). The mobility is greater than that of common metals, but is still strikingly lower than the mobility of graphene under ambient conditions (5000-15000 $cm^2V^{-1}s^{-1}$ [29]). This was attributed to higher electron velocities for graphene, despite the higher scattering rate. The carrier concentration of monolayer Ca_2N was calculated to be 8.93×10^{14} cm^{-2}, but if the electron density could be reduced to 1.33×10^{14} cm^{-2}, thereby moving the Fermi level towards the bottom of the surface band, the mobility could climb up to 3000 $cm^2V^{-1}s^{-1}$ at 300 K [28].

The work function of monolayer electrenes have been found to be slightly higher than bulk electrides along the out-of-plane direction. With Ca_2N, bulk has a measured work function of 3.5 eV [4], while the value for monolayer has been calculated to be just above 3.6 eV [24]. Monolayer Sr_2N has a lower work function between 3.3 eV and 3.4 eV, indicating the electrons are more loosely bound, but it and monolayer Ca_2N see a drop in work function as further layers are added [24, 1]. As another example, the calculated work function of monolayer Gd_2C starts at 3.43 eV and converges towards a value of 3.35 eV at five layers [30]. Conversely, the computational study Liu et al. determined an out-of-plane work function for monolayer Gd_2C of 3.75 eV [17]. Interestingly, this study demonstrates that there is a strong correlation between the binding energy between layers of the electrides and the work function, a feature they establish is not present in van der Waals materials. The study also demonstrated that the difference between the in-plane and the out-of-plane work function of a monolayer is fairly consistent, with the average difference being 0.78 eV over twelve different electrene materials from each of the three main families of electrides. As a final observation, the work function of alkaline earth sub-pnictogenides and monofluorides decreases as the mass of the alkaline earth metal increased, and the work function of all sub-pnictogenide compounds is lower than their corresponding monofluoride compounds in monolayer.

Their high conductivity along with their low work functions makes electrides and electrenes attractive for a variety of potential applications. Their possible use as a catalyst has been previously mentioned, but the loosely bound electrons would also make it a prime reducing agent [31] or solid-state dopant in nanoscale or 2D materials [32, 33]. Work has also focused on using electrides as an electron injection layer for thin-film transistors in driving organic light-emitting diodes [34]. Computations have been performed looking at Ca_2N and Sr_2N monolayer as anode materials in Na-ion batteries with strong results coming from Ca_2N due to its high specific capacity, metallic character, fast Na diffusion, and good cycling stability [35].

The use of 2D semiconductors in transistors is impeded by the high metal–semiconductor interface resistance due to the lack of dangling bonds in the out-of-plane direction. To reduce the contact resistance, first-principles studies are looking at creating heterostructures by inserting a layered electride, such as Ca_2N, at the interface to act as an electron-rich ohmic contact and reduce the potential barrier. Initial results indicate electride surface states disappear and get donated to the metal and semiconductor, thereby lowering the potential barrier and enabling an Ohmic contact [36].

One of the most unique uses of electride materials is as a transparent conductor [37]. It has been established that Ca_2N has high electron mobility, low phonon scattering, long mean free paths, and high carrier concentrations, but another avenue of active study is the optical properties of electride and electrene materials. Experimental tests of few layer Ca_2N found that a 10 nm-tick film would transmit 97% of light [4]. Thus, electrenes could find applications in which both high conductivity and high optical transmission are needed.

The process of searching for stable electrenes with desirable electrical properties is a time consuming endevour, and so it would be beneficial to find a way of altering the known electrenes so as to achieve better performance. A common and very effective method of controlling the properties of 2D materials is strain engineering. Strain engineering alters the lattice structure of a material, and unlike bulk materials, 2D materials can withstand much greater strain values without structural failure. In the case of graphene, a relative strain value of up to 25% can be applied before material failure [38, 39].

The alteration of the atomic structure in this way can produce drastic changes in a material's electronic structure due to the alteration in bonding distances and orbital overlap. This can allow for fine tuning of electrical properties like the magnitude of a semiconductor band gap by about $\sim$70 meV per strain percent [40], or induce transitions from an indirect to a direct band gap [41]. Strain loading can also alter a material's phonon vibrational modes [42] and decrease effective carrier mass by up to 16% for electrons, or by nearly 80% for electron holes with 6% tensile or compressive strain respectively [43, 44].

Given how readily the anionic electrons of an electrene conform to the arrangement of the atomic lattice, the strain response of electride materials could be of great importance to their properties and performance. The layered electride Mg_2N shows how dramatic strain effects can be. Unlike other alkaline earth metal nitrides, Mg_2N

is both a 0D electride, a recently discovered semiconducting electride [45], and has fewer anionic electrons than is typical with $[Mg_2N]^{0.45+}\cdot 0.45e^-$. When applying strain along the out-of-plane direction, the material starts as a semiconductor, and then transitions to a conductor with 2% tensile strain. Not only that, at 5% strain, tensile or compressive, Mg_2N becomes a 2D electride, although the pressure required to achieve these strain values is on the order of gigapascals [46].

As another example, Pereira et al. [47] reports that Mo_2N monolayer becomes an eletrene at low temperatures, and manipulating strain allows for control of the electron-phonon coupling constant, going from $\lambda \approx 1.9$ to $\lambda \approx 1.2$ at 2% tensile strain. Strain loading also allows for control of the critical temperature at which superconduction occurs, with values changing from 19.3 K to 24.8 K. Similar coupling response to strain has been calculated for the electride MgONa, where the electron-phonon coupling was reduced from 0.82 to around 0.75 under 2.5% compressive strain [48].

A computational study by Mortazavi et al. [49] reports on the conductivity response of monolayer Ca_2N and Sr_2N to uniaxial strain, and finds that tensile strain reduces the current response of the material up to between $\sim$14% and $\sim$24%, while compressive strain increases the current. The authors attribute this change to compressive strain increasing the overlap of atomic orbitals in the material while tensile strain induces localization of the orbitals. They find that the peaks in the electrostatic potential increase with tensile strain, which is interpreted as increasing electron scattering. Conversely, a decrease in the peak values of the electrostatic potential with compressive strain is believed to result in lower scattering. A study on the superconducting properties of monolayer Ba_2N demonstrates a potentially similar conductance relation to strain, with a reduction of the electron-phonon coupling constant with compressive strain from its unstrained value of 0.59 to around 0.45 with -2% biaxial strain [50].

These studies provide an indication of the response that can be expected from 2D electrenes, but there are other types of electrene materials which have not been studied and other desirable properties that have not been explored. It is the goal of this work to investigate, using first-principles modeling, how strain influences the elctronic characteristics of seven 2D electrenes that are part of the alkaline earth subpnictogenide family (Ca_2N, Sr_2N, Sr_2P, Ba_2N, Ba_2P, Ba_2As, Ba_2Sb). The range of explored strain values will be limited to ±5% due to the unknown structural failure point of the materials in question; previous computational study places the failure of monolayer Ba_2N at 5% tensile strain, so exploration beyond this point would not produce practical results [50]. A particular interest is focused on whether strain could be used to modulate the transport properties and the electron-phonon coupling of the anionic electrons, in addition to these material's ability to act as electron donors.

Chapter 2

Theoretical and Computational Approach

2.1 Lattice Structure and Band Theory

2.1.1 Periodic Lattice for Real and Reciprocal Space

All the materials examined in this thesis are crystalline solids, meaning their atomic structure forms a periodic lattice defined by the lattice vectors $\mathbf{R} = n_1\mathbf{a_1}+n_2\mathbf{a_2}+n_3\mathbf{a_3}$, where $\mathbf{a_i}$ are the primitive lattice vectors and n_i are integers. The region defined by the primitive lattice vectors is called the primitive cell and contains the unique atomic environment that is repeated to form the periodic lattice. Starting from the position of the atoms in the primitive cell, the position of eVery other atom in the crystal is given by a linear combination of $\mathbf{a_1}$, $\mathbf{a_2}$ and $\mathbf{a_3}$.

While the primitive lattice vectors are unique, there is no unique way of defining the primitive cell. However, one common definition is the Wigner-Seitz cell. It is defined as all the volume in the lattice which is closer to point $\mathbf{R} = 0$ than any other point on the lattice, bordered by planes that orthogonaly transect the midway point between $\mathbf{R} = 0$ and its adjacent lattice points. Translating this volume by every lattice vector $\mathbf{R}$ will perfectly tile the lattice space without overlap or gaps.

For any structure which is periodic in real space, that structure will also have periodic behavior in reciprocal $\mathbf{k}$-space. $\mathbf{k}$ here represents the wavevectors of electronic states, which will be examined later on. To introduce reciprocal space, we examine the properties of a periodic function. A continuous periodic function representing some observable quantity on the lattice will by necessity have the property $f(\mathbf{r}) = f(\mathbf{r}+\mathbf{R})$, and can be represented in a Fourier expansion over a set of wavevectors $\mathbf{G}$,

$$f(\mathbf{r}) = \sum_{\mathbf{G}} c_{\mathbf{G}} e^{i\mathbf{r}\cdot\mathbf{G}}. \tag{2.1}$$

These two principles taken together make it clear that the set of wavevectors $\mathbf{G}$ must follow the constraint

$$e^{i\mathbf{R}\cdot\mathbf{G}} = 1. \tag{2.2}$$

Much like the direct lattice, all the points $\mathbf{G}$ are determined by the translation $\mathbf{G} = m_1\mathbf{b_1} + m_2\mathbf{b_2} + m_3\mathbf{b_3}$, where $\mathbf{b_i}$ are the primitive reciprocal lattice vectors and m_i are integers. The vectors $\mathbf{b_i}$ can be constructed via the primitive vector relation $\mathbf{a_i} \cdot \mathbf{b_j} = 2\pi\delta_{ij}$, which is satisfied by defining the vectors $\mathbf{b_i}$ in the following way:

$$\mathbf{b_1} = \frac{2\pi\mathbf{a_2} \times \mathbf{a_3}}{\mathbf{a_1} \cdot (\mathbf{a_2} \times \mathbf{a_3})}, \quad \mathbf{b_2} = \frac{2\pi\mathbf{a_3} \times \mathbf{a_1}}{\mathbf{a_1} \cdot (\mathbf{a_2} \times \mathbf{a_3})}, \quad \mathbf{b_3} = \frac{2\pi\mathbf{a_1} \times \mathbf{a_2}}{\mathbf{a_1} \cdot (\mathbf{a_2} \times \mathbf{a_3})}. \tag{2.3}$$

With this definition of $\mathbf{G}$ and $\mathbf{b_i}$, it can be shown that Eq. 2.2 is always satisfied. These vectors define a periodic space referred to as $\mathbf{k}$-space or reciprocal space, and behave analogously to the $\mathbf{R}$ and $\mathbf{a_i}$ vectors in real space.

When the Wigner-Seitz cell is constructed for the reciprocal lattice in $\mathbf{k}$-space, it is referred to as the Brillouin zone. The Brillouin zone is very useful in the analysis of crystalline materials as many quantities of interest arise from summing over all the $\mathbf{k}$ states in the Brillouin zone, as will be shown later.

The value of $\mathbf{k}$ is quantized by the size of the material due to the boundary conditions, which impose that only integer multiples of the fundamental wavelength are allowed. This condition limits the possible values for the components of $\mathbf{k}$ to $k_i = \frac{2\pi}{L_i}n_i$, where L_i is the material length along direction i and n is an integer. However, given that L_i is typically much greater than the size of the primitive lattice vector $\mathbf{a_i}$, the allowed values of k_i have a difference much smaller than the length of the reciprocal lattice vector $b_i = \frac{2\pi}{a_i}$, and so the value of $\mathbf{k}$ can be treated as effectively continuous. This simplifies the analysis of the material properties and is valid so long as the total size of the material is much greater than that of the primitive lattice vectors.

2.1.2 Blöch's Theorem

Having established the principles of the atomic lattice, we turn to describing the electron states that exist in a periodic potential. Such states will conform to Schrödinger's equation,

$$\left[-\frac{\hbar^2}{2m_e}\nabla^2 + V(\mathbf{r})\right]\psi_{\mathbf{k}}(\mathbf{r}) = E_{\mathbf{k}}\psi_{\mathbf{k}}(\mathbf{r}), \tag{2.4}$$

where $\psi_{\mathbf{k}}$ is the wavefunction for an electron with wavevector $\mathbf{k}$ and $E_{\mathbf{k}}$ is the eigenenergy of that state. The term in brackets is the Hamiltonian in which the first term is the operator for the kinetic energy and $V(r)$ is a potential acting on the electron.

In 1929, the physicist Felix Blöch [51] demonstrated how the wavefunction solution to the Schrödinger equation in a periodic potential will have the form,

$$\psi_{\mathbf{k}}(\mathbf{r}) = u_{\mathbf{k}}(\mathbf{r})e^{i\mathbf{k}\cdot\mathbf{r}}, \tag{2.5}$$

where $e^{i\mathbf{k}\cdot\mathbf{r}}$ is a plane wave with wavevector $\mathbf{k}$ and $u_{\mathbf{k}}(\mathbf{r})$ is a function with the same spatial periodicity as the lattice, i.e. $u_{\mathbf{k}}(\mathbf{r}) = u_{\mathbf{k}}(\mathbf{r}+\mathbf{R})$. These modified plane wave solutions make up the possible single-electron states for the material.

For a free electron, the wavefunction is just a plane wave $e^{i\mathbf{k}\cdot\mathbf{r}}$ with $u_{\mathbf{k}}(\mathbf{r}) = 1$. In this case the momentum of the electron is directly proportional to the wavevector $\mathbf{k}$ as the momentum operator $\mathbf{p} = \frac{\hbar}{i}\nabla$ returns,

$$\mathbf{p}\psi_{\mathbf{k}} = \frac{\hbar}{i}\nabla e^{i\mathbf{k}\cdot\mathbf{r}} = \frac{\hbar}{i}(i\mathbf{k})e^{i\mathbf{k}\cdot\mathbf{r}} = \hbar\mathbf{k}\psi_{\mathbf{k}}, \tag{2.6}$$

meaning that the expectation value for the momentum of a plane wave is $\hbar\mathbf{k}$.

For a Blöch wave function this is no longer the case, since the Blöch solutions are not eigenstates of the momentum operator,

$$\mathbf{p}\psi_{\mathbf{k}} = \frac{\hbar}{i}\nabla(u_{\mathbf{k}}(\mathbf{r})e^{i\mathbf{k}\cdot\mathbf{r}}) = \frac{\hbar}{i}[(i\mathbf{k})u_{\mathbf{k}}(\mathbf{r})e^{i\mathbf{k}\cdot\mathbf{r}} + e^{i\mathbf{k}\cdot\mathbf{r}}\nabla u_{\mathbf{k}}(\mathbf{r})] = \hbar\mathbf{k}\psi_{\mathbf{k}} + \frac{\hbar}{i}e^{i\mathbf{k}\cdot\mathbf{r}}\nabla u_{\mathbf{k}}(\mathbf{r}). \tag{2.7}$$

Instead, $\hbar\mathbf{k}$ is called the crystal momentum as, similar to the true momentum, it possesses useful conservation laws that limit how electrons can transition between states when interacting with an external potential.

It can be shown that the wavefunction and eigenenergy are insensitive to translations of $\mathbf{G}$, i.e. $\psi_{\mathbf{k}} = \psi_{\mathbf{k}+\mathbf{G}}$ and $E_{\mathbf{k}} = E_{\mathbf{k}+\mathbf{G}}$. It is therefore convenient to take all $\mathbf{k}$-points and fold them into the first Brillouin zone, which is allowable due to the equivalence of all $\mathbf{k}$-points separated by $\mathbf{G}$. This sort of representation is known as the reduced zone scheme, and simplifies problems involving the reciprocal lattice as we only need focus on the first Brillouin zone.

Every $\mathbf{k}$-point in the Brillouin zone will have multiple eigenenergies, and so they must be indexed by the band number n. The group of states that share a band index are referred to as a band and are discrete over $\mathbf{k}$-space due to the quantization of $\mathbf{k}$. The unique set of states defined inside the first Brillouin zone is called the band structure, and due to the equivalence of $\psi_{\mathbf{k}} = \psi_{\mathbf{k}+\mathbf{G}}$ and $E_{\mathbf{k}} = E_{\mathbf{k}+\mathbf{G}}$, is periodic over reciprocal space.

Since $\mathbf{k}$ need only be defined over the Brillouin zone, the number of quantized states is limited by the reciprocal lattice vector $b_i = \frac{2\pi}{a_i}$ in direction i. Given that $L_i = N_i a_i$, where N_i is the number of unit cells in direction i, the components of $\mathbf{k}$ will equal the reciprocal lattice vectors at $k_i = \frac{2\pi}{L_i} N_i$. Since the discrete $\mathbf{k}$-points have a spacing of $dk_i = \frac{2\pi}{L_i}$, the number of $\mathbf{k}$-states in a band is therefore equal to the number of unit cells that are in the whole material. As this number grows, the bands begin to behave as if they are continuous.

The band structure of a material will have gaps along the energy spectrum in which there exist no eigenenergy states and so no bands. These gaps play a major role in determining the electrical properties of a material depending on how difficult it is for electrons to occupy higher energy bands. A conductor will have the Fermi level of the material cross a band; since the band is partially filled, there are many electrons that can contribute to conduction under an applied potential. Insulators have their Fermi level in a band gap, so the highest energy band with filled states is entirely filled, and a large energy is needed to excite the electrons to the next higher energy (conduction) band. If the Fermi level is in the band gap, but the band gap is less than roughly 3 eV, such materials are semiconductors.

The behavior of the electrons is determined by the shape of the band they occupy. The group velocity for a state is given by

$$\mathbf{v}_{\mathbf{k}} = \frac{\nabla_{\mathbf{k}} E(\mathbf{k})}{\hbar}, \tag{2.8}$$

and the effective mass of that state is given by the tensor

$$\frac{1}{m^*_{ij}(\mathbf{k})} = \frac{1}{\hbar^2} \frac{\delta^2 E(\mathbf{k})}{\delta k_i \delta k_j}. \tag{2.9}$$

This simplifies for a free electron which has a purely quadratic shape in $\mathbf{k}$-space,

$$E(\mathbf{k}) = \frac{\hbar^2 k^2}{2m_0}, \tag{2.10}$$

and serves as a good approximation for the extrema of bands of a semiconductor,

$$\mathbf{v}_{\mathbf{k}} = \frac{\hbar(\mathbf{k} - \mathbf{k}_{min})}{m^*(\mathbf{k})}, \tag{2.11}$$

where $\mathbf{k}_{min}$ is the location of the band minimum.

2.2 Density Functional Theory

2.2.1 Kohn-Sham Equation

Solving the many-body Schrödinger equation for the N electrons in the material would be incredibly difficult to tackle as each electron would add 3 degrees of freedom to the many-body wavefunction $\Psi(\mathbf{r_1}, \mathbf{r_2}, \mathbf{r_3}, ..., \mathbf{r_N})$. A methodology must be used to reduce the problem to a manageable size, and such an approach begins with the Hohenberg-Kohn theorem from 1964 [52]. What this theorem proves is that for an interacting, non-relativistic electronic system in an external potential, the ground-state energy of that system is uniquely defined by the ground-state density of the system, $n(\mathbf{r})$. This greatly simplifies the problem as it now only requires we solve for the 3-dimensional density function, which minimizes the energy rather than a $3N$-dimensional many-body wavefunction.

Hohenberg and Kohn define the form of the energy functional, in atomic units, as,

$$E[n(\mathbf{r})] = \int v(\mathbf{r})n(\mathbf{r})d\mathbf{r} + \frac{1}{2}\int \frac{n(\mathbf{r})n(\mathbf{r}')}{|\mathbf{r}-\mathbf{r}'|}d\mathbf{r}d\mathbf{r}' + T[n(\mathbf{r})] + E_{XC}[n(\mathbf{r})], \tag{2.12}$$

where the first two terms represent the classical electrostatic energy of the ion-electron and electron-electron interactions, where $v(\mathbf{r})$ is the ionic potential. The third and fourth terms represent the kinetic energy and the quantum exchange-correlation energy which accounts for quantum and many-body interactions. Neither of these two functionals have a known form in terms of $n(\mathbf{r})$, and without knowing what these functionals are the ground state density can't be determined exactly.

In 1965, an approximation was provided for these functionals by Kohn and Sham [53]. They make the assumption that the density of the system is the sum of the occupied single-particle states,

$$n(\mathbf{r}) = \sum_{i=1}^{N} |\psi_i(\mathbf{r})|^2. \tag{2.13}$$

By minimizing $E[n(\mathbf{r})]$ with respect to the states ψ_i, Kohn and Sham showed that the solutions ψ_i must obey a single-particle Schrödinger equation known as the Kohn-Sham equation

$$\left[-\frac{\nabla^2}{2} + v_{KS}[n(\mathbf{r})]\right]\psi_i(\mathbf{r}) = E_i\psi_i(\mathbf{r}), \tag{2.14}$$

where the electrons are taken to be non-interacting, subject only to the effective potential

$$v_{KS}[n(\mathbf{r})] = v(\mathbf{r}) + \int \frac{n(\mathbf{r}')}{|\mathbf{r}-\mathbf{r}'|}dr' + \frac{\delta E_{XC}[n(\mathbf{r})]}{\delta n(\mathbf{r})}. \tag{2.15}$$

The kinetic energy functional is approximated as simply the sum of kinetic energies of the occupied single-particle states,

$$\sum_{i=1}^{N}\left[-\frac{\nabla^2}{2}\psi_i(\mathbf{r})\right] = \sum_{i=1}^{N} E_{k,i}\psi_i(\mathbf{r}). \tag{2.16}$$

The exchange-correlation energy is still unknown, but the effective potential due to the exchange-correlation effect is given by

$$v_{XC}[n(\mathbf{r})] = \frac{\delta E_{XC}[n(\mathbf{r})]}{\delta n(\mathbf{r})}. \tag{2.17}$$

Density Functional Theory (DFT) looks to solve the Kohn-Sham equations using iterative computational methods. Due to the dependence of the Kohn-Sham Hamiltonian on the solution ψ_i via the density $n(\mathbf{r})$, the problem requires a self-consistent solution approach. This is done numerically by starting with a guess of the density $n_0(\mathbf{r})$, and then refining this solution with each iteration to within a certain error of the actual value. From this initial guess the Hamiltonian is calculated and is used to solve the Kohn-Sham equation for ψ_i. The solution is then used to determine the new density $n_1(\mathbf{r})$, and if the density is self-consistent within a defined threshold, the iterative process concludes and $n_1(\mathbf{r})$ is used to calculate the properties of the material. If the solution is not self-consistent, the density is updated and the process is repeated until convergence is reached.

This study uses the DFT code QUANTUM ESPRESSO [54] to model materials. QE has a variety of functionalities, the primary one being the aforementioned self-consistency calculation for solving the Kohn-Sham equations. It uses a modified Broyden method for updating $n(\mathbf{r})$ at each iteration, as described above [54, 55]. DFT is also able to calculate the inter-atomic forces [56] and stresses [57] acting on the atoms. By minimizing the energy due to these forces, the code can find the optimal atomic positions and lattice vectors using the Broyden-Fletcher-Goldfarb-Shanno (BFGS) algorithm [54].

The exchange-correlation energy still has no known exact form, and so an approximation must be made. The local density approximation (LDA) takes the energy density $\epsilon_{XC}[n(\mathbf{r})]$, the exchange-correlation energy per particle, to be that of a homogeneous electron gas. LDA works best for materials where $n(\mathbf{r})$ is largly uniform like in simple metals, but generally causes over-binding where the bonding strength of the atomic lattice is larger than it should be, leading to shortened lattice constants and bonding distances [58]. Alternatives to LDA take into account the spatial non-uniformity of the charge density. The generalized gradient approximation (GGA) does this by including the density gradient in the exchange-correlation density, $\epsilon_{XC}^{GGA}[n(\mathbf{r}), \nabla n(\mathbf{r})]$. GGA's do not have the same overbinding problem as LDA, but can overcorrect and lead to underbinding [59, 60]. Another alternative is meta-generalized gradient approximation (meta-GGA) [61], which takes GGA a step further by including a dependence on higher order derivatives of the charge density, thereby capturing non-linear behavior.

All of these approximations are considered local functionals as they depend only on the electron density at or near the point at which they are evaluated, but there are ones that include non-local effects. Hybrid functionals include exact exchange integrals from Hartree-Fock theory involving multiple wavefunctions [62], which is far more computationally intense than the previous approximations, but has far greater accuracy at predicting electronic properties like band gaps. This study uses a GGA established by Perdew, Burke and Ernzerhof (PBE) [60], which has both a low computational demand and resonable accuracy, in combination with a van der Waals model for determining accurate atomic structures.

2.2.2 van der Waals Correction

When calculating the optimal atomic structure of a material, it is important to include a correction for the van der Waals (vdW) interation. vdW forces occur due to a transient induced polarization between atoms in proximity to each other, causing a momentary attraction. It is a comparatively weak force, but becomes more relevant for 2D materials where the interlayer bonding isn't very strong. vdW corrections are absent from standard XC functionals as they are a non-local effect. XC functionals corrected to include non-local behavior are called van der Waals density functionals (vdW-DF), and while they offer much higher accuracy than purely local XC functionals, they require far more computational operations [63].

There are a number of vdW corrections that are semi-empirical and use predetermined pairwise dispersion coefficients, C_{AB}, for a given pair of atoms A and B. Such methods generally have a two-body dispersion energy correction of the form,

$$E_{\text{disp}} = \sum_{A,B} \sum_{n=6,8,10\ldots} s_n \frac{C_{AB,n}}{r_{AB}^n} f_n(r_{AB}), \tag{2.18}$$

where n is the order of the dispersion term, r_{AB} is the distance between the atoms A and B, s_n is a scaling factor, and $f_n(r_{AB})$ is a damping function that prevents divergences at small r_{AB} [64, 65, 66].

One correction of this type is the exchange-hole dipole moment (XDM) model [65]. The central assumption of this model is the attribution of the transient vdW dipole moments to the quantum effect of the exchange hole caused by the Pauli exclusion principle. The exchange hole is a decrease in the probability of finding identical electrons in vicinity of one another. This drop in the wavefunction magnitude around other electrons forms a dipole moment, which causes a dispersion interaction with nearby atoms. Using this theory, XDM precalculates its dispersion coefficients to use in its vdW correction [67].

The most common way of accounting for vdW is the semi-empirical Grimme's dispersion-corrected DFT (DFT-D). It is widely used due to its numerical simplicity, and its broad applicability to a variety of chemical environments and XC functionals. This study uses the third version of this model, DFT-D3, with two-body contributions only. This version of DFT-D manages to reduce the empirical components of the method, primarily by using a first-principles approach to determine dispersion coefficients $C_{AB,n}$, and cut-off radii for the damping function f_n, where dispersion order only goes to $n = 8$ [64]. In this work, the Becke-Johnson damping scheme is used due to its improvements on calculation accuracy [68].

2.2.3 k-point Sampling and Smearing

Many quantities of interest require an integration over all **k**-states in the Brillouin zone, including the charge density $n(\mathbf{r})$ during the self-consistent calculations of the Kohn-Sham equation. In practice these integrations are done numerically as a sum over a uniform **k**-point grid. This grid is generated using the Monkhorst-Pack scheme [69],

$$\mathbf{k}_{prs} = u_p\mathbf{b_1} + u_r\mathbf{b_2} + u_s\mathbf{b_3}, \tag{2.19}$$

where $\mathbf{b_i}$ are the reciprocal lattice vectors, and u_a are sequences of numbers determined by,

$$u_a = (2a - q_i - 1)/2q_i \quad (a = 1, 2, 3, ..., q_i). \tag{2.20}$$

This scheme creates a uniform **k**-mesh along each reciprocal lattice vector, confined to the Brillouin zone.

The accuracy of this **k**-point sampling method increases with the number of **k**-points, the final grid containing a total of $q_1 \cdot q_2 \cdot q_3$ uniformly spaced points. The computation is further expedited by exploiting the symmetries of the Brillouin zone, which possesses the same symmetries as the atomic lattice. By determining the portion of the Brillouin zone that is unique under these symmetries, called the irreducible Brillouin zone, the integration need only be performed for those irreducible **k**-points.

When doing **k**-space integrals on metals, as is done in this study, it is important to consider the fact that DFT calculations are performed at absolute zero, meaning there is an abrupt cut-off between occupied and unoccupied states in the middle of the band. This discontinuity requires a high number of **k**-points to properly sample, which increases the computational load. A smearing approximation smooths out the electron population when transitioning from occupied to unoccupied states near the Fermi level. In this study Marzari-Vanderbilt cold smearing is used for atomic structure optimization and self-consistent electronic calculations, where the discontinuity is modeled by a Gaussian function multiplied by a first order polynomial [70]. For DOS calculations, the tetrahedron method with Blöchl corrections [71] is used as it provides better accuracy for these particular calculations.

2.2.4 Basis Set

When solving the Kohn-Sham equations numerically, the eigenfunctions ψ_i are almost always represented as a linear combination of some basis set functions. One of the simplest basis sets is a linear combination of atomic orbitals (LCAO), which consists of a linear combination of energetically relevant atomic orbitals over every atom in the unit cell [72]. Compared to more generalized basis sets, LCAO requires far fewer basis functions and so is an efficient method that produces accurate results, but requires attention to selecting and optimizing the proper functions for the system as seeking convergence can lead to overcompleteness [73].

Other localized basis sets include Gaussian type orbitals (GTO), which are much more efficient to calculate. However, GTOs are too dissimilar from the form of the Schrödinger solution for atomic orbitals, being both differentiable at $r = 0$ and decaying too quickly in r. What is used instead of a pure Gaussian then is a linear combination of Gaussians to approximate a Slater type orbital (STO), which has a much more accurate functional form but no analytic solution to XC integrals. Given that the number of primitive Gaussians in each basis function increases the complexity of the calculation, there is a significant trade off between speed and accuracy when using GTO in this way. The number of Gaussians used must therefore be carefully considered, the general convention being three as the optimum number of Gaussian functions [74].

One common basis set used in DFT, and the one used in this work, is a plane wave basis, which takes maximal advantage of the periodic behavior of the atomic lattice. Because the periodic portion of the Blöch wavefunction (Eq. 2.5), $u_{n,\mathbf{k}}(\mathbf{r})$, shares the periodicity of the lattice, it can be represented as a Fourier sum over the reciprocal lattice vectors $\mathbf{G}$,

$$u_{n,\mathbf{k}}(\mathbf{r}) = \sum_{\mathbf{G}} c_{n,\mathbf{k},\mathbf{G}} e^{i\mathbf{G}\cdot\mathbf{r}}, \tag{2.21}$$

where $c_{n,\mathbf{k},\mathbf{G}}$ are the Fourier coefficients that depend on n, $\mathbf{k}$ and $\mathbf{G}$. This gives the Blöch wavefunction the form

$$\psi_{n,\mathbf{k}}(\mathbf{r}) = \sum_{\mathbf{G}} c_{n,\mathbf{k},\mathbf{G}} e^{i(\mathbf{G}+\mathbf{k})\cdot\mathbf{r}}. \tag{2.22}$$

This series is theoretically infinite since the reciprocal lattice vectors extend indefinitely, but in practice the sum is truncated to a finite number of terms. Large $\mathbf{G}$ vectors beyond some cutoff point are removed as large $\mathbf{G}$ vectors correspond to a plane wave with a small wavelength, and by removing these components from the expansion, the spatial resolution of the wavefunction is reduced. Since the wavevector $\mathbf{k}$ determines the energy of a plane wave, this cut off point is usually specified as some energy value,

$$E_{\text{cut}} \geq \frac{\hbar^2|\mathbf{k}+\mathbf{G}|^2}{2m_e}. \tag{2.23}$$

By using a convergent series like the plane wave basis, it ensures that increasing the number of terms in the series returns greater accuracy, but requires comparatively more terms than other basis sets. QUANTUM ESPRESSO is a code that uses a plane wave basis set, and so this is the basis set adopted in this study.

2.2.5 Pseudopotentials

There are difficulties that arise with a plane wave basis, since rapid oscillations in ψ_i require many more Fourier terms in the basis expansion. Such rapid oscillatory behavior occurs in excited eigenfunctions, where ψ_i is confined in an external potential well like that very near to the atomic nucleus, and so an approximation is needed to reduce the size of the basis set. Additionally, the atomic potential of the ions in the crystal lattice are of a very simple form, proportional to the inverse of the radial distance, but this simple form causes numerical difficulties due to a singularity at $r = 0$.

The pseudopotential approximation solves both of these issues by taking advantage of the fact that only the valence electrons of the atoms are involved in chemical bonding. The core electrons are inert and screen out the Coulomb potential of the ions, so the effects of both the core electrons and the ions can be combined into a single pseudopotential acting on the valence electrons. This eliminates the singularity of the ion potential and promotes the valence electrons to be the lowest energy eigenstates. These states have a smooth behavior suitable for a plane wave expansion.

Generating an accurate pseudopotential requires adhering to several restrictions, the first of which was described by Topp and Hopfield in 1973 [75]. This restriction requires that after a specified cut-off radius r_c, which delineates between valence and core, the wave function solution must match the solution of the true potential. Further constraints are that the solution must conserve the charge density for r less than r_c, called norm-conservation, and its eigenenergies must match the true eigenenergies. Lastly, the resulting pseudopotential must match both the true potential beyond r_c, and match its scattering behavior. Using the Schrödinger equation, the pseudopotential can be back-solved based on the pseudo-wavefunction that adheres to these constraints.

The desirable features sought in a pseudopotential approximation are accurate transferability across different chemical environments, and softness in the eigensolutions that reduces the number of plane waves needed to represent them. In pursuit of these criteria, all the pseduopotentials used in this study are ultra-soft pseudopotentials (USP) taken from the QUANTUM ESPRESSO library [76]. For USP, the norm-conservation of the charge density in the core is disregarded to produce a pseudopotential that can be constructed from as few plane waves as possible. This of course causes a charge deficit in the core region which must be accounted for by augmenting the electron density $n(\mathbf{r})$ during the self-consistent calculations with a term set to vanish beyond a given radius. The result is that the pseudopotential has much more accurate behavior in the valence electrons across different chemical environments, all while using a smaller plane wave basis set [77].

Chapter 3

Results

In this chapter, we investigate seven electrene materials that obey the formula M_2X in monolayer and bilayer form using DFT, where M is an alkaline earth metal and X is a pnictogen. These materials are Ca_2N, Sr_2N, Sr_2P, Ba_2N, Ba_2P, Ba_2As, and Ba_2Sb.

The focus of this study is on the effect of in-plane strain placed on the electrenes. All materials have therefore been calculated with various strain loads of up to ±5%, which was achieved by modifying the in-plane lattice constant. An atomic position optimization calculation was then run holding the lattice constants fixed to their strain values. This will show what effect strain has on the electrical properties of electrene materials as calculated from first principles.

We begin by presenting the results of the convergence tests to establish the value of the DFT calculation parameters that provide acceptable accuracy. Afterwards, we present the results of the unstrained monolayer and bilayer Ca_2N, in order to provide a baseline for comparison with literature and other electrenes. Then in a brief aside, the unique properties of electrenes will be compared to another metallic 2D material, to illustrate the differences between electrenes and traditional metals. The effects of strain will then be examined in monolayer and bilayer Ca_2N to make an initial assessment of the material's responses before moving on to compare the strain results of all materials to determine if any patterns arise that show potential for improving electron transport properties.

3.1 Convergence of DFT Calculation Parameters

There are three principle parameters that control the precision of calculations done in Quantum Espresso. The first is discussed above in section 2.2.4 and limits the spatial resolution of the Blöch wavefunctions by truncating the basis set used to construct them. Since the basis set is comprised of plane waves with increasing wavevectors,

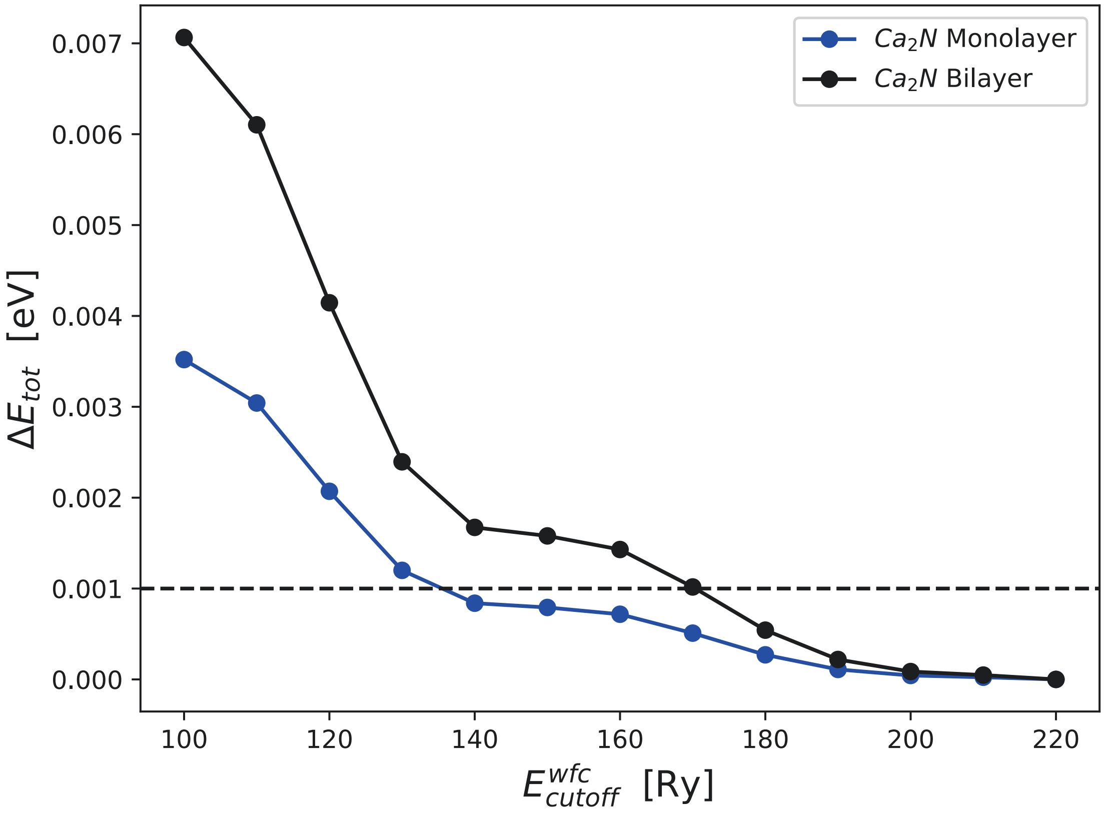

Figure 3.1: Convergence of total energy with respect to the wave function cutoff energy parameter, $E^{\mathrm{wfc}}_{\mathrm{cutoff}}$, for monolayer and bilayer $\mathrm{Ca_2N}$. The convergence threshold is set to 1 meV.

higher order terms correspond to finer spatial resolution of the wavefunctions, such that the accuracy is improved when additional terms of the expansion are included. The cutoff for the truncation is expressed as an energy $E^{\mathrm{wfc}}_{\mathrm{cutoff}}$ as shown in Eq. 2.23, with a larger energy cutoff corresponding to more terms included in the plane wave expansion.

To determine what constitutes an acceptable value for the calculation parameters, a series of self-consistent DFT total energy calculations are performed by varying the value of one calculation parameter. Once the total energy is within a set accuracy limit, in this case 1 meV, that parameter value is adopted.

Figure 3.1 shows the convergence test of the electrene material $\mathrm{Ca_2N}$ in both its monolayer and bilayer forms for the wavefunction energy cutoff $E^{\mathrm{wfc}}_{\mathrm{cutoff}}$, where the total energy is displayed as the absolute difference relative to the highest cutoff value. The

	Ca_2N	**Sr_2N**	**Sr_2N**	**Ba_2N**	**Ba_2P**	**Ba_2As**	**Ba_2Sb**
Monolayer	150	160	150	140	110	140	160
Bilayer	180	180	180	150	150	150	160

Table 3.1: Converged $E_{\text{cutoff}}^{\text{wfc}}$ parameter for all electrenes, reported in Rydbergs [Ry].

monolayer material converges to within the chosen limit between 130 Ry and 140 Ry, and levels off just under the limit between 140 Ry and 160 Ry. From this, the value of $E_{\text{cutoff}}^{\text{wfc}}$ was chosen to be 150 Ry. The bilayer material comes under the limit just after 170 Ry, so the cutoff value for bilayer was chosen to be 180 Ry. The chosen value of $E_{\text{cutoff}}^{\text{wfc}}$ for all materials, using the same procedure, is shown in Table. 3.1.

The second calculation parameter tested for convergence is $E_{\text{cutoff}}^{\text{rho}}$. This parameter is similar to the first in that it limits the spatial resolution of the charge density by truncating the plane wave basis. The charge density is derived from the norm

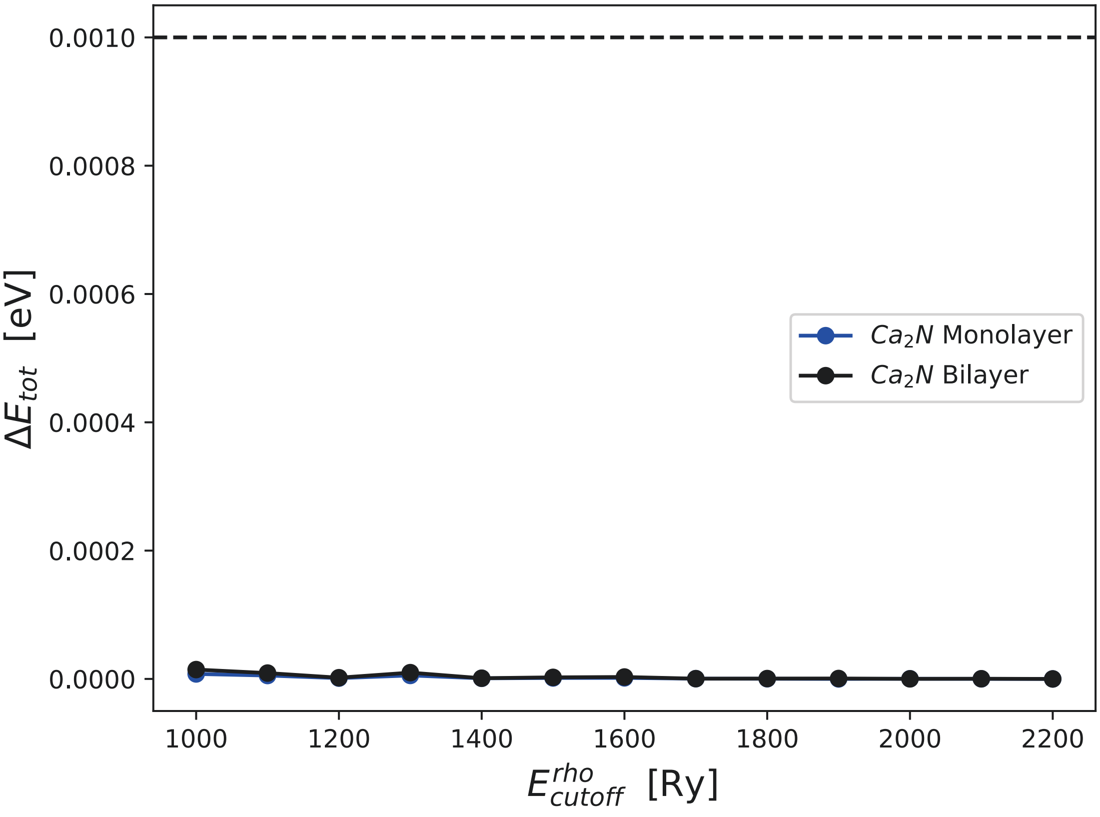

Figure 3.2: Convergence of total energy with respect to the charge density cutoff energy, $E_{\text{cutoff}}^{\text{rho}}$, for monolayer and bilayer Ca_2N. The convergence threshold is set to 1 meV.

	Ca_2N	Sr_2N	Sr_2N	Ba_2N	Ba_2P	Ba_2As	Ba_2Sb
Monolayer	1800	1800	1600	1700	1600	1600	1700
Bilayer	1800	1800	1900	1800	1600	1700	1600

Table 3.2: Converged $E_{\text{cutoff}}^{\text{rho}}$ parameter for all electrenes in Ry.

squared of the wavefunction, and thus can contain higher frequency components which require a different energy cutoff. Moreover, since these calculations use ultra-soft pseudopotentials, there is also an augmentation term applied to the charge density to account for the charge deficit in the core region due to the non-norm-conservation of USP (section 2.2.5). Since this deficit is in the core region, the augmentation contains the high-oscillation components of the charge density, and thus requires higher order terms to represent in the plane wave basis.

The convergence graph of $E_{\text{cutoff}}^{\text{rho}}$ for Ca_2N (Fig. 3.2) falls entirely below the convergence limit, so by this metric any value of $E_{\text{cutoff}}^{\text{rho}}$ would be acceptable, but to limit the choice, the convention of $\sim 10 E_{\text{cutoff}}^{\text{wfc}}$ is adhered to. The cutoff value for both monolayer and bilayer is chosen to be 1800 Ry.

The final calculation parameter is the density of the **k**-point grid used to sample the Brillouin zone (section 2.2.3). Since calculations will be done for 2D materials, the only wavevector components of interest are those in the xy-plane (i.e. in plane), so the **k**-mesh used to sample **k**-space will also be a 2D plane.

The number of grid points along each reciprocal lattice vector determines the grid density, with an increasing number leading to higher resolution of **k**-space. To ensure a grid sampling point falls on the high-symmetry Γ point located at the origin of **k**-space, the number of grid points along each direction is limited to odd numbers. Figure 3.3 shows the convergence of the total energy with increasing $k \times k$ point count for Ca_2N monolayer and bilayer. The selected values for **k**-point density for all electrenes are shown in Table 3.3. Note that more stringent **k**-point densities, over the minimum set by the total energy threshold, were adopted for improved accuracy.

These computations use a PBE GGA for the exchange-correlation energy [60] and Grimme's DFT-D3 with two-body contributions and Becke-Johnson damping scheme for van der Waals correction [64, 68]. The **k**-point sampling grid is generated using the Monkhorst-Pack scheme [69]. Marzari-Vanderbilt cold smearing [70] is used for atomic structure optimizations and self-consistent electronic calculations to

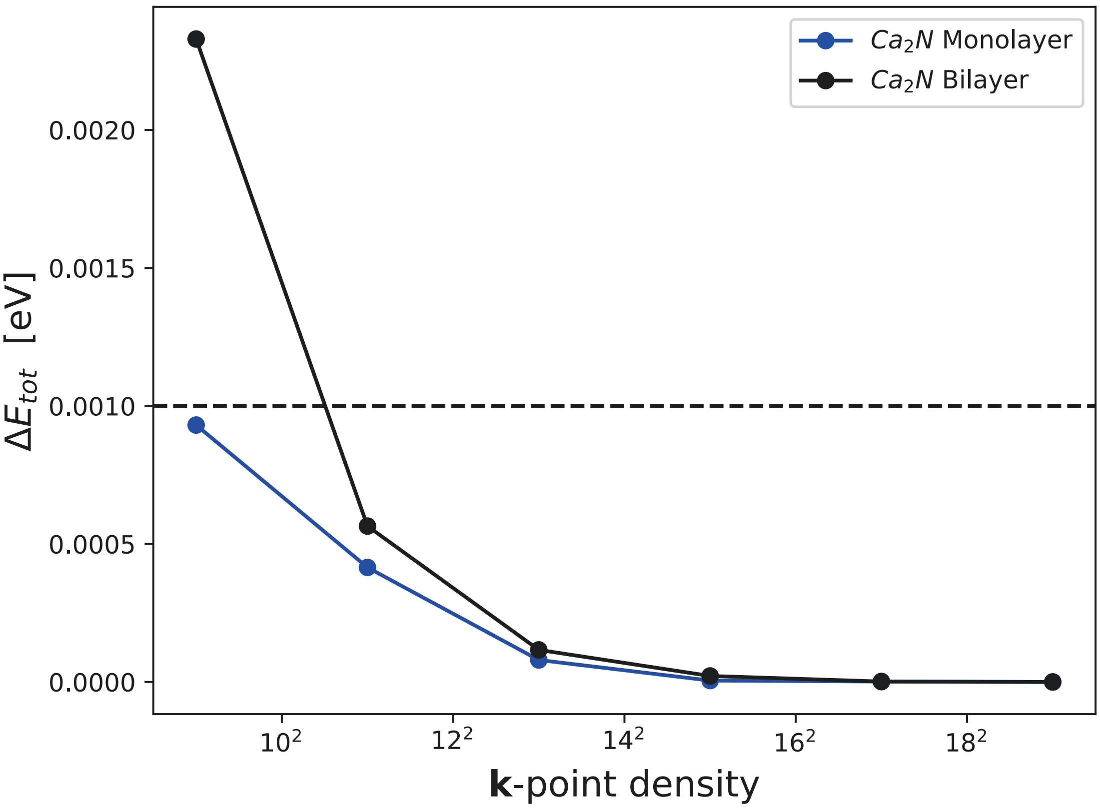

Figure 3.3: Convergence of total energy with respect to the **k**-point density for monolayer and bilayer Ca_2N. The convergence threshold is set to 1 meV.

account for state occupation discontinuities, while for DOS calculations, the tetrahedron method with Blöchl corrections is used [71]. A plane wave basis set is used with ultra-soft pseudopotentials, and energy and force thresholds of 10^{-5} a.u. for atomic and cell relaxation. At least 20 Å of vacuum is included in the cross plane direction during calculations to insure isolation of the atomic layers.

	Ca_2N	Sr_2N	Sr_2N	Ba_2N	Ba_2P	Ba_2As	Ba_2Sb
Monolayer	15^2	13^2	11^2	13^2	9^2	9^2	9^2
Bilayer	13^2	13^2	11^2	13^2	9^2	9^2	9^2

Table 3.3: Converged **k**-point density for all electrenes.

3.2 Unstrained Ca_2N Electrene

We begin by presenting the results of Ca_2N, which have been previously reported, to introduce the electrene properties and establish consensus with the scientific literature. All materials studied in this thesis have a hexagonal crystal structure with 3 atoms per primitive cell for monolayers and 6 atoms per primitive cell for the bilayers. The monolayer Ca_2N was found to have an in-plane lattice constant of $a = 3.584$ Å, which is consistent with the lattice constant value reported by other first-principles studies in the range 3.562-3.620 Å [23, 24, 49, 78]. The bilayer in-plane lattice constant is $a = 3.579$ Å, which is likewise similar to another first-principles result of 3.562 Å [24].

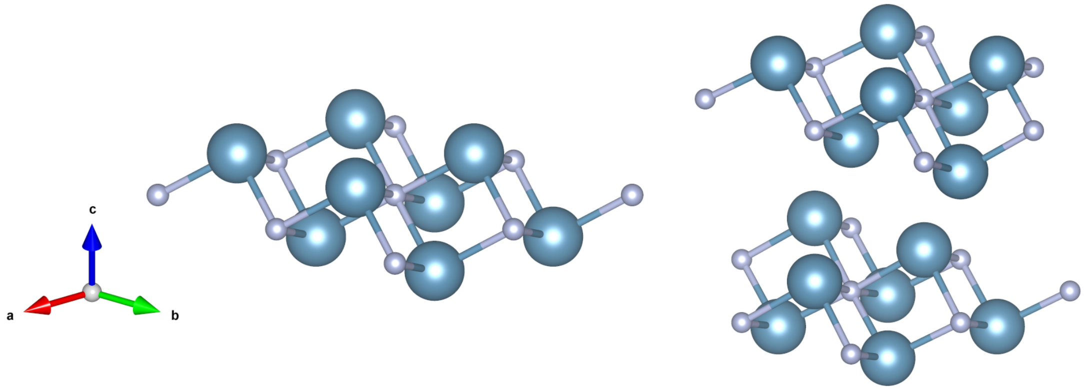

Figure 3.4: Atomic structure of monolayer (left) and bilayer (right) Ca_2N. Larger atoms are calcium, smaller atoms are nitrogen.

The determined layer thickness for monolayer and bilayer (shown in Table 3.4) agree well with literature values of 2.516 Å and 2.509 Å, respectively, as does the interlayer gap distance for bilayer (3.598 Å) [24]. Other sources indicate a monolayer thickness of 2.515 Å [78] and 2.52 Å [49], so clearly, variation in layer thickness is low.

Material	**a**	**c**	Layer thickness	Interlayer gap
Ca_2N Monolayer	3.584	29.998	2.518	
Ca_2N Bilayer	3.579	34.582	2.510	3.597

Table 3.4: Lattice parameters of Ca_2N. **a** and **c** are the in-plane and out-of-plane lattice constants and are measured in Angstroms, as are the single layer thickness and interlayer gap.

High-symmetry points of the Brillouin zone are labeled based on the type of crystal system it belongs to, and in doing so gives a standard by which reciprocal space can be navigated. By picking a path from point to point, the eigenenergies can be more easily visualized, which is referred to as the band structure or electron dispersion. Here we plot the band structure along the high-symmetry points displayed in Fig. 3.5.

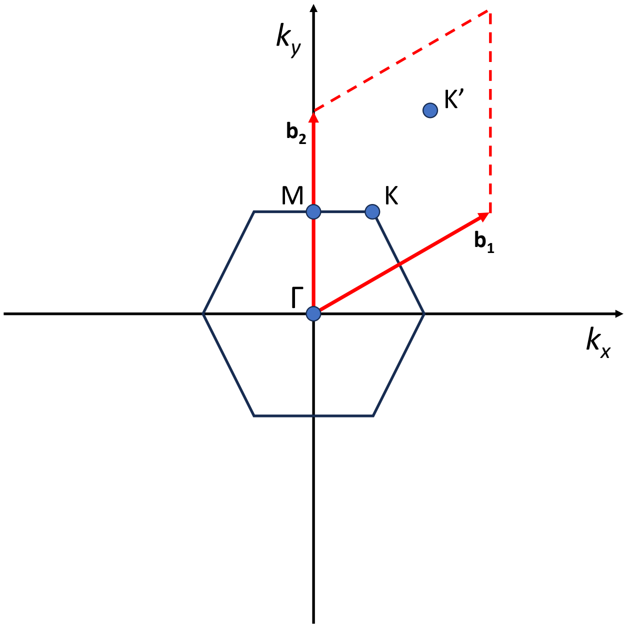

Figure 3.5: First Brillouin zone and reciprocal lattice vectors of monolayer Ca_2N. Displayed high-symmetry **k**-points are Γ, M and K.

The band structures of monolayer and bilayer Ca_2N are shown in Fig. 3.6. The two Fermi-crossing bands in Fig. 3.6a are associated with the 2D electron gas layers occupying the free-space regions of the material (2DEG-FS). Since the monolayer form only has two free-space regions, the surfaces above and below the atomic slab, the bands are associated with states in these regions. The third Fermi-crossing band that appears for bilayer (3.6c) appears due to the new free-space region in between the two atomic layers, so this band is associated with interlayer 2DEG-FS states. Since this region is essentially an overlap of two atomic surface regions, this band has energies deeper below the Fermi level and thus contains more electrons compared to a surface band.

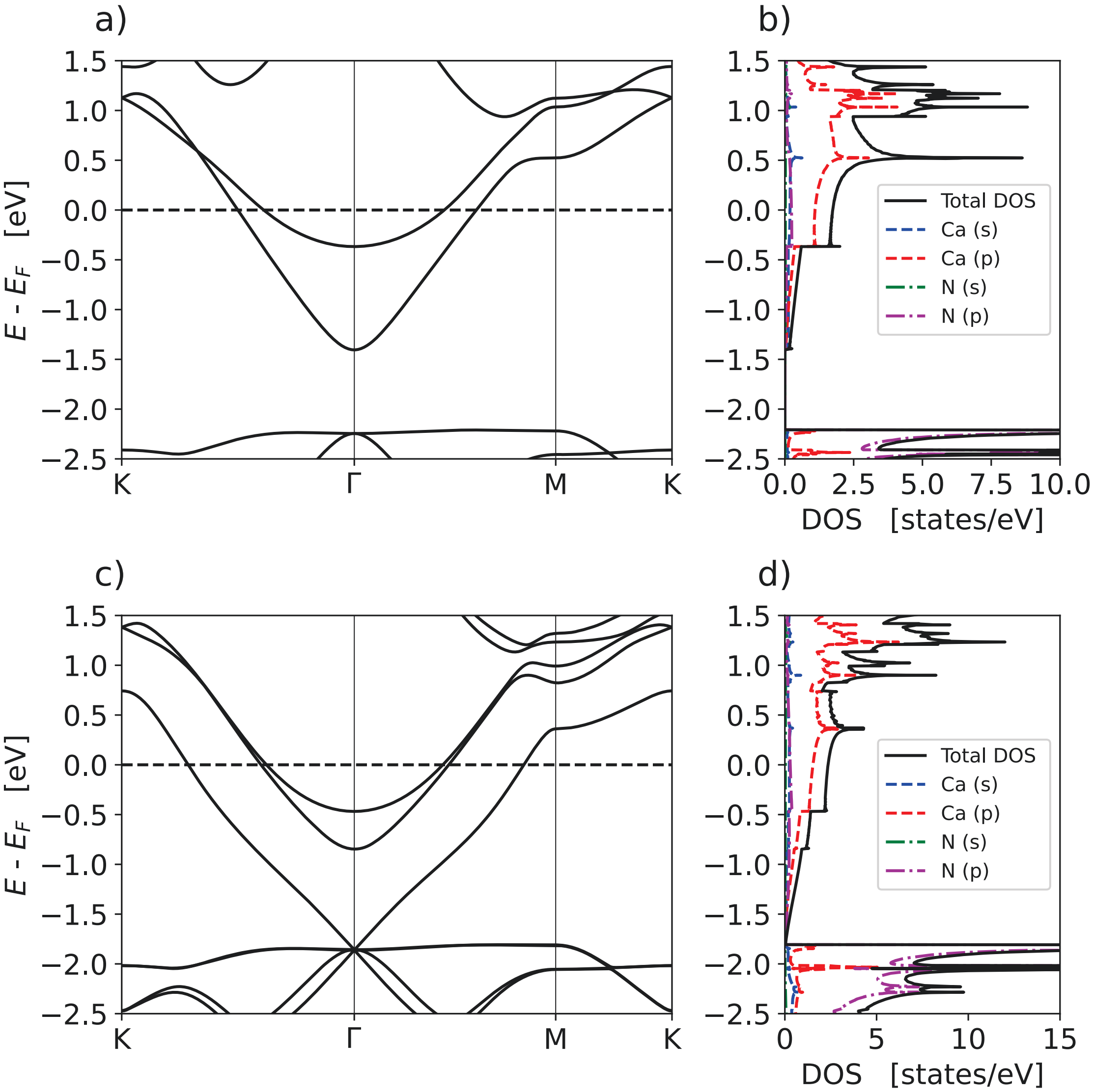

Figure 3.6: Band structure (a) and density of states (b) of monolayer Ca_2N. (c) Band structure and (d) density of states of bilayer Ca_2N. Density of states also includes the orbital projections. Zero on the energy scale corresponds to the Fermi energy.

The majority of existing literature for Ca_2N electrene is in agreement with these results [24, 78, 28, 21], though there is slight disagreement with the results of Zhao, Li, and Yang [23] on the energy of the monolayer surface bands. This seems to be due to a disagreement in calculated Fermi energy between studies, causing a consistent shift in the energy range of the band structure (an offset of about 0.25 eV). There is stronger disagreement with the monolayer band structure found by Mortazavi et. al. [49], particularly around and between the M and K points. In the Mortazavi et.

al. paper, bands seem to maintain strict order moving through this region, with no band crossings between -4eV and 4eV, where as this study found a great number of band crossings in the same range.

In addition to calculating the density of states (DOS), Quantum Espresso is also able to project the DOS onto the atomic orbitals to determine the DOS contributions of each orbital. This is referred to as the projected density of states (PDOS). Figure 3.6b,d shows the DOS of both monolayer and bilayer Ca_2N, and observing these figures make it clear how the DOS relates to the band structure of the material. Abrupt changes occur where new bands begin, and peaks occur where extant bands have a flatter character. Both increase the number of states in the energy range, but one increases it in a discrete manner while the other increases it gradually. Likewise, places where bands end show sudden drops in the DOS. Such behavior is expected for a 2D parabolic band (like that near the band minimum or maximum shown in Fig. 3.6a,c), which will contribute a step-function DOS [79].

The projected orbitals shown in the figure indicate that in the energy range around the Fermi level, the DOS is dominated by the calcium p orbital for both monolayer and bilayer. However, it should be noted that this type of orbital projection is not very effective at capturing all contributing states for electride-type materials. States that exist in the regions between the atomic layers and not in orbitals localized around the atoms of the material are under-represented in PDOS, with an earlier calculation of bulk Ca_2N needing to include a non-atom-centered orbital in the interlayer region in order to capture the state contributions. That calculation is in agreement with the results determined here, showing Ca dominated surface and interstitial states around the Fermi level, and N dominated states below the Fermi level (around -2 eV) [4].

Weighted **k**-points can be used to examine the orbital character of bands. The weighted **k**-points of Ca_2N monolayer and bilayer are shown in Fig. 3.7 and Fig. 3.8, and it is clear that the relative contribution of the orbitals change across the bands, indicating that the spatial distribution of states is changing. Near the Γ point, Ca s-orbitals are in higher proportion for the surface and interlayer bands, though the DOS in Fig. 3.6 indicates this is due to a reduction in p-orbital contribution rather than an increase in s-orbital strength. This agrees well with the **k**-resolved state densities shown in Appendix C, which demonstrates p-orbital bonding features at

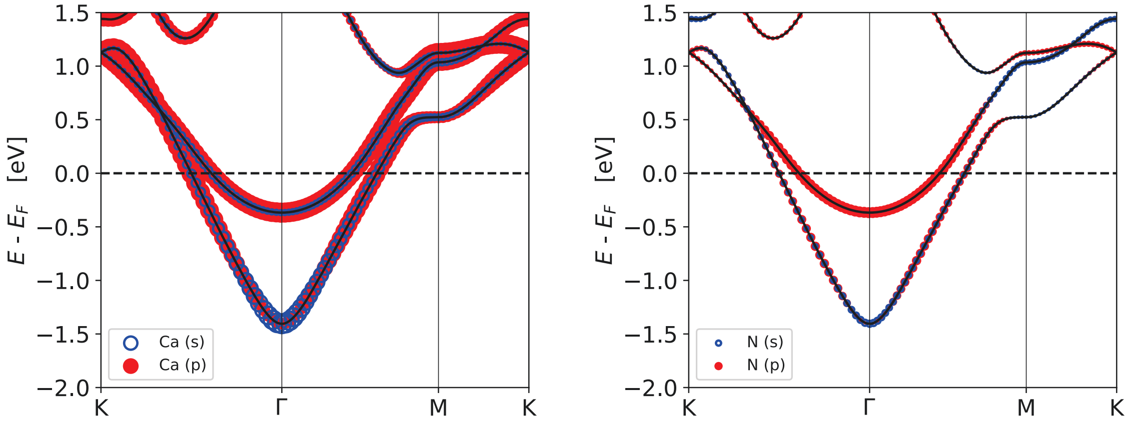

Figure 3.7: Weighted **k**-points of monolayer Ca_2N showing (left) calcium orbital contributions and (right) nitrogen orbital contributions..

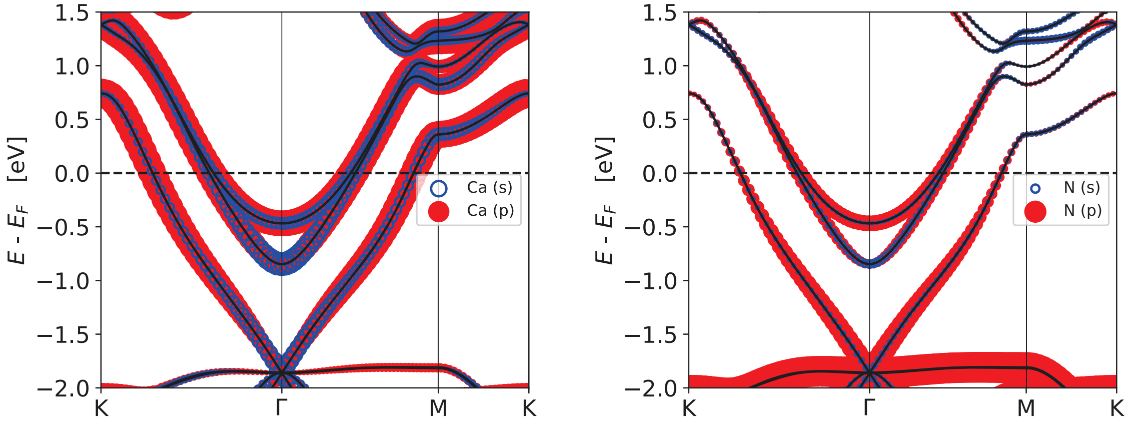

Figure 3.8: Weighted **k**-points of bilayer Ca_2N showing (left) calcium orbital contributions and (right) nitrogen orbital contributions.

the M point, indicating that Ca s-orbitals are more relevant to 2DEG-FS character, which is located predominantly at the Γ point. Bands below the Fermi level, at roughly -2 eV in bilayer Ca_2N, have a large N p-orbital contribution, which is in agreement with Fig. 3.6.

To gain further understanding of the electrical character of the individual bands, the **k**-resolved electron density can be determined for the specific state $\psi_{\mathbf{k},n}$. Figure 3.9 shows the results of this calculation for $\mathbf{k} = \Gamma$ in the case of Ca_2N bilayer, for all the bands between -2 eV and 0 eV. As is expected, the two highest energy bands (labeled a and b) display 2DEG-FS behavior and are located on the outer surfaces of the bilayer. The next lowest energy band (labeled e) is also a 2DEG-FS state

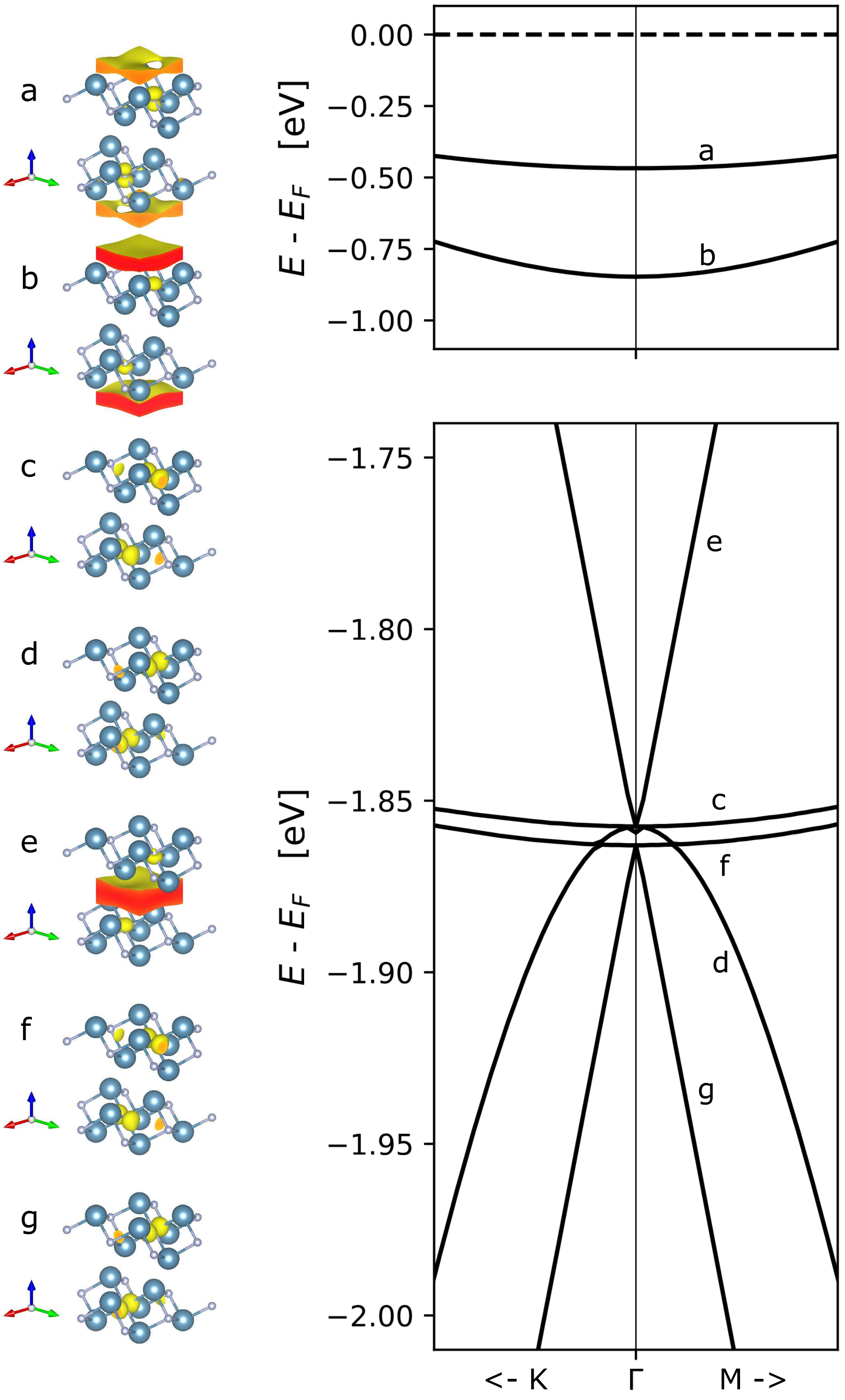

Figure 3.9: (Left) $|\psi_{\mathbf{k},n}|^2$ at $\mathbf{k} = \Gamma$ in the case of bilayer Ca_2N for each band between -2 eV and 0 eV. (Right) Zoomed-in band structure of bilayer Ca_2N.

and is concentrated in the interlayer region. All other calculated bands seem to be p orbitals of nitrogen, with at least partial p orbitals also appearing in the surface and interstitial bands. This is in agreement with the PDOS of bilayer which shows very high nitrogen p-orbital contribution in bands located roughly -2 eV below the Fermi level.

To get a quantified image of the spatial distribution of states, the integrated local density of states (ILDOS) modifies the DOS by the spatial density before integrating over a specified energy range:

$$ILDOS(\mathbf{r}) = \frac{2}{N_{\mathbf{k}}} \int_{E_1}^{E_2} \sum_{\mathbf{k},n} |\psi_{\mathbf{k},n}(\mathbf{r})|^2 \delta(E - E_{\mathbf{k},n}) dE, \tag{3.1}$$

where $N_{\mathbf{k}}$ is the number of $\mathbf{k}$-points in the Brillouin zone. For this study, all ILDOS were determined for the energy range ±0.1 eV around the Fermi energy, as this range is most relevant to the electron transport properties of the material.

Taking the planar average of the ILDOS returns the average distribution of states along the z-axis (out-of-plane direction) for the energy range $|E - E_F| \leq 0.1$eV, as shown for monolayer and bilayer Ca_2N in Fig. 3.10 and Fig. 3.11. It is clear from these figures that the major concentration of states exists outside the atomic layers

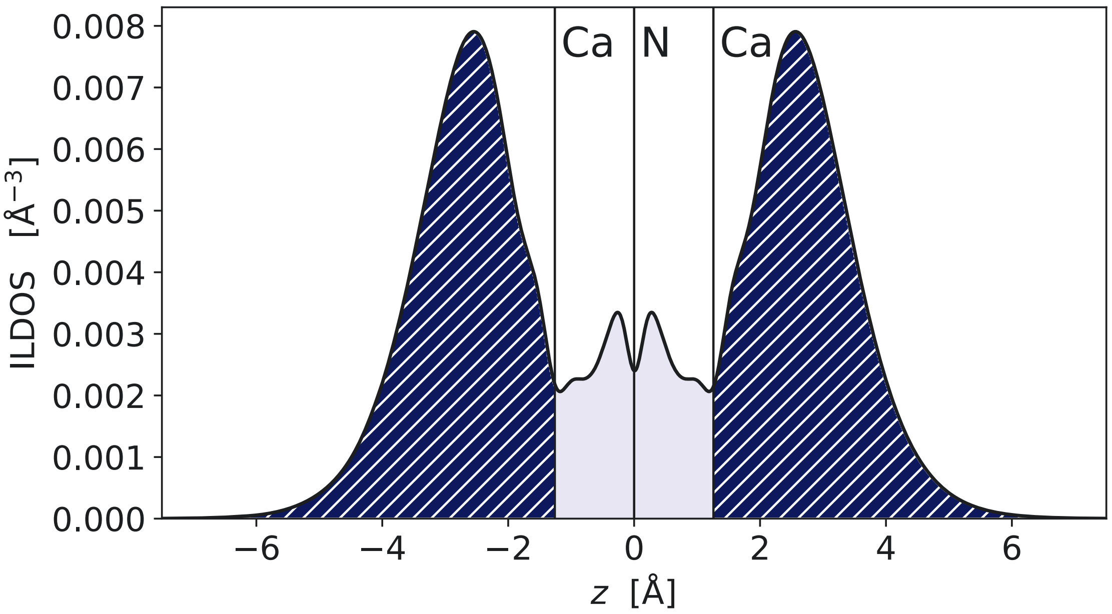

Figure 3.10: Planar average of the ILDOS for monolayer Ca_2N along the out-of-plane axis. Shaded regions on the surfaces are used to calculate the surface state density.

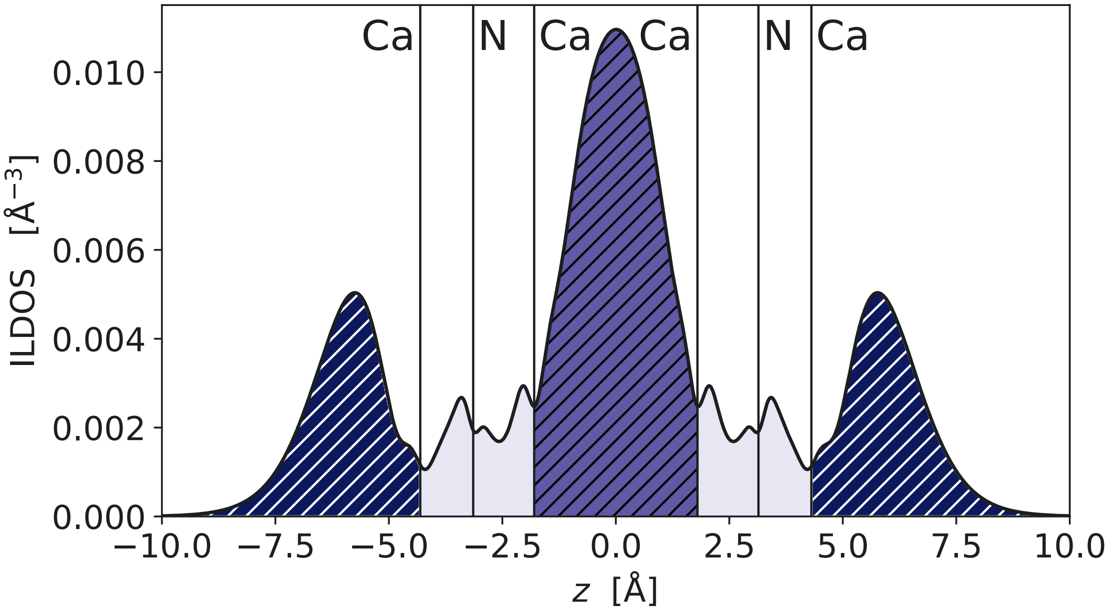

Figure 3.11: Planar average of the ILDOS for bilayer Ca_2N along the out-of-plane axis. Shaded areas on the surfaces and interstitial region are used to calculate the surface state density and interlayer state density, respectively.

on the surfaces and in the interstitial region for bilayer Ca_2N, as is anticipated for 2DEG-FS behavior.

The degree to which the surface states extend from the surface of the atomic layers can be determined by finding the average distance of the ILDOS from the outer atomic position:

$$\langle z\rangle = \frac{\int_{-\infty}^{z_{Ca}} z \cdot ILDOS(z)dz}{\int_{-\infty}^{z_{Ca}} ILDOS(z)dz} - z_{Ca}. \tag{3.2}$$

Here, z_{Ca} is the z position of the outermost Ca atom on the left of the material. For monolayer, the average z position relative to the surface is 1.51 Å, and for bilayer, the average z position is 1.70 Å. The higher value of $\langle z\rangle$ for bilayer is likely due to the electrostatic repulsion of the interlayer electrons acting on the surface state electrons.

To quantify the number of 2DEG-FS states in these regions, the ILDOS was integrated along the z-axis over the regions of interest.

$$\langle\sigma\rangle = \int_{-\infty}^{z_{Ca_1}} ILDOS(z)dz + \int_{z_{Ca_2}}^{\infty} ILDOS(z)dz \tag{3.3}$$

For the surface state density of monolayer Ca_2N, we find a value of 0.032 states/Å^2.

This constitutes 83% of the total states around the Fermi level being outside the atomic structure of Ca_2N.

Bialyer Ca_2N has the additional interlayer region that can be integrated, so it has 0.021 states/Å^2 on its outer surfaces, representing 36% of the total states, and 0.027 states/Å^2 in its interlayer region, which is 46% of the total states, leaving only 18% inside the atomic structure of bilayer. This reduction in surface state density from monolayer to bilayer indicates an affinity towards interlayer states rather than interlayer being just a combination of two surface regions.

Like the ILDOS, Quantum Espresso can take the planar average of the electric potential along the z-axis, which is shown in Fig. 3.12. It is then simple to determine the work function of the material by taking the difference between the vacuum energy (flat potential energy in the vacuum region) and the Fermi level. The calculated work function of Ca_2N monolayer and bilayer are 3.60 eV and 3.37 eV respectively, values that are consistent with the results of previous DFT calculations for the out-of-plane work function [24].

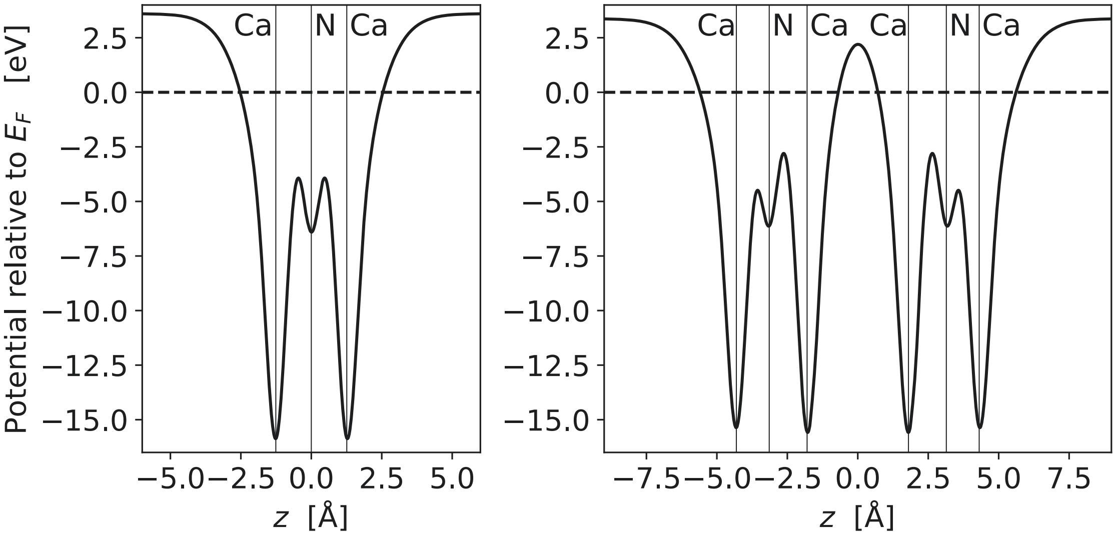

Figure 3.12: Planar averaged electrostatic potential relative to the Fermi level versus out-of-plane direction for monolayer (left) and bilayer (right) Ca_2N.

3.2.1 Comparison to Another 2D Metal

In the interests of establishing the unique properties of electrenes, here we take a moment to perform a comparative analysis to another 2D metal, 1T-MoS_2, which is a transition-metal dichalcogenide (TMDC).

Like Ca_2N, TMDCs have layered crystal structures. They are of the form MX_2 where M is a transition metal and X is from the chalcogen family of elements. They are covalently bonded rather than ionically bonded like Ca_2N, and are easily exfoliated to single layers due to the weak van der Waals interlayer bonding [80]. Under standard conditions MoS_2 is a semiconductor [81, 82], but the material can undergo phase transitions which alters its electrical properties. The thermodynamically stable form of MoS_2 has a trigonal prismatic structure where the two layers of sulfur atoms are aligned in the cross-plane direction, referred to as the 2H phase. The 1T phase is a higher energy polymorph with an octahedral structure where the sulfur atoms become off-set in the cross-plane direction. In this phase, MoS_2 becomes a conductor, and also matches the octahedral structure of Ca_2N [83, 84, 80]. Both of these factors make 2D 1T-phase MoS_2 ideal to highlight the unique attributes of Ca_2N as an electrene material.

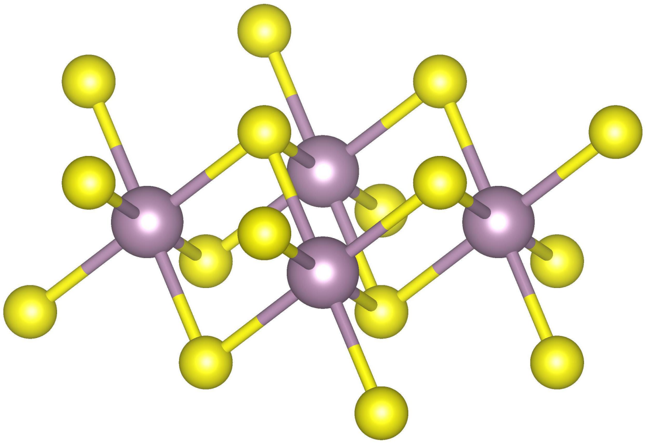

Figure 3.13: The atomic structure of 1T-MoS_2.

Performing a DFT calculation of 1T-MoS_2 yields the expected conductive behavior and crystal structure, with a hexagonal lattice constant of a=3.139 Å which compares well to the 3.168 Å reported in another DFT study [85]. Literature is also in agreement with the calculated band structure [86] and DOS projected orbitals [87], both shown in

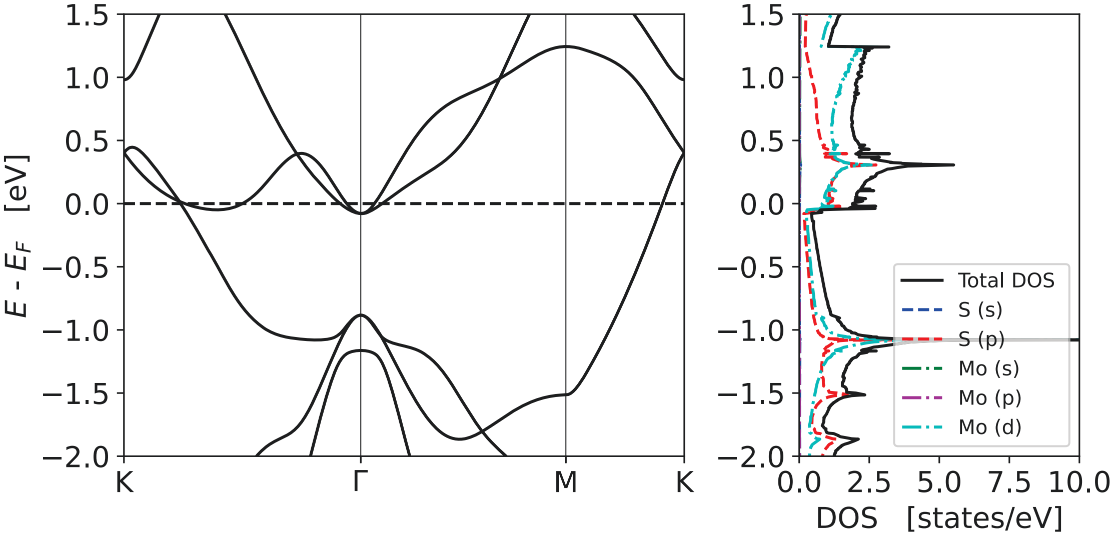

Figure 3.14: Electronic structure of monolayer 1T-phase MoS_2. The band structure (left) and the projected DOS (right) are presented.

Fig. 3.14. The band structure shows the Fermi level crossing several bands, confirming the metallic behavior of 1T-MoS_2. The PDOS shows that states in the vicinity of the Fermi level are composed of d-orbital Mo and p-orbital S states, whereas Ca_2N is mostly s-orbital Ca states in the same region.

The planar average of the ILDOS for monolayer 1T-MoS_2 is shown in Fig. 3.16. With 1T-MoS_2, the electron states are centered around the atomic positions, unlike Ca_2N, with the average surface state density located 0.53 Å beyond the sulfur atom.

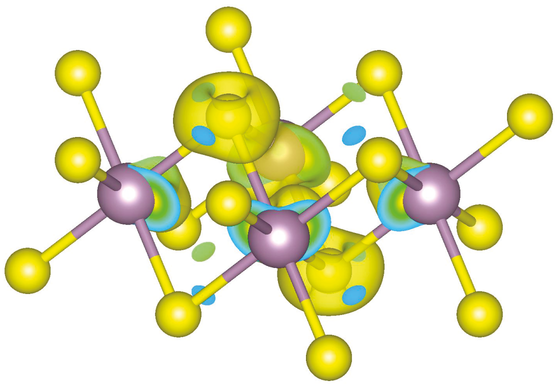

Figure 3.15: ILDOS of monolayer 1T-MoS_2, integrated ±0.1eV around the Fermi level.

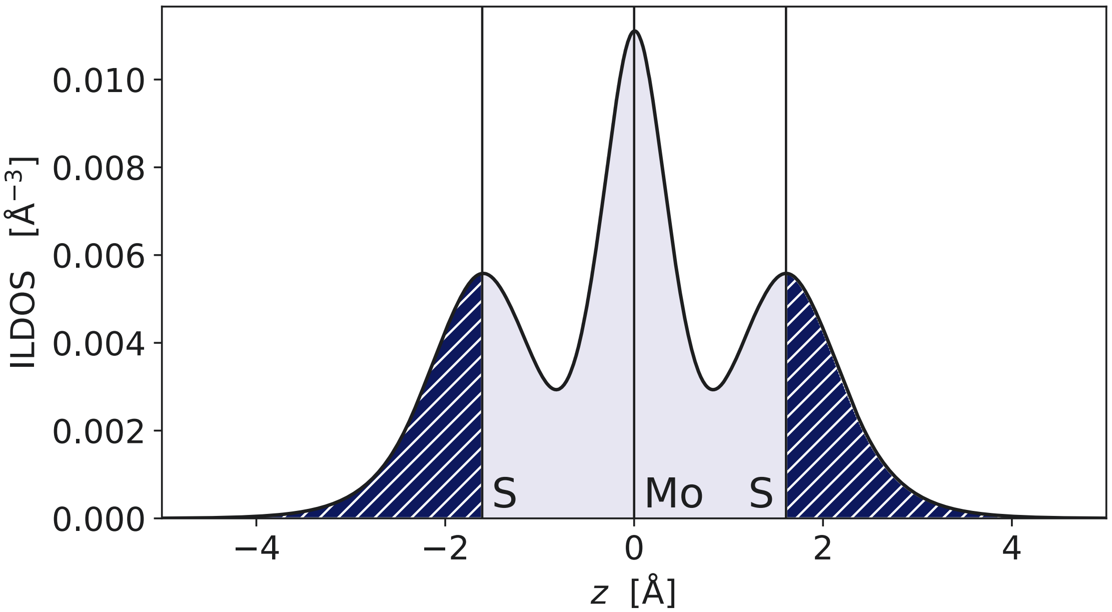

Figure 3.16: Planar average ILDOS of monolayer 1T-MoS_2, integrated ±0.1 eV around the Fermi level.

This is nearly one Angstrom closer to the surface atom compared to that of monolayer Ca_2N (1.51 Å). The surface state density of 1T-MoS_2 constitutes 32% of the total integrated ILDOS, greatly decreased compared to the 83% of monolayer Ca_2N. The 3D spatial distribution of the ILDOS is presented in Fig. 3.15.

For a direct graphical comparison, Fig. 3.17 shows the ILDOS of both monolayer MoS_2 and monolayer Ca_2N normalized by total integrated ILDOS. From this it is clear how the ILDOS of Ca_2N extends farther out from the lattice compared to 1T-MoS_2. This extension of states is unique to the electride family of materials, and distinguishes them from other conductive materials.

Lastly, the work function of monolayer 1T-MoS_2 was determined to be 5.052 eV, a 40% increase from that of monolayer Ca_2N. Because the surface electrons in Ca_2N are located far from the atoms, they possess a lower work function, whereas they are more tightly bound in 1T-MoS_2.

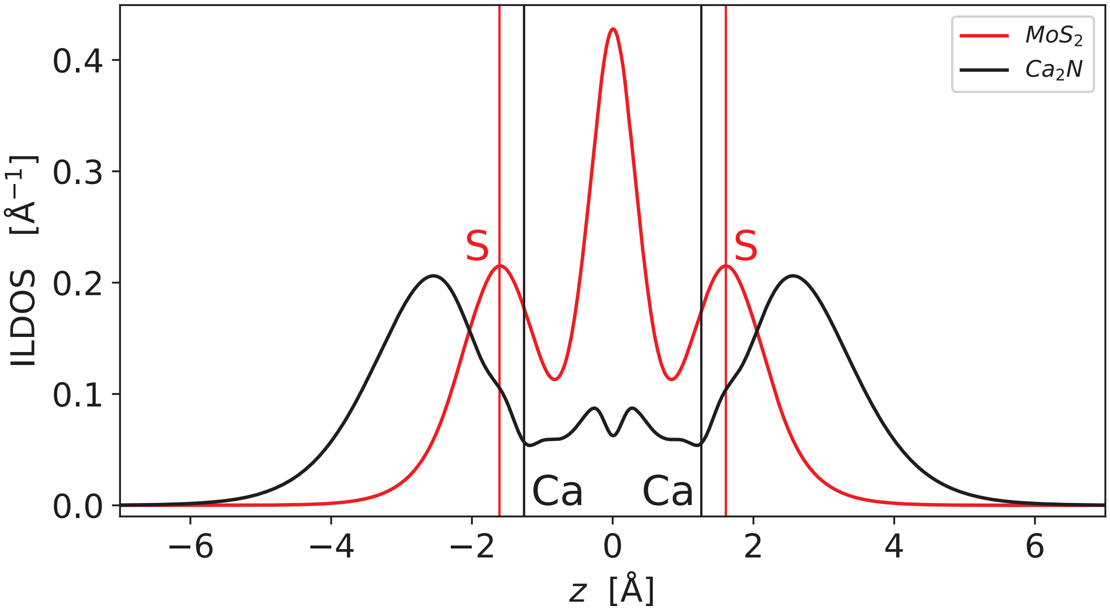

Figure 3.17: Planar average ILDOS normalized by total integrated ILDOS for monolayer Ca_2N and monolayer 1T-MoS_2, integrated ±0.1 eV around the Fermi level. The z position of the surface atoms of both materials, Ca and S, are indicated by vertical lines.

3.3 Strained Ca_2N Electrene

Next, we begin investigating how the properties of Ca_2N change when placed under strain, both tensile and compressive. To illustrate these changes, the most extreme and the least extreme results will be explored with ±5% and ±1% strain applied in both of the in-plane directions simultaneously.

Figure 3.18 presents how the band structure and DOS vary with strain. It is apparent that the effects of ±1% strain on the band structure are minimal, with notable changes in band energy or DOS only occurring in ±5% cases. This would indicate that the electric properties of Ca_2N have a slow response to strain, particularly near the Fermi level. The DOS reveals that the general trend of this response is that tensile strain moves states to a lower energy while compressive strain shifts states to a higher energy. This could be due to compressive strain forcing atoms closer together, causing an increase in electrostatic repulsion.

The exception to this trend is the highest energy surface band near the zone center, which instead increases energy with positive strain and decreases energy with

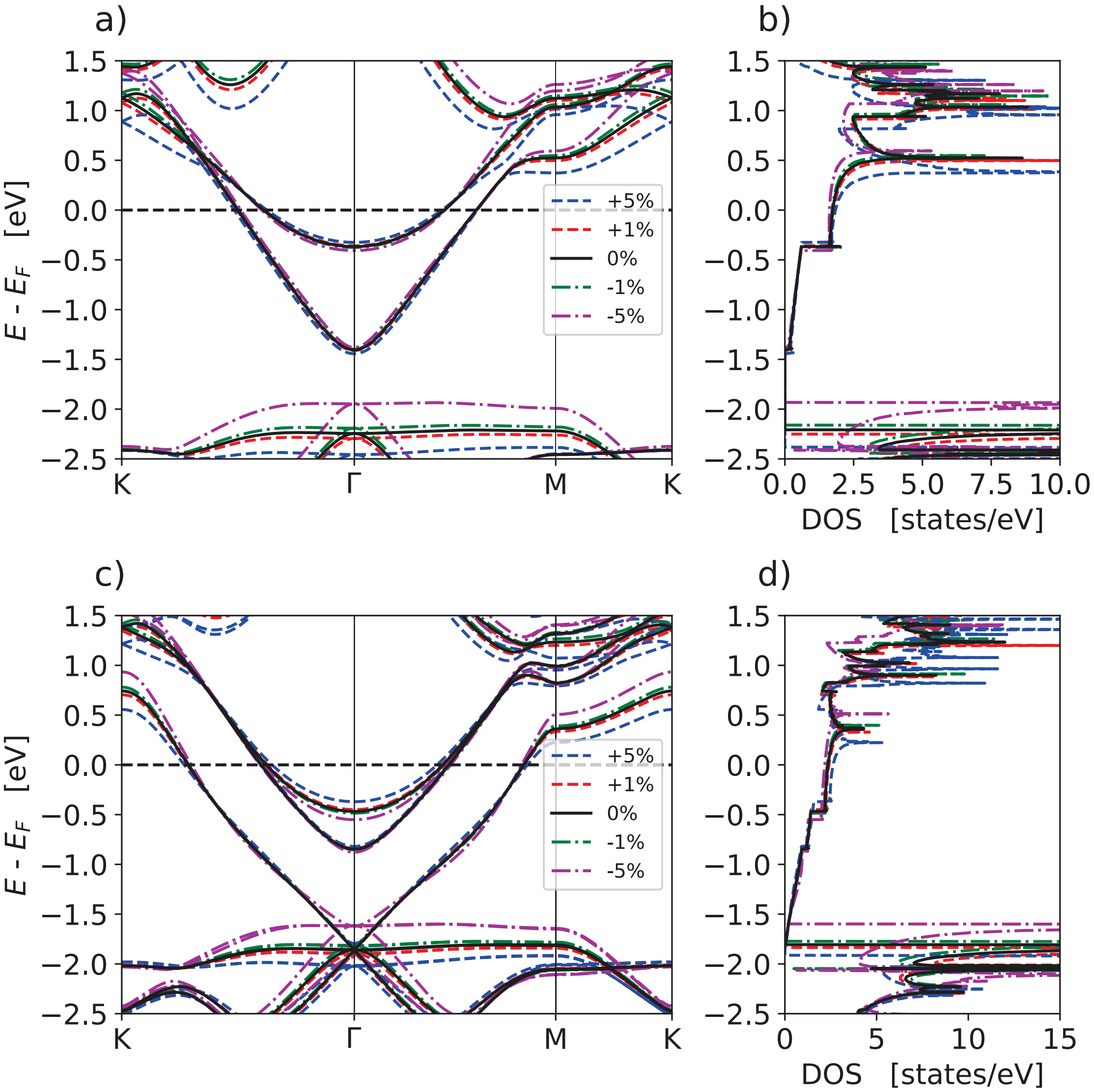

Figure 3.18: Band structure (left) and DOS (right) of Ca_2N in monolayer (a,b) and bilayer (c,d) forms with applied in-plane strain.

negative strain. A similar feature is observed in the interstitial band of bilayer between Γ and M. This possibly occurs due to the fact the number of occupied states must be unchanged between strain cases, as strain neither adds nor removes electrons from the material. Therefore any increase in occupied states in one band must be offset by a loss of occupied states in another. To observe how the **k**-resolved electron density evolves with strain, see Appendix C for the changes at the Γ point and the M point.

There is a particular resistance to band movement under strain seen in the surface and interstitial bands, with an almost pinning effect near to the Fermi level. Given that it is band behavior near the Fermi level which dictates electron mobility, it is important to have a clear understanding of how the concentration of states changes in this region. Figure 3.19 shows how the planar ILDOS around the Fermi energy changes with strain. Monolayer displays a direct relationship between compressive strain and the ILDOS, with up to a ∼12% increase at the maximum peak. This is corroborated in Fig. 3.20 which shows the surface state density increasing by up to

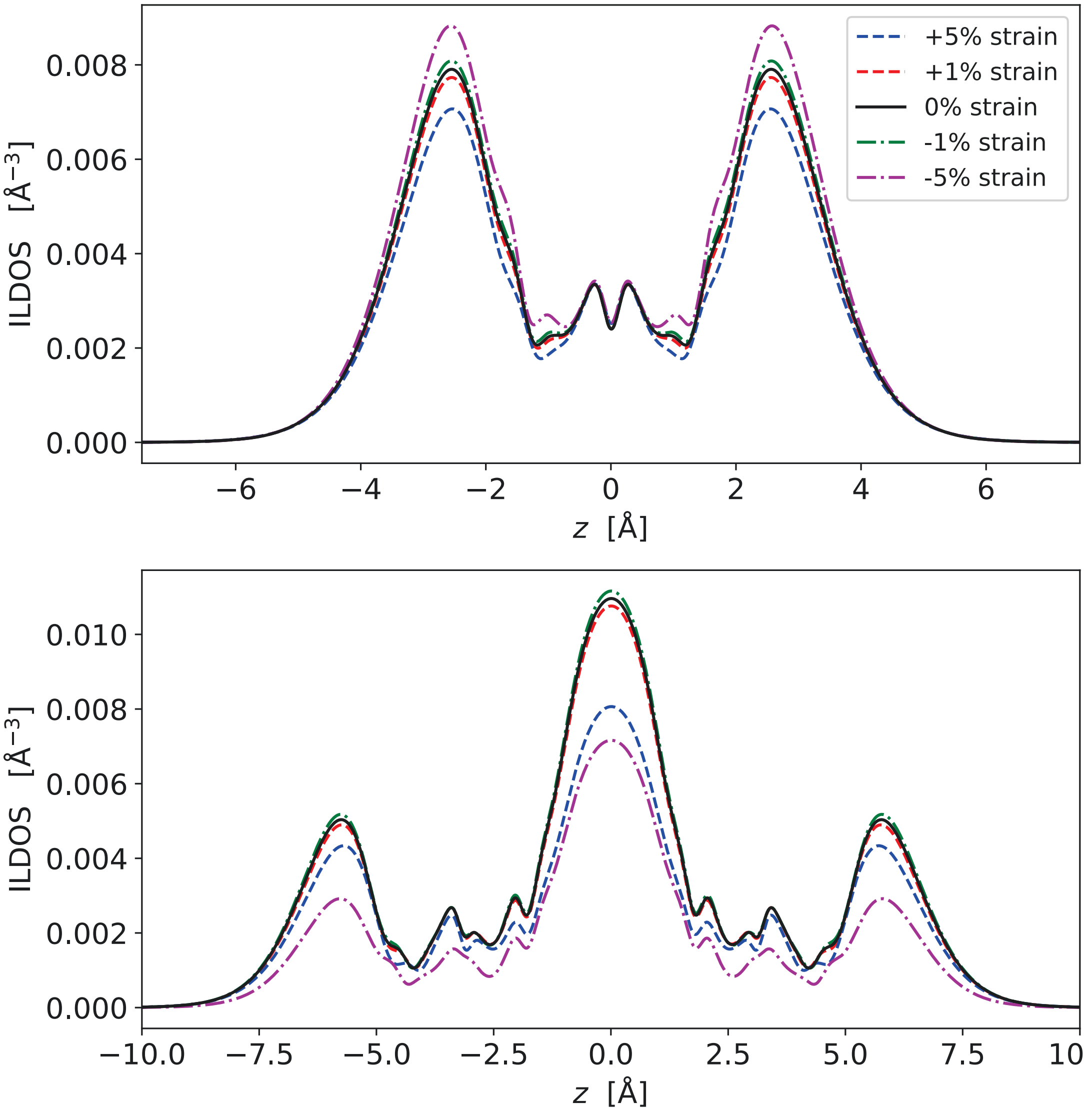

Figure 3.19: Effects of strain on the planar averaged ILDOS of monolayer (top) and bilayer (bottom) Ca_2N over the energy range $E_F \pm 0.1$eV.

10% with a -5% compressive strain.

This trend in the ILDOS is the opposite of the DOS shown in Fig. 3.18b. The DOS shows a minute increase under +5% strain and a minute decrease under -5% strain in the energy range of the ILDOS. The discrepancy can be explained by the change in lattice constants of the unit cell under strain. Tensile strain increases in the area over which states are distributed, causing a drop in the surface state density and ILODS, which are spatially dependent. A compression of the lattice vectors produces the opposite effect in compressive strain cases. Therefore, the strain trend seen in the ILDOS and density of surface states for monolayer Ca_2N can be attributed entirely to the change in the area of the unit cell with strain.

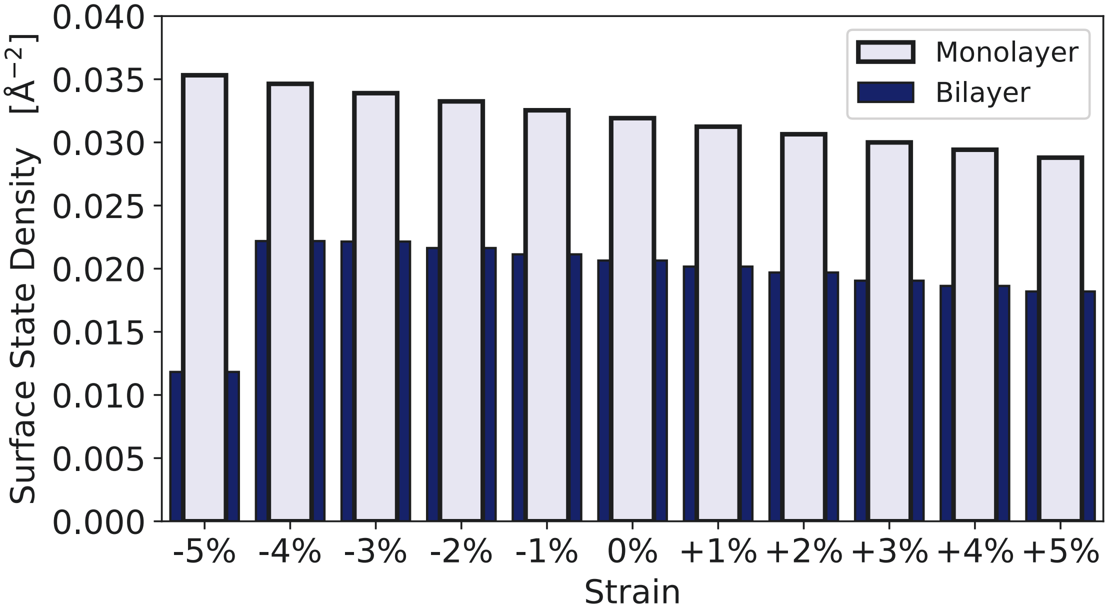

Figure 3.20: Surface state density versus strain for monolayer and bilayer Ca_2N.

Simply by changing the shape of the lattice, electron mobility shows potential improvement under compressive strain given the increase of state density around the Fermi level. Figure 3.20 confirms that the surface state density of bilayer also rose by 7% at -4% strain, but falls off significantly for -5%. The interlayer state density, shown in Fig. 3.21, is not monotonic either, and drops at compressive strain below -3%. This could potentially offset the improvements in surface state density at -4% strain given the greater proportion of states in the interlayer region.

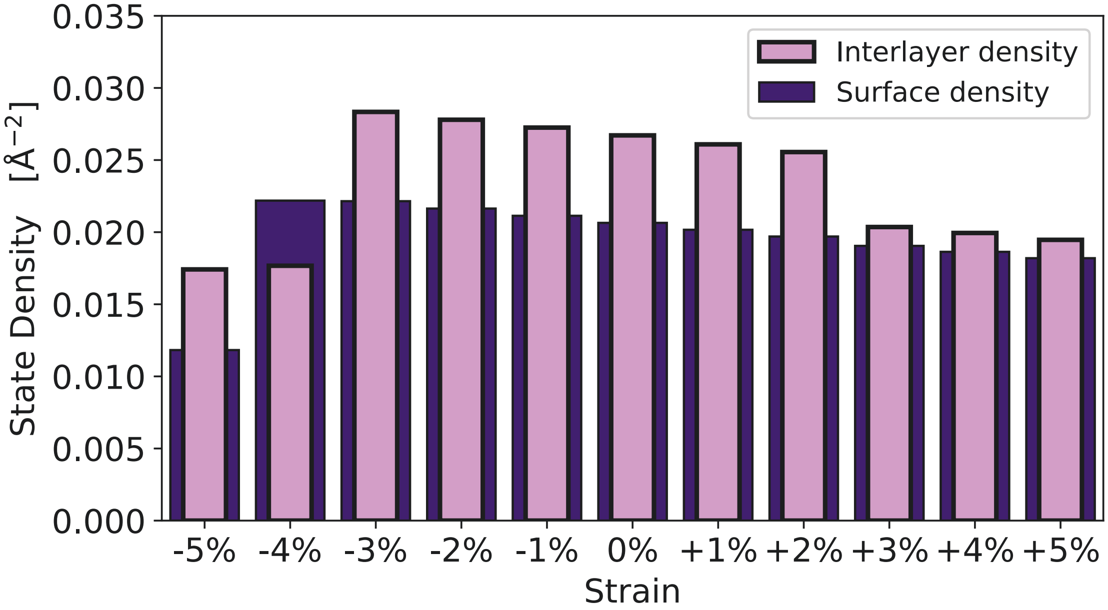

Figure 3.21: Interlayer and surface state density versus strain for bilayer Ca_2N.

Figure 3.22 shows the average z position of the surface state density around the Fermi level for monolayer and bilayer. The average z correlates directly with the applied strain, but only changes by about 0.1 Å between minimum and maximum strain for monolayer, and 0.17 Å for bilayer. This is again likely due to the compression of the atomic layer with positive strain, causing lattice states to be pushed out onto the surface.

The work function of strained Ca_2N was extracted from the electrostatic potential energy (shown in Appendix B). Figure 3.23 shows a monotonic decrease of the work function with increasing strain values, varying the most for bilayer. The change in work function is 0.3 eV for monolayer and 0.4 eV for bilayer across ±5% strain, and brings the work function for bilayer Ca_2N below 3.2 eV. This is due to the thickness of the atomic layers decreasing with applied tensile strain (the table of Poisson's ratios is included in Appendix A). As the layers get thinner, the electrons are squeezed together, increasing the mutual repulsive force between them and reducing the energy needed to extract one electron to the vacuum level.

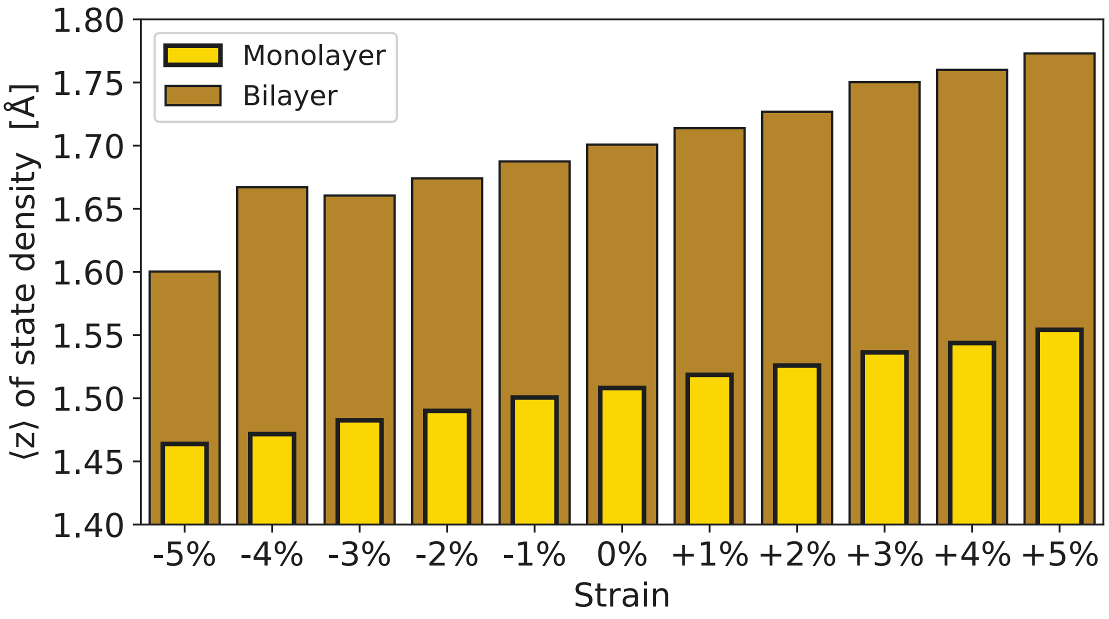

Figure 3.22: Average z position of surface state density relative to outer atomic layer versus strain.

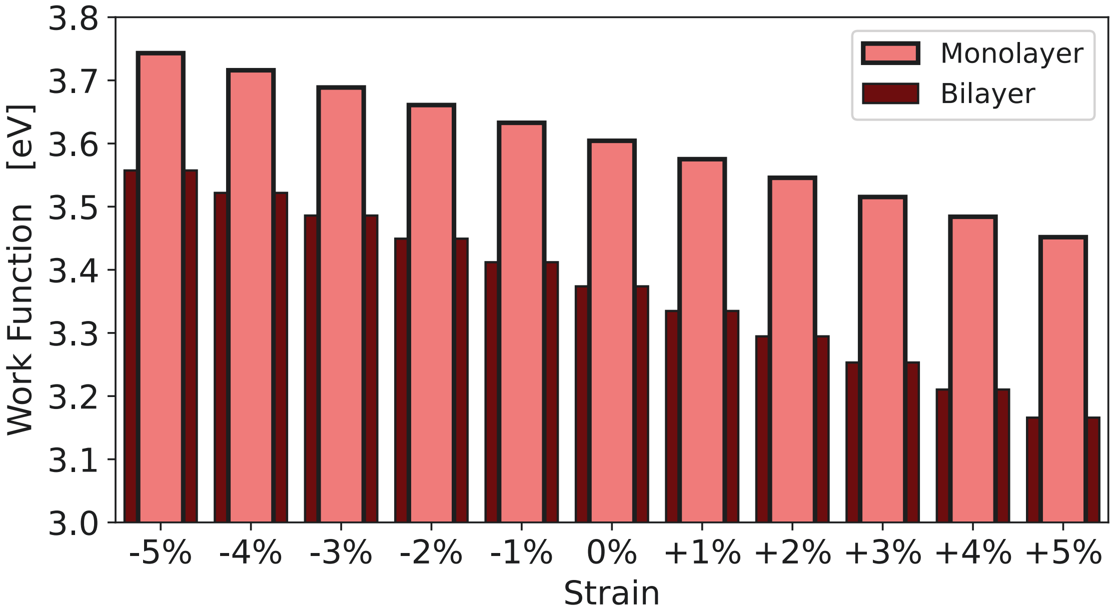

Figure 3.23: Work function of monolayer and bilayer Ca_2N versus strain.

3.4 M_2X Electrenes

Having examined the DFT results for monolayer and bilayer Ca_2N, and corroborating those results with the literature for electrenes, we now extend our analysis to include all seven electrenes of the form M_2X (Ca_2N, Sr_2N, Sr_2P, Ba_2N, Ba_2P, Ba_2As, Ba_2Sb).

Material	**a**	**c**	Layer thickness
Ca_2N	3.584	29.998	2.518
Sr_2N	3.829	32.000	2.755
Sr_2P	4.407	32.000	3.160
Ba_2N	3.959	32.000	3.022
Ba_2P	4.576	32.000	3.427
Ba_2As	4.689	32.000	3.510
Ba_2Sb	4.947	32.000	3.709

Table 3.5: Lattice parameters of monolayer electrenes. **a** and **c** are the in-plane and out-of-plane lattice constants and are measured in Angstroms, as is the single layer thickness.

Material	**a**	**c**	Layer thickness	Interlayer gap
Ca_2N	3.579	34.582	2.510	3.597
Sr_2N	3.823	34.000	2.749	3.961
Sr_2P	4.416	34.000	3.146	3.849
Ba_2N	3.979	34.000	3.013	4.388
Ba_2P	4.592	34.000	3.437	4.316
Ba_2As	4.703	32.000	3.518	4.259
Ba_2Sb	4.964	34.000	3.718	4.146

Table 3.6: Lattice parameters of bilayer electrenes. **a** and **c** are the in-plane and out-of-plane lattice constants and are measured in Angstroms, as are the single layer thickness and interlayer gap.

3.4.1 Band Structure and Density of States

The band structures of all seven monolayer electrenes are shown in Fig. 3.24. In all cases, there are two surface bands that cross the Fermi level, which are responsible for the surface states on either side of the materials. The energy range of the bands decreases as the elements move down the periodic table. This leads to flatter bands with the heavier elements, which results in a larger DOS, as seen in Fig. 3.25. With

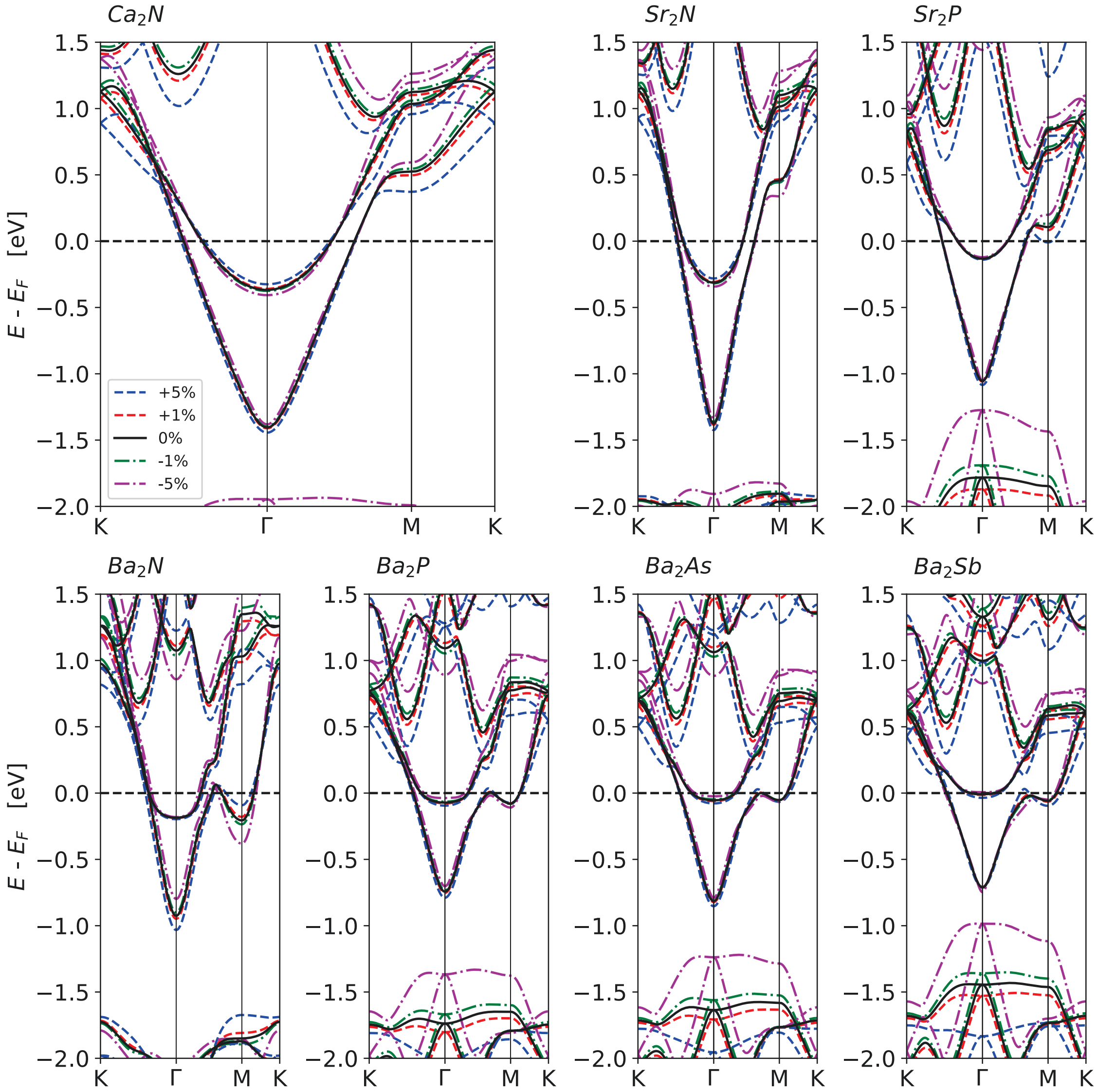

Figure 3.24: Band structures of all monolayer electrenes with applied strain.

the application of strain, in all cases, the states near the Fermi level show little movement. Most of the band movement is observed at the M point.

An interesting feature of the Ba series of electrenes is how the lower surface band has a local maximum along the Γ-M path. With Ba_2N, this local maximum occurs just above the Fermi level. Importantly, this feature can be made to cross the Fermi level with the application of tensile strain in the case of Ba_2P, Ba_2As, and Ba_2Sb. The lower surface band of Sr_2P can also be made to cross the Fermi level with a local minimum at the M point. This demonstrates how an applied strain can move states up or down in energy depending on its location in the Brillouin zone.

This is corroborated by the peaks in the DOS shown in Fig. 3.25. Peaks highlight the location of flat regions (often near the Brillouin zone edge) in the band structure, with abrupt step-like increases in the DOS corresponding to the band edges. Tracking the movement of these features as strain is applied allows us to see how states move up and down the energy scale as strain is modulated. Focusing on energies near to the Fermi level, which are relevant for conduction (roughly 10 k_BT around E_F), we identify that Sr_2P and Ba_2X display the largest changes in DOS with strain. This

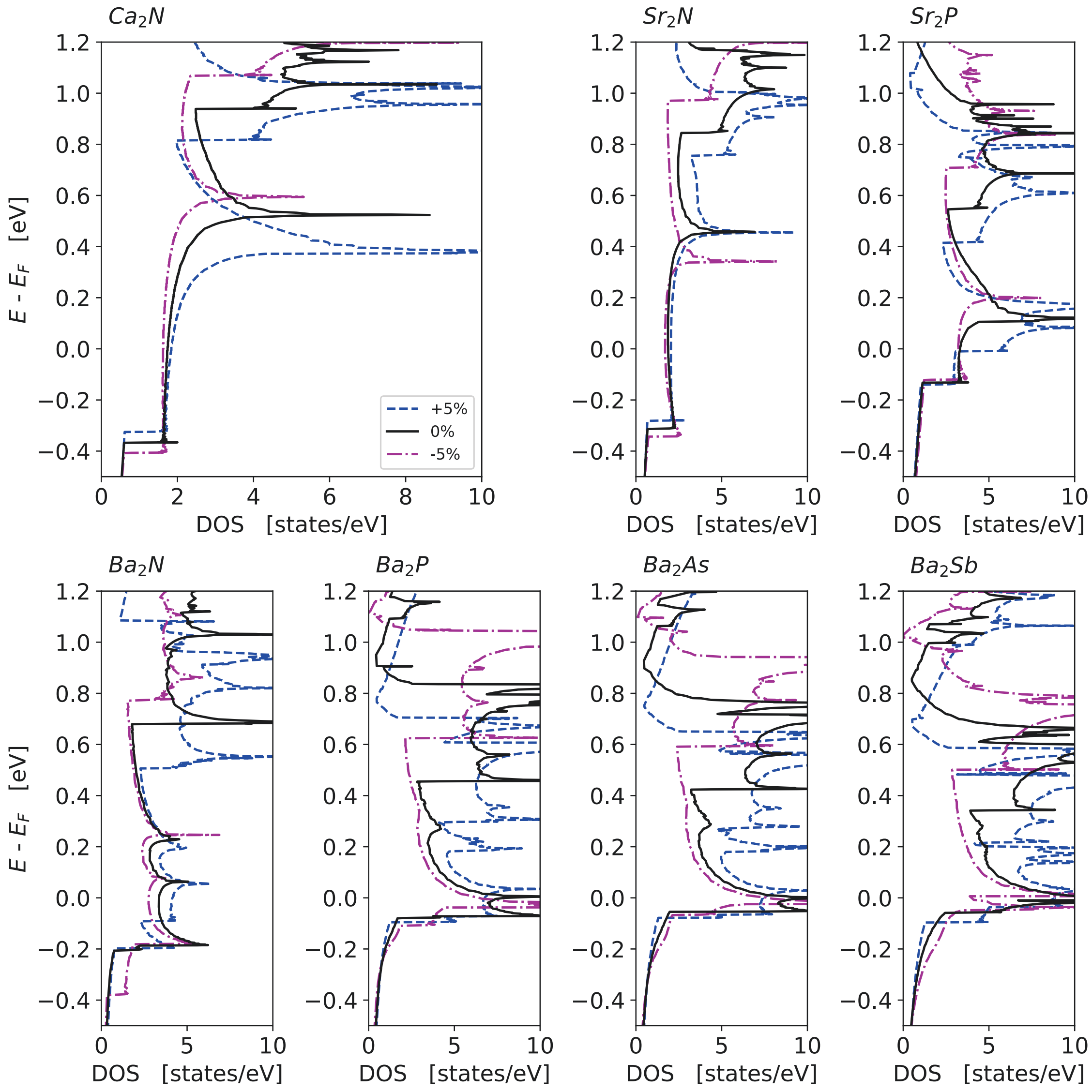

Figure 3.25: Density of states of all monolayer electrenes with applied strain.

suggests that these materials could show increased electron transport performance under strain.

However, the charge available for transport may be harmed by the fact that the Ba_2X series sees the top surface band advancing toward the Fermi level, with the band in Ba_2Sb having almost no filled states at all. This is reflected in the DOS where the first peak moves progressively closer to 0 eV from Ba_2N to Ba_2Sb. In addition, as the upper surface band moves toward the Fermi level it flattens, and the electron velocity of those states (proportional to the slope of the band) decreases, which would

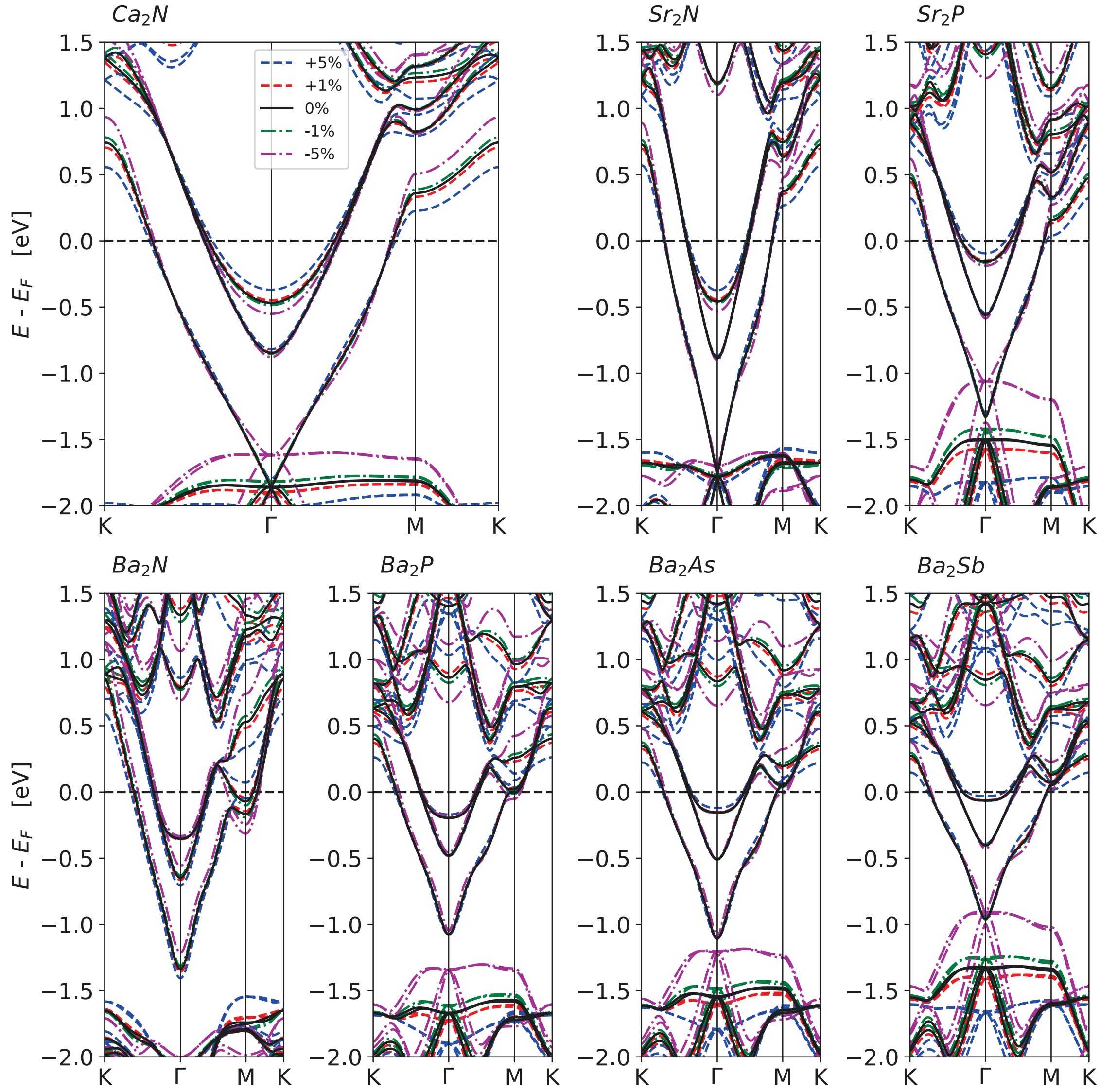

Figure 3.26: Band structures of all bilayer electrenes with applied strain.

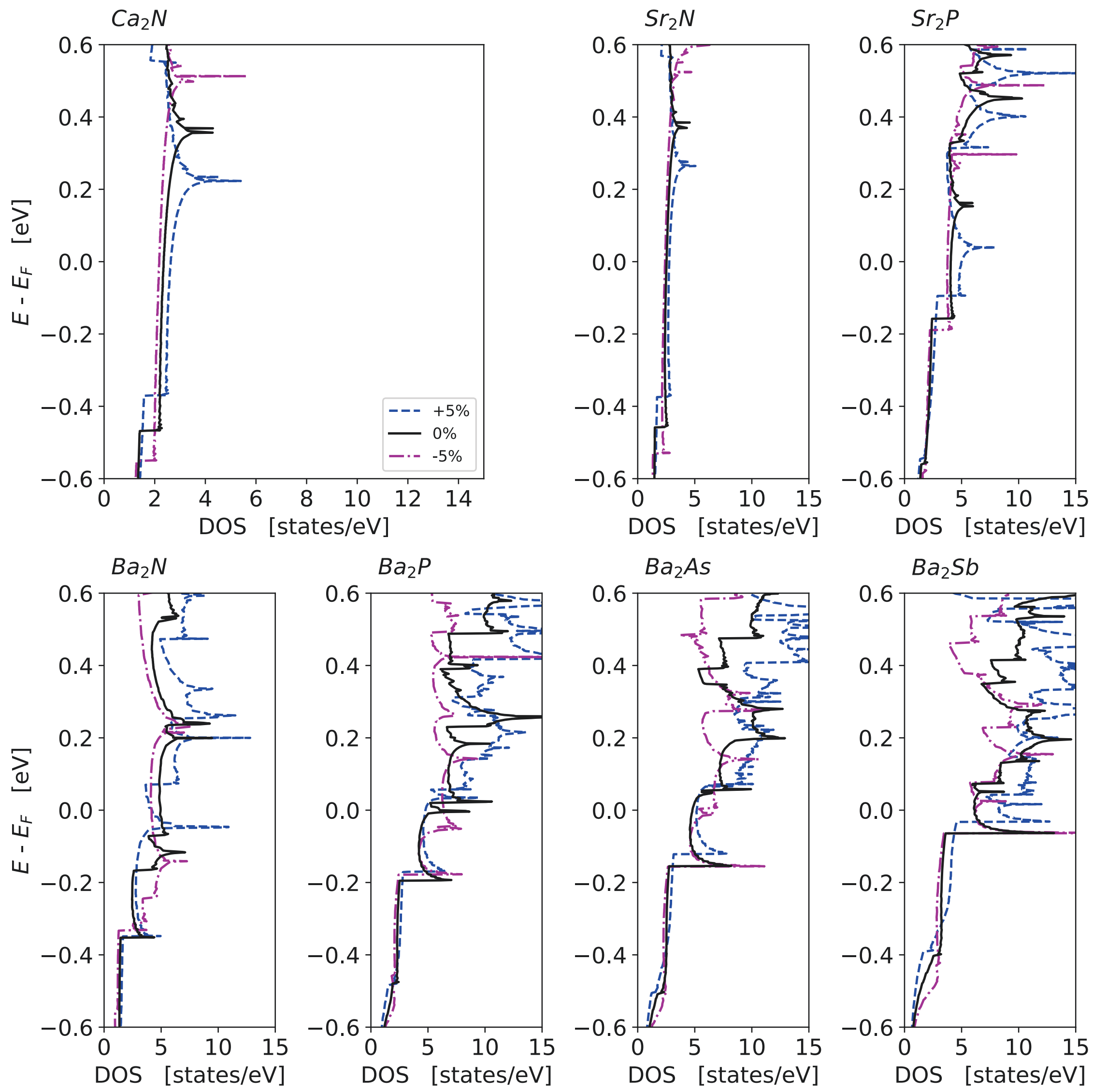

Figure 3.27: Density of states of all bilayer electrenes with applied strain.

negatively impact transport.

From the band structure of the bilayer materials, shown in Fig. 3.26, Ca_2N and Sr_2N display similar properties, with a weak strain dependence near the Fermi level. Under tensile strain the upper surface band increases in energy while the interlayer band decreases in energy, which is also clearly observable in the DOS shown in Fig. 3.27. The flat interlayer band at the M point makes a distinctive peak in the DOS.

The surface and interlayer bands of Sr_2P and the Ba_2X electrenes cross the Fermi level at the M point due to the applied strain. Multiple bands intercept near the M point, with different dependencies on strain, leading to complex band behavior. From Fig. 3.27, we find an increase in DOS at the Fermi level for tensile strain in Sr_2P, Ba_2As, and Ba_2Sb and for compressive strain in Ba_2As. This suggests that improved electronic conduction due to strain could be possible in those electrenes. However, further insights can be gained from the ILDOS, as presented below.

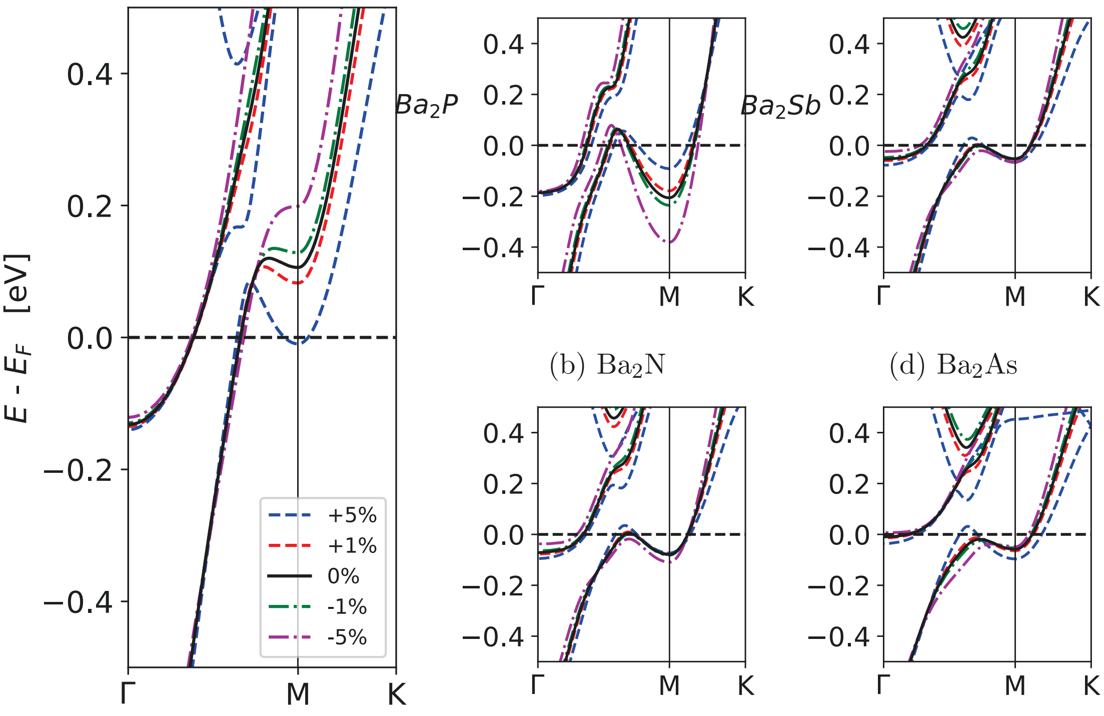

(a) Sr_2P

(b) Ba_2N

(c) Ba_2P

(d) Ba_2As

(e) Ba_2Sb

Figure 3.28: Band structures of monolayer electrenes with bands that cross the Fermi level due to strain.

The region of the band structure that showed the largest response near the Fermi level is in the vicinity of the M point. To better highlight band movement under strain, Fig. 3.28 and Fig. 3.29 show the band structure for monolayer and bilayer electrenes (which have bands crossing at the Fermi level as a result of strain) around the M point.

For monolayers, Sr_2P has an unoccupied portion of one of its surface bands drop to the Fermi level at 5% tensile strain. Ba_2P, Ba_2As, and Ba_2Sb have occupied portions of a surface band rise above the Fermi level along the Γ-M path at 5% tensile strain.

In the case of bilayers, the bands closest to the Fermi level near the M point are

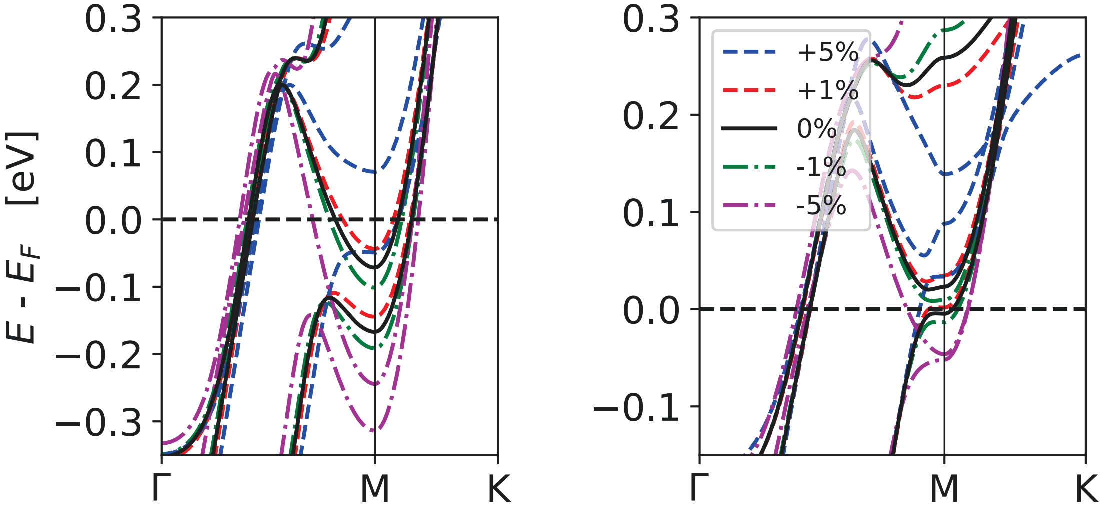

(a) Ba_2N (b) Ba_2P

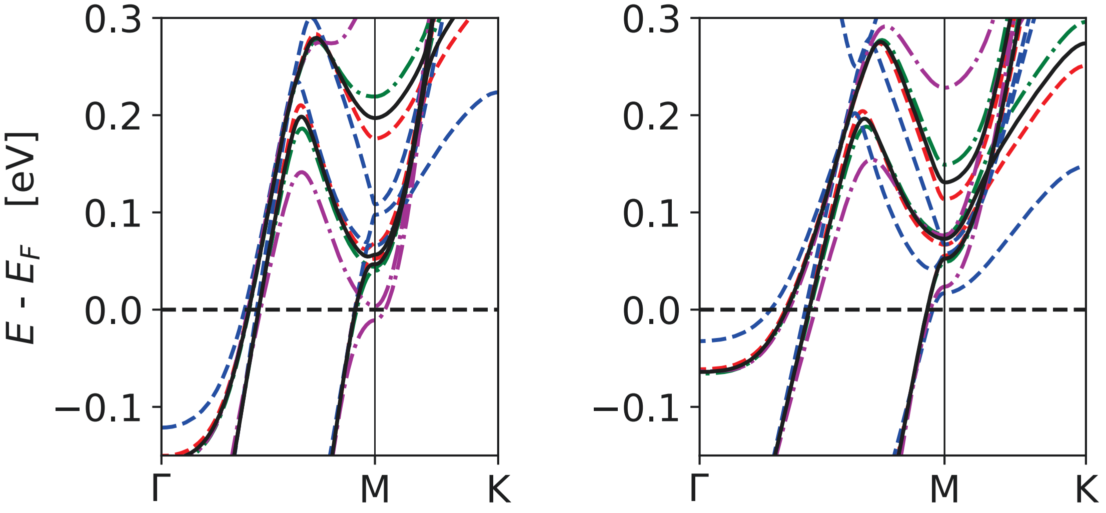

(c) Ba_2As (d) Ba_2Sb

Figure 3.29: Band structures of bilayer electrenes with bands that cross the Fermi level due to strain.

pushed up by tensile strain and pushed down by compressive strain. One exception is Ba_2Sb, which shows opposite band movement with strain.

3.4.2 Integrated Local Density of States

Figure 3.30 shows the planar averaged ILDOS integrated over the energy range E_F±0.1 eV for all monolayer electrenes to compare their conduction states, and how

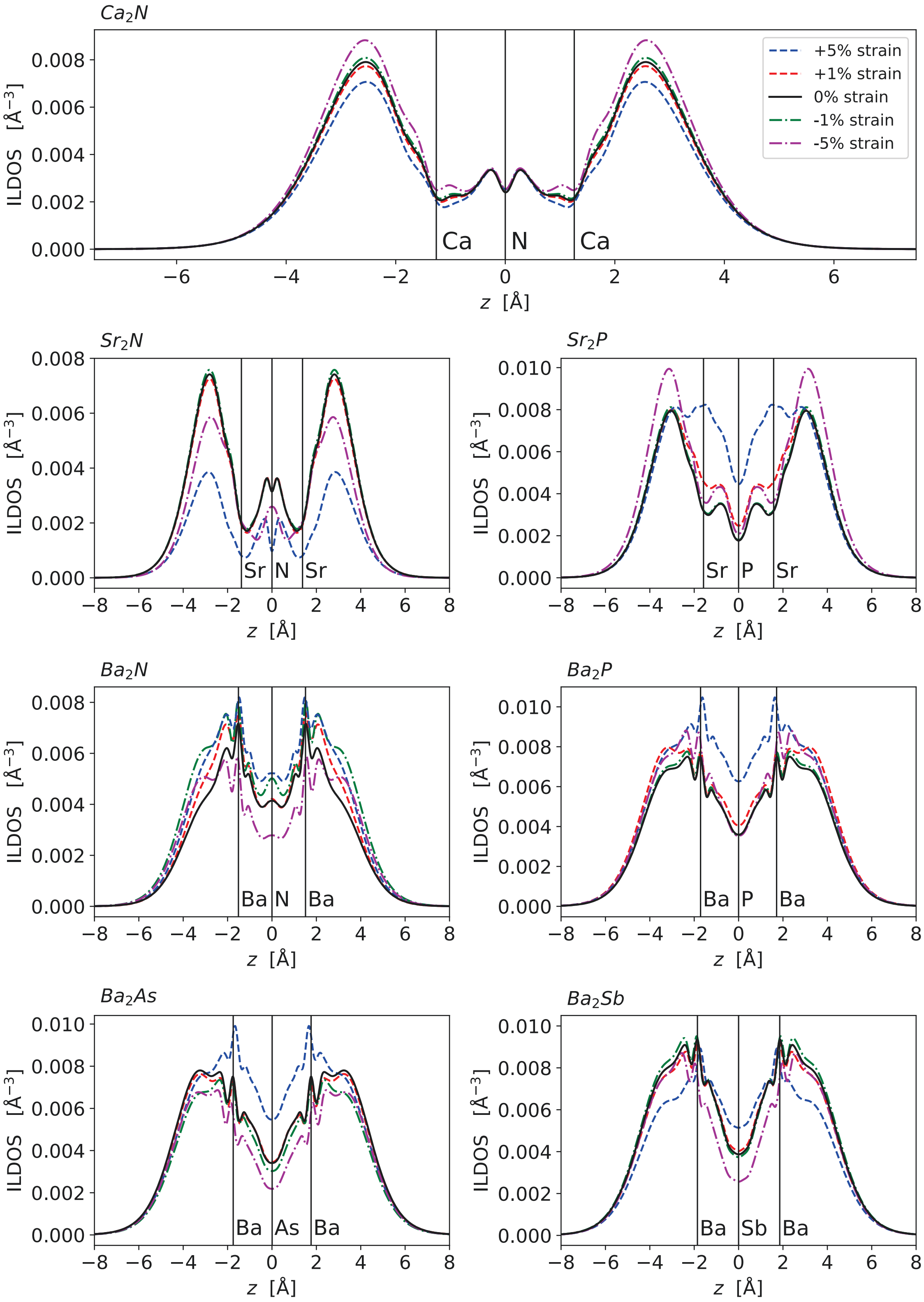

Figure 3.30: Planar averaged ILDOS for all monolayer electrenes versus out-of-plane direction as a function of strain. Vertical lines show atomic positions for the unstrained lattice.

those states along the z-axis change with strain.

The shape of the ILDOS distribution shown in Fig. 3.30 changes a great deal going from Ca_2N and Sr_2X to Ba_2X. The clear peaks of the surface state regions are less distinct as the peaks become much broader and overlap significantly with ILDOS located near the center, in most cases producing a minimum at z=0. In a previous study of these electrenes [1], ILDOS in the central region was flatter, and the peaks more separated. The difference is that the energy integration range in the ILDOS of the previous study ranged from the bottom of the surface bands up to the Fermi level, while in this study the energy range is focused around the Fermi level. This suggests there is a change in the spatial character of states near the Fermi level versus the states near the bottom of the surface bands.

The electrene's response to strain is quite variable. Ca_2N has a very clear strain response, increasing for compressive strain and decreasing for tensile strain. In Sr_2N, the ILDOS drops off dramatically for both ±5% strain. The monolayer Sr_2P and Ba_2X have ILDOS that increase substantially in the interior of the lattice under tensile strain. On the surfaces, the ILDOS can increase or decrease with either tensile or compressive strain, with no clear trend among these electrenes. Strain response is thus particular to the electrene being examined in this energy range.

To quantify and compare the state density of the monolayers, the ILDOS is integrated over the entire z range and over only the surface regions. The results are displayed in Fig. 3.31.

In the previous study [1], it was shown that the density of surface states decreases with the heavier elements as a result of the larger atomic radii leading to increased lattice constants, causing an otherwise equivalent amount of charge to be distributed over a greater area. Here it is shown that this is not the case for states near the Fermi level. Ca_2N and Sr_2N, the electrenes that should have the smallest lattice constants, have among the lowest total state and surface state densities for all strain cases. This indicates other electrenes have a higher density of surface states outside the atomic lattice which are conducive to low-scattering transport.

Quantifying the surface states in this way also shows that changes in the surface state density due to strain are reflected in the total state density. This indicates that the density of high conduction 2DEG-FS states is benefiting from strain engineering

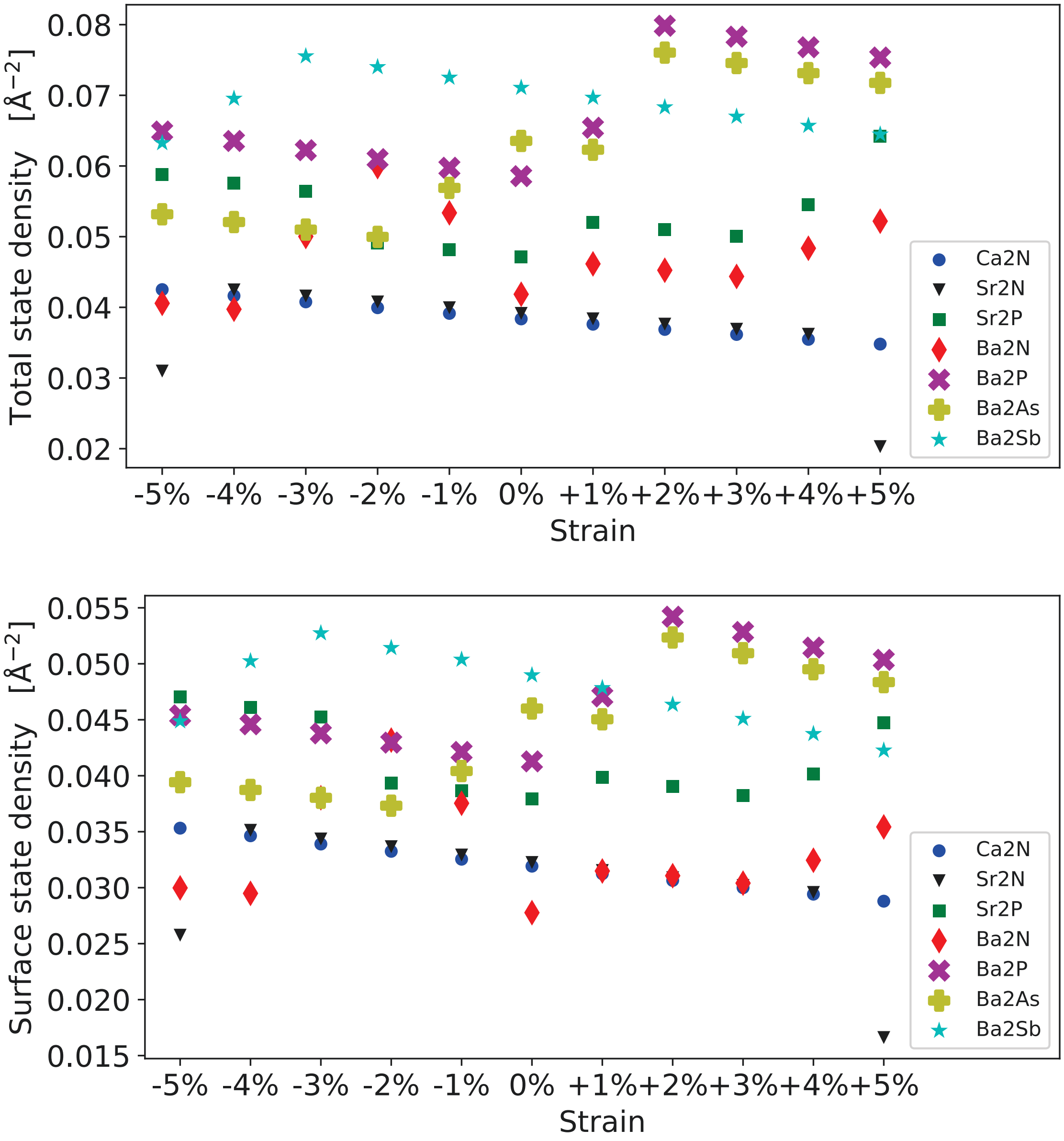

Figure 3.31: State density of all monolayer electrenes for (top) the entire range of z and (bottom) only the surface regions.

in a way that is proportional to the over all state density, despite the energy shift of states being disproportionate across the Brillouin zone under strain. States which show clear 2DEG-FS character (like those near the bottom of the surface bands at the Γ point) are likely to be more beneficial to conduction versus states near the M point that display less 2D character and are not necessarily localized to the surfaces. These results show that the density of such poorly localized states is not disproportionately favored by strain manipulation.

What has yet to be determined is what the electron-phonon coupling strength of these non-2DEG-FS states are. It seems unlikely they have as low a coupling as those states that have 2DEG-FS character, but at this time it is difficult to come to a conclusion on how they affect the conductive properties of the materials in comparison to Ca_2N. For the time being, the states most impactful to transport efficiency will be assumed to be those in the 2DEG regions of the material, so the surface and interlayer state counts will be considered the best indicator of overall conductivity. This is a reasonable assumption as bands which correspond to more localized states are generally very flat, which means lower electron velocities and lower conduction.

All bilayer electrenes, shown in Fig. 3.32, display a central ILDOS peak for the interlayer states and secondary peaks on the sides due to the surface states, with the exception of Ba_2N. The most prominent changes in ILDOS due to strain are focused near the interlayer region, although the strain trend is again very different among different electrenes. This suggests that these bilayers could show similar variation in their conductivity response to strain, with Ba_2N and Ba_2Sb presenting the most increase in the interlayer ILDOS with strain.

Figure 3.33 shows the total, surface and interlayer state density for all bilayers. It shows that a bilayer form improves the interlayer state density for Ca_2N and Sr_2N, having now some of the highest state densities in this region, though the Ba_2X series has the highest state density in surface regions. For the interlayer region, Ca_2N, Ba_2P and Ba_2As show the best performance.

The state density of bilayer electrenes show a great deal of difference in the way interlayer and surface densities are affected by strain. There is a downturn in the interlayer state density of Ca_2N and Sr_2N at -4 and -5% strain, and a drop in surface states for Sr_2N at any value of compressive strain. Ba_2As surface density decreases with tensile strain until +5%, and has nearly strain-invariant interlayer states. The electrenes with the most variable density are Ba_2N and Ba_2Sb in the interlayer region, but all electrenes, monolayer or bilayer, seem to have strain cases which maximize the density of states in the energy range around the Fermi level. This should correspond to a maximization of conduction benefiting states under strain modulation. What isn't known at this time is if there is a benefit to maximizing the surface state density,

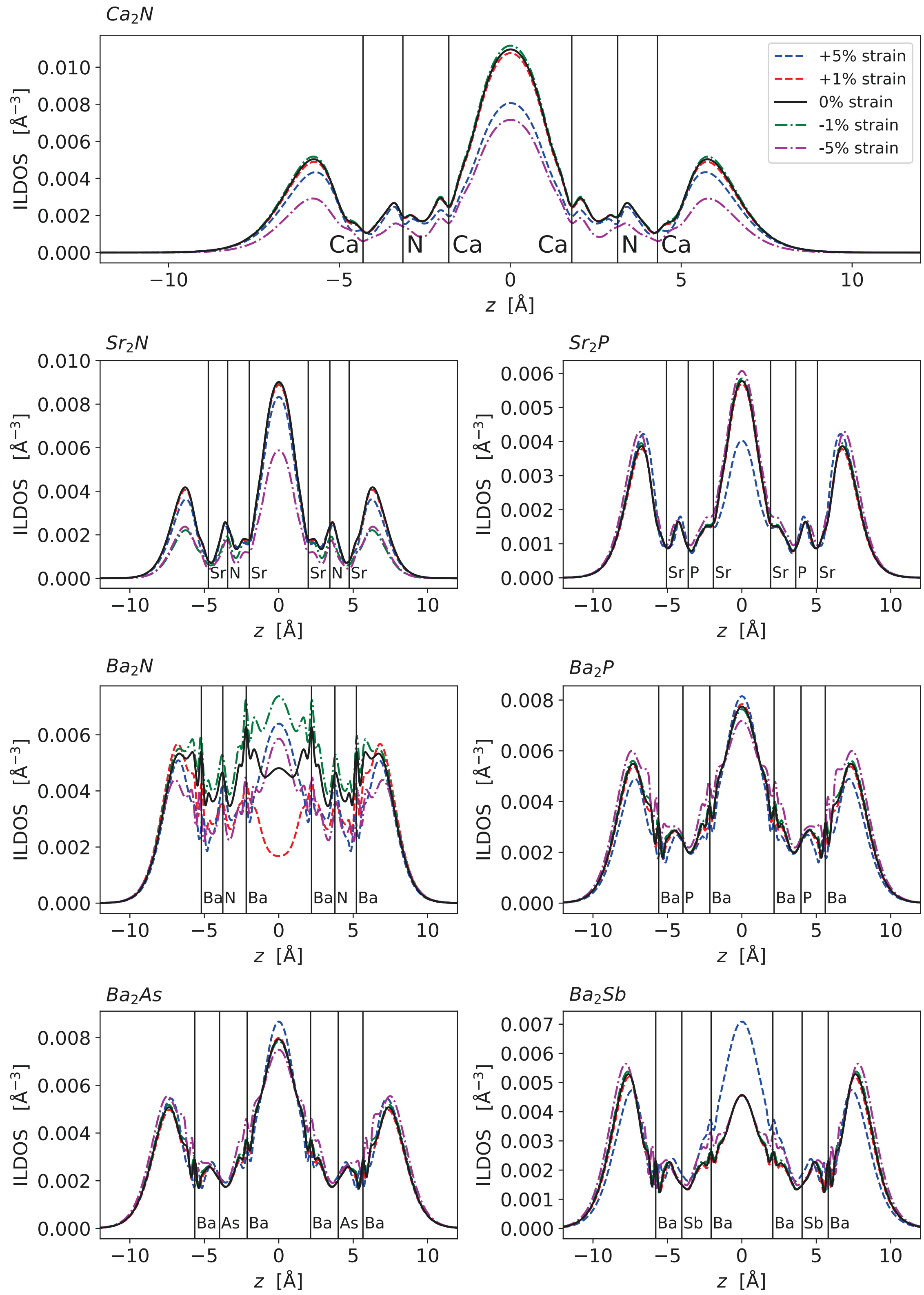

Figure 3.32: Planar averaged ILDOS for all bilayer electrenes versus out-of-plane direction as a function of strain. Vertical lines show atomic positions for unstrained lattice.

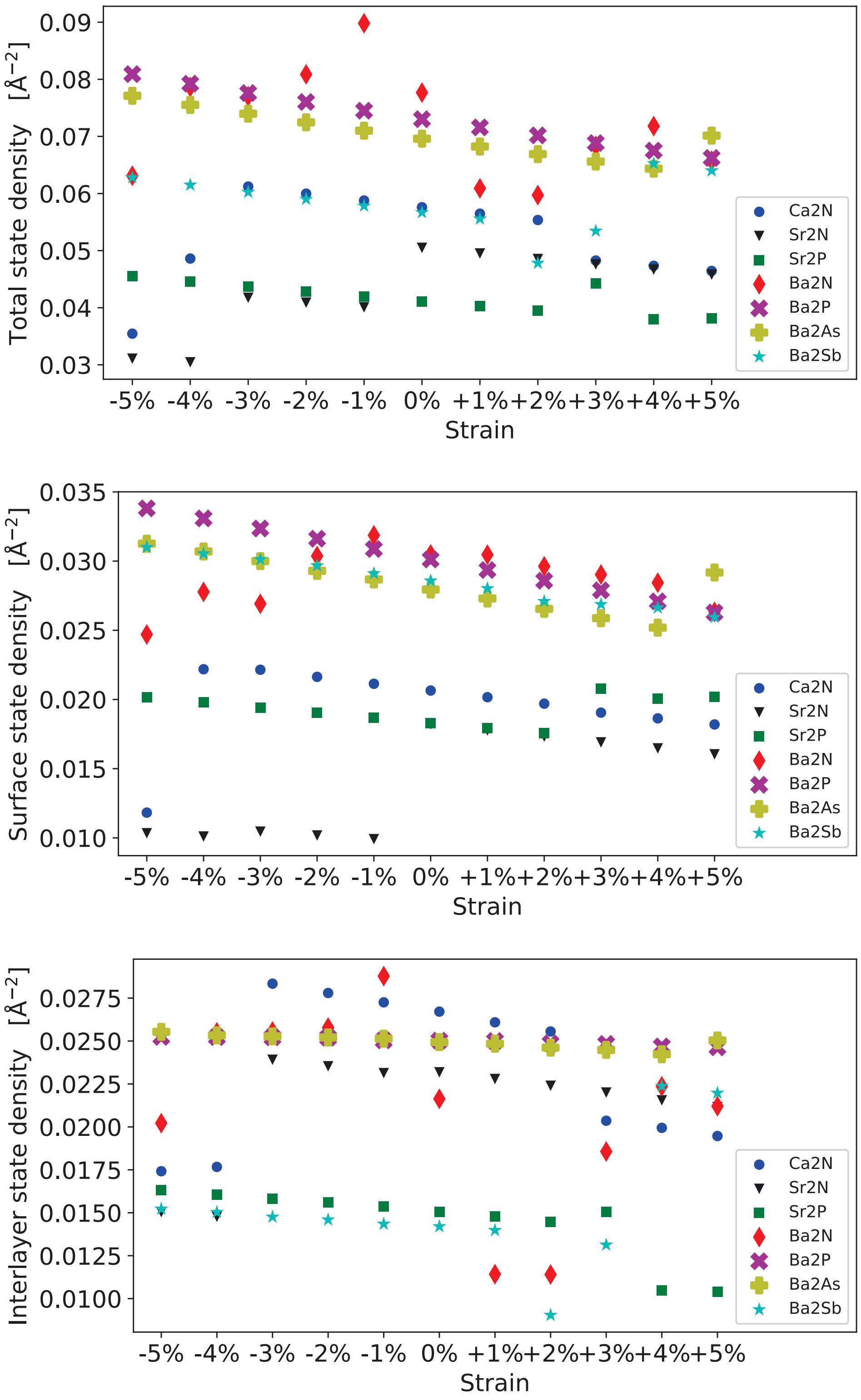

Figure 3.33: State density of all bilayer electrenes for (top) the entire range of z, (middle) the surface states, and (bottom) only the interlayer region.

interlayer state density, or total state density.

A good way to approximate the electron-phonon coupling, and thus the electron scattering rate, could be by looking at the $\langle z \rangle$ of the electron density extending out from the atomic lattice, which should be unusually large for electrene materials given the physical separation of the conducting electrons from the atoms. $\langle z \rangle$ has been calculated for all monolayer and bilayer electrenes, and is presented in Fig. 3.34.

A study looking at the strain response of monolayer Ba_2N shows that this is a viable approximation of the coupling strenth, as it found that the electron-phonon coupling constant increases exponentially from λ=0.59 up to λ=1.49 for 4% tensile strain, and decreases down to around λ=0.45 at 2% compressive strain [50]. This agrees well with the results of $\langle z \rangle$ under strain for monolayer Ba_2N.

The general trend between electrenes seems to be that heavier elements have a larger $\langle z \rangle$ than lighter ones, though there are exceptions to this trend, as in Ba_2N. This is attributable to the decreasing electronegativity of heavier elements not binding electrons as tightly. We also see that bilayer surface states have a greater average distance than monolayer. This is likely due to the electrostatic repulsion of the higher density interlayer states. The values for bilayer increase with tensile strain (excluding Ba_2N), as do the monolayer values for Ca_2N and Sr_2N, which can be attributed to tensile strain reducing the thickness of the material and causing electrons to repel each other as charge density increases within and between the atomic layers. The calculated Poisson's ratios for all materials is included in Appendix A.

Monolayers other than Ca_2N and Sr_2N do not follow this strain behavior and instead display staggered or unresponsive trends, not changing much at all or occasionally dropping to lower values. As strain brings new states within the energy integration range, the ILDOS distribution will change, and in some cases will add states near the atomic layer since there is no large interlayer charge to repel the electrons, thereby resulting in a decrease in $\langle z \rangle$. This is most clearly illustrated in monolayer Sr_2P, where there is a subtantial increase of the ILODS in the vicinity of the lattice at +5% strain, resulting in a minimum value of $\langle z \rangle$.

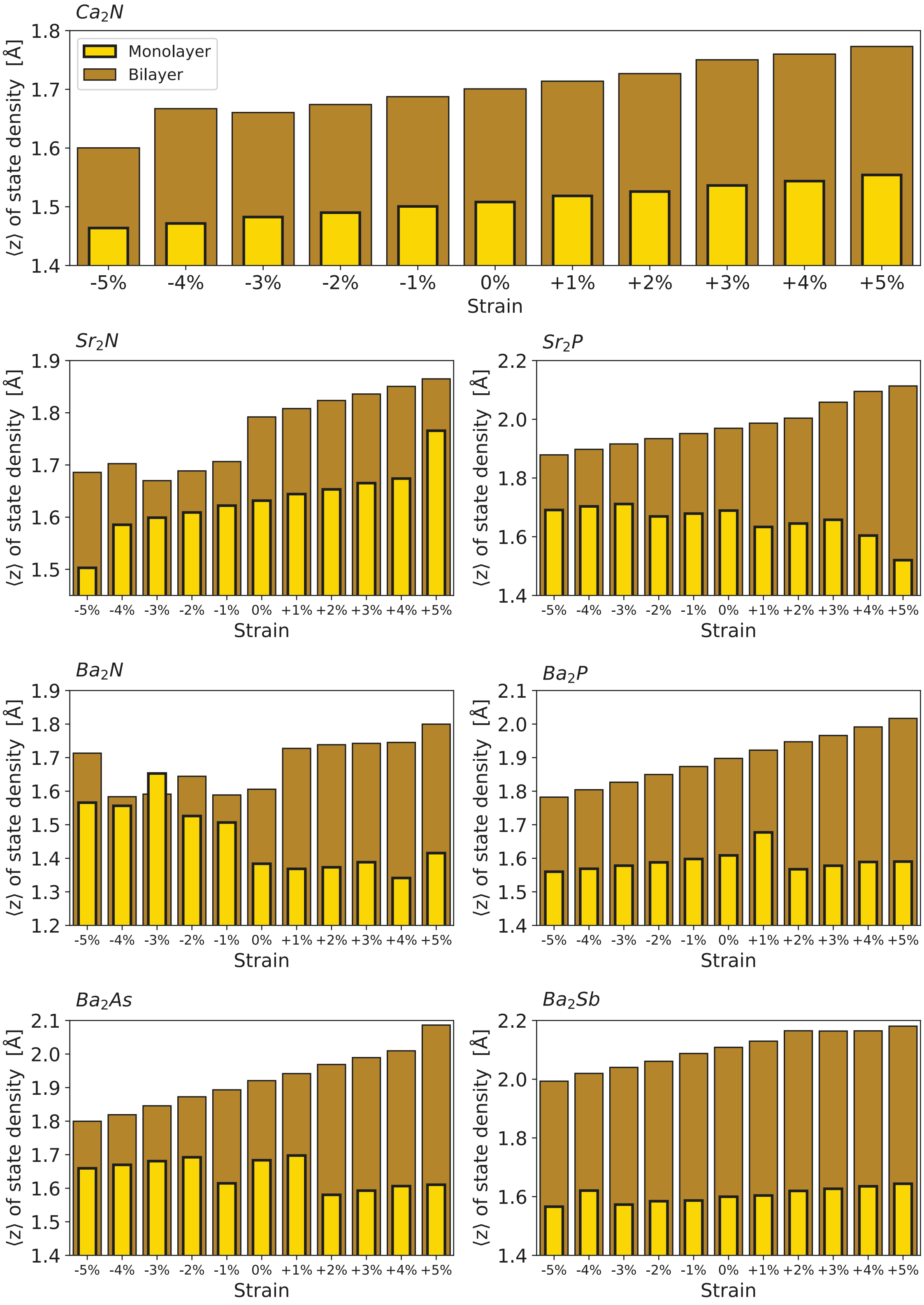

Figure 3.34: Average z position of surface state density relative to outer atomic layer versus strain.

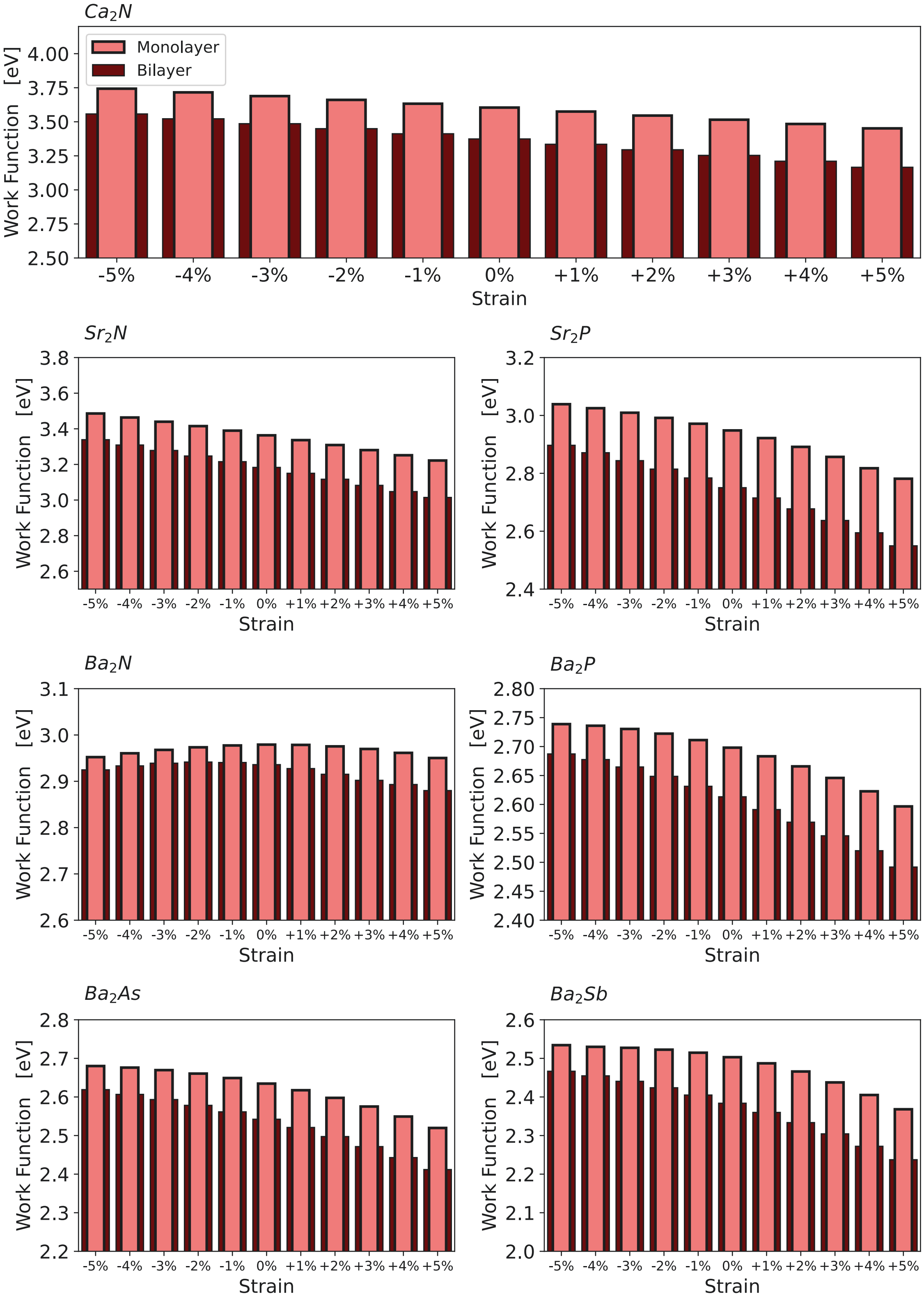

Figure 3.35: Work function of monolayer and bilayer electrenes versus strain.

3.4.3 Work Function

The work functions of all materials are shown in Fig. 3.35. The monolayer electrenes consistently have larger work functions over their bilayer counterparts, and lower response to strain. Bilayer Ca_2N and Sr_2P see the biggest decrease in the work function, by 0.2 eV for +5% in both cases. Lighter rare earth electrenes have higher work functions, possibly due to atoms with larger radii having weaker electron affinity, and so Ba_2Sb already had the lowest work function at 2.38 eV, and with this strain effect, the work function is reduced to 2.24 eV (the lowest calculated work function in this study).

Monolayer Ba_2X show a few features of note, the first being a variable change in the work function under different strain values. The trend for bilayer is a fairly linear change, but monolayer sees a leveling off of the work function to a steady value under compressive strain. This value is 2.74 eV for Ba_2P, 2.68 eV for Ba_2As, and 2.53 eV for Ba_2Sb. The strain response of Ba_2N is non-monotonic and displays a maximum value of 2.98 eV at 0% with monolayer and 2.94 eV at -2% with bilayer, but overall is relatively insensitive to strain.

The lower work functions for bilayer electrenes has previously [1] been attributed to the greater $\langle z \rangle$ of bilayer surface states; as electrons are pushed farther away from the lattice, it requires less energy to extract them. All electrenes follow a similar trend of decreasing work function as strain is increased. This correlates with the trend of increasing $\langle z \rangle$ with strain, as was previously found in Ref. [1]. To verify this, Fig. 3.36 presents a scatter plot of work function versus $\langle z \rangle$. A negative correlation is observed between these quantities, most clearly for bilayer electrenes.

Monolayer materials do not have as strong a correlation between work function and $\langle z \rangle$. This is most apparent in monolayer Sr_2P and Ba_2As, which has a weak positive correlation. However, this seems to have no effect on the trend of the work function which decreases irrespective of $\langle z \rangle$ up to +5% strain. In fact, Sr_2P has the highest proportional response to strain, seeing over 5% decrease in the work function compared to ∼4% for most other monolayer materials.

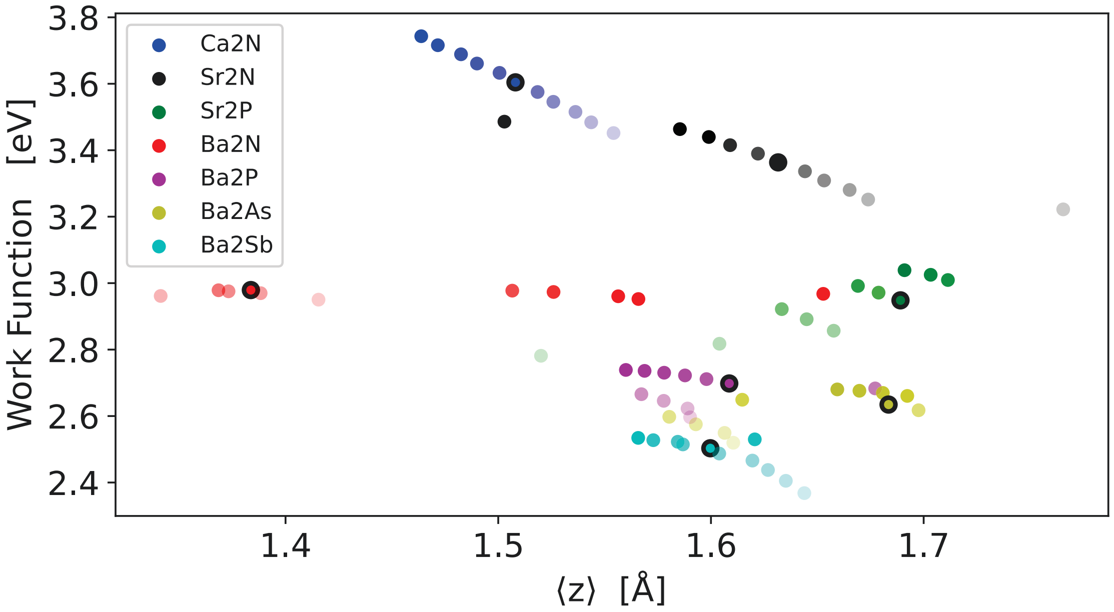

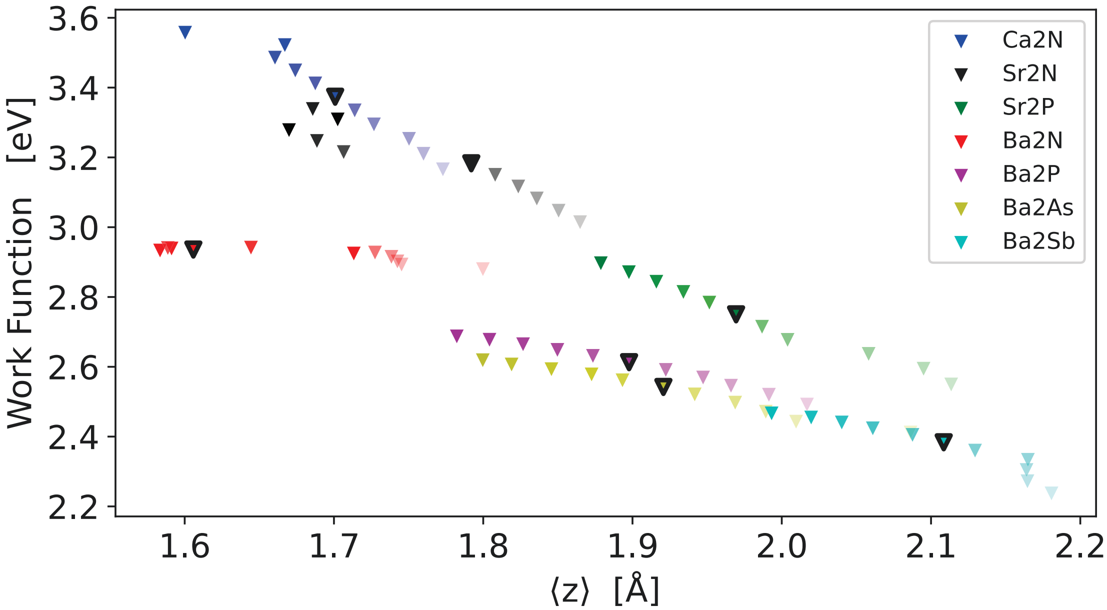

Figure 3.36: Work function versus $\langle z \rangle$ of surface state density as a function of strain for (top) monolayer electrenes and (bottom) bilayer electrenes. Strain is indicated by the opacity of the markers, with -5% strain plotted with most saturation and +5% strain plotted with least saturation. The unstrained case is indicated by a black outline.

Heavier elements have a much flatter trend between work function and $\langle z \rangle$, indicating that as the atomic radii increase, the range of the work function over ±5%

strain becomes smaller. The range of work function values over ±5% strain is only weakly connected to the range of $\langle z \rangle$ for monolayers, but more strongly correlated for bilayers. Ba_2N is an outlier as both a monolayer and a bilayer, showing almost no change in the work function for any strain value.

Chapter 4

Conclusions and Outlook

The appeal of electrene materials is obvious; the delocalized anionic electrons have the potential for high conductivity through low electron-phonon coupling, and their low work functions make them ideal electron donors. The goal of this study was to explore how these electrical properties could be manipulated via the application of tensile or compressive strain up to 5% in the family of layered, inorganic electrenes known as alkaline earth sub-pnictogenides, with the formula M_2X where M is an alkaline earth metal and X is a member of the pnictogen family of elements. This family includes the 7 electrenes: Ca_2N, Sr_2N, Sr_2P, Ba_2N, Ba_2P, Ba_2As, and Ba_2Sb.

The transport properties of these electrenes were examined using two indirect metrics: the state density in free-space regions of the material (surface and interlayer) and the average z position of surface state density relative to the surface of the atomic lattice. Electrical current is dependent on electron density, so looking at the surface and interlayer state density in the energy range near the Fermi level should indicate the density of electrons available for conduction which have a 2D delocalized distribution and low electron-phonon coupling. Under the assumption that having the transport states be physically separated from the lattice will reduce the scattering rates, the relative electron-phonon coupling strength is approximated by calculating the average distance of the surface state density from the atomic lattice.

Results show that the band structures of electrenes have varying responses to strain in the region of interest around the Fermi level. Some show little sensitivity to strain while others show a strong dependence. There is an underlying negative correlation in state density with strain due to a decrease of the area over which states are distributed, forcing them closer together and increasing their density, but this trend seems limited to changes of around 10% at most.

Materials that do see strong energy shifts in bands near the Fermi level see these shifts in states near to the M point of the Brillouin zone, displaying bands that can move across the Fermi level under strain. As a result, these materials can display noticeable increases in state density. Monolayer Ba_2N and Ba_2P see a surface state density increase of 0.015 states/$Å^2$ (corresponding to 56%) at -2% strain and 0.013 states/$Å^2$ (corresponding to 31%) at +2% strain, respectively. Such substantial increases can only be due to a significant proportion of new states entering the conduction range.

But what can't be forgotten is that these states are being manipulated at the M point, and M point states will not have the same spatial distribution as those delocalized states at the Γ point. The delocalized electron behavior that makes electrenes so interesting is broadly associated with the Fermi-crossing bands, however, weighted **k**-point results and analysis of the region very near to the Fermi level shows that the majority of the delocalized 2DEG-FS states likely exist near the bottom of these bands, closer to the Γ point. The states in the vicinity of the Fermi level, which control the transport properties, can be more localized than first expected, and may have increased scattering rates as a result.

The electron-phonon coupling, and thus the scattering rates, are inferred by looking at the average z of state density, and results show that $\langle z \rangle$ tends to trend up with tensile strain for most materials, though monolayer Sr_2P, Ba_2N, and Ba_2As show this trend reversed. So despite the protrusion of an M point feature into the conduction region of monolayer Sr_2P causing an increase in the surface state density under high tensile strain, the resulting decrease in $\langle z \rangle$ may hamper the transport efficiency of these new states due to higher scattering rates. The highest values of $\langle z \rangle$ are those for bilayer materials, being significantly higher than $\langle z \rangle$ for monolayers. The highest value of $\langle z \rangle$ is seen in bilayer Ba_2Sb under 5% tensile strain, where it reaches nearly 2.2 Å. A substantial increase of its interlayer state density of around 0.0075 states/$Å^2$ (corresponding to 58%) is also observed at +4% strain.

The biggest jump in $\langle z \rangle$ is for monolayer Ba_2N, where the average z increases by nearly 0.3 Å at -3% strain. This is paired with a roughly 0.01 states/$Å^2$ increase in the surface state density, which could make for a noticeable increase of conduction properties. The large increase in the surface states of monolayer Ba_2P on the other hand is paired with a minimal decrease of $\langle z \rangle$, on the order of half an Angstrom. Given the variability in the strain response of all materials, it is difficult to come to a conclusion about the best way to improve the conductivity of electrene materials as a group, but by balancing the individual responses of state density and $\langle z \rangle$ of each material, we can predict the most promising candidates for transport improvement.

Over all electrenes, the one with the lowest work function was found to be bilayer Ba_2Sb under 5% tensile strain with 2.24 eV. This follows the expected trend seen in electrenes for the work function; heavier elements will have greater radii which pushes surface electrons farther away from the lattice and more effectively screens the electrostatic potential, such that the surface electrons are less energetically bound. In addition, tensile strain compresses the material in the out-of-plane direction, causing electrons to be pushed out of the lattice and away from their binding atoms. The largest decrease observed due to strain was in bilayer Ca_2N and Sr_2P, where the work function fell by about 0.2 eV under +5% strain to around 3.2 eV and 2.5 eV, respectively.

Moving forward in the investigation of strain's effect on electrene materials, there are several unanswered questions that must be addressed. For instance, an increase in surface state density does not guarantee an increase in the conduction. A thorough treatment of the electron-phonon coupling of the M point states is needed before it can be decided if it is beneficial to bring these states into the conduction range over increasing state density using compressive strain. While this is possible, it remains a very computationally demanding task to undertake.

A first-principles study of monolayer Ba_2N demonstrates that it becomes dynamically unstable at 5% tensile strain, making any investigation of the scattering behavior beyond that point inconsequential [50]. In order to ensure that the results of this study are meaningful, and to focus future efforts, calculations must be performed to look at the instability point of all materials to find what range of strain values are physically plausible.

For example, a computational study looking at monolayer Ca_2N and Sr_2N predicts that under uniaxial loading, the ultimate strain point of the materials is between 14% and 24%, and 12% and 22%, respectively [49]. In addition, if electrenes are to be strain loaded for use in practical applications, it is important to know what kind of loading force is required. The study predicts stress values (reported in GPa·nm) of between 4.4 and 6.5 for Ca_2N, and between 3.1 and 4.7 for Sr_2N are required to achieve their ultimate strain point.

Another potential research avenue is to explore not only biaxial strain (i.e. uniform expansion or contraction), like we did here, but also uniaxial strain (apply strain along one of the in-plane directions) which might show different results. Given how the anionic electrons conform to the available free-space of the material, moving forward with strain engineering may involve folding or bending the lattice. Deforming the lattice in an out-of-plane direction could result in constructing regions of exceptionally high electron density where the surfaces of the electrene are brought closer together. This could result in even higher carrier concentrations available for low-scattering conduction or push states further out from the lattice, resulting in lower work function values.

As a last consideration, taking full advantage of the transport properties of electrenes may involve lowering the Fermi level to near the bottom of the surface bands, where the most desired transport states likely reside. Inoshita et al. [12] came to a similar conclusion in their computational study of the electride Y_2C, where they found that 2D confinement of the anionic electrons was improved at energy ranges further below the Fermi level, and suggested that increased mobility of interlayer electrons might be achieved by hole doping. Zeng et al. [28] likewise calculated that monolayer Ca_2N sees an enormous increase in carrier mobility of nearly 1500% if the Fermi level were lowered near the bottom of the surface band.

There are many difficulties associated with this proposition. Firstly, doping likely can't be used to achieve this outcome. The dopant concentrations needed would not be possible as doping is limited to roughly a few percent. Instead, electrene alloying may be able to reduce the surface and interlayer electrons. For example, something like $Ca_xK_{2-x}N$ where $x<2$, due to potassium being able to donate one less electron than calcium. This strategy would introduce scattering sites at the randomly distributed alloying atoms; practically unavoidable in an atomically thin material. While additional alloy scattering would be detrimental, the fact that the conduction states of the electrene are external to the lattice may help to alleviate this problem.

Identifying the proper alloy would be key to implementing this solution, but another route may be possible. A reliable method has yet to be found for stabilizing the highly reactive electrenes in ambient conditions, but one possibility is by confining it with another atomically-thin material. If a confining material can be found that accepts the right amount of charge without corrupting the band structure of the electrene, two design problems could be solved using a single solution. However, the confining material would have to be designed to take the proper amount of electrons from a notoriously eager donor without destroying the delocalized states altogether.

Bibliography

[1] Mohammad Rafiee Diznab, Erin R. Johnson, and Jesse Maassen. Periodic trends in the structural, electronic, and transport properties of electrenes. *Nanoscale*, 15:12038, 2023.

[2] James L. Dye. Electrides: Ionic Salts with Electrons as the Anions. *Science*, 247:663, 1990.

[3] G. Allan, M. G. De Backer, M. Lannoo, and I. Lefebvre. Why Do the Electrons Play the Role of Anions in the Electrides? *Europhysics Letters*, 11:49, 1990.

[4] Kimoon Lee, Sung Wng Kim, Yoshitake Toda, Satoru Matsuishi, and Hideo Hosono. Dicalcium nitride as a two-dimensional electride with an anionic electron layer. *Nature*, 494:336, 2013.

[5] M. A. Uijttewaal, G. A. de Wijs, and R. A. de Groot. Low work function of the (1000) Ca_2N surface. *Journal of Applied Physics*, 96:1751, 2004.

[6] Xiao Zhang, Zewen Xiao, Hechang Lei, Yoshitake Toda, Satoru Matsuishi, Toshio Kamiya, Shigenori Ueda, and Hideo Hosono. Two-Dimensional Transition-Metal Electride Y_2C. *Chemistry of Materials*, 26:6638, 2014.

[7] Jongho Park, Kimoon Lee, Seung Yong Lee, Chandani N. Nandadasa, Sungho Kim, Kyu Hyoung Lee, Young Hee Lee, Hideo Hosono, Seong-Gon Kim, and Sung Wng Kim. Strong Localization of Anionic Electrons at Interlayer for Electrical and Magnetic Anisotropy in Two-Dimensional Y_2C Electride. *Journal of the American Chemical Society*, 139:615, 2017.

[8] Takeshi Inoshita, Noriaki Hamada, and Hideo Hosono. Ferromagnetic instability of interlayer floating electrons in the quasi-two-dimensional electride Y_2C. *Physical Review B*, 92:201109, 2015.

[9] Aron Walsh and David O. Scanlon. Electron excess in alkaline earth sub-nitrides: 2D electron gas or 3D electride? *Journal of Materials Chemistry C*, 1:3525, 2013.

[10] Grigori V. Vajenine, Andrzej Grzechnik, Karl Syassen, Ingo Loa, Michael Hanfland, and Arndt Simon. Interplay of metallic and ionic bonding in layered subnitrides AE_2N (AE=Ca, Sr, or Ba) under high pressure. *Comptes Rendus Chimie*, 8:1897, 2005.

[11] Wenmei Ming, Mina Yoon, Mao-Hua Du, Kimoon Lee, and Sung Wng Kim. First-Principles Prediction of Thermodynamically Stable Two-Dimensional Electrides. *Journal of the American Chemical Society*, 138:15336, 2016.

[12] Takeshi Inoshita, Sehoon Jeong, Noriaki Hamada, and Hideo Hosono. Exploration for Two-Dimensional Electrides via Database Screening and Ab Initio Calculation. *Physical Review X*, 4:031023, 2014.

[13] Y. Mudryk, Durga Paudyal, V. K. Pecharsky, and K. A. Gschneidner. Magnetic properties of Gd_2C: Experiment and first principles calculations. *Journal of Applied Physics*, 109:07A924, 2011.

[14] Masao Atoji. Neutron-diffraction studies of Tb_2C and Dy_2C in the temperature range 4-296 k. *The Journal of Chemical Physics*, 75:1434, 1981.

[15] Masao Atoji. Neutron-diffraction study of Ho_2C at 4-296 k. *The Journal of Chemical Physics*, 74:1893, 1981.

[16] Seung Yong Lee, Jae-Yeol Hwang, Jongho Park, Chandani N. Nandadasa, Younghak Kim, Joonho Bang, Kimoon Lee, Kyu Hyoung Lee, Yunwei Zhang, Yanming Ma, Hideo Hosono, Young Hee Lee, Seong-Gon Kim, and Sung Wng Kim. Ferromagnetic quasi-atomic electrons in two-dimensional electride. *Nature Communications*, 11:1526, 2020.

[17] Shuyuan Liu, Wei Li, Sung Wng Kim, and Jin-Ho Choi. Decisive Role of Interlayer Ionic Couplings for the Electronic Properties of Two-Dimensional Layered Electrides. *The Journal of Physical Chemistry C*, 124:1398, 2020.

[18] Xiaoming Zhang, Weizhen Meng, Ying Liu, Xuefang Dai, and Goudong Liu. Magnetic Electrides: High-Throughput Material Screening, Intriguing Properties, and Applications. *Journal of the American Chemical Society*, 145:5523, 2023.

[19] Qiang Zhu, Timofey Frolov, and Kamal Choudhary. Computational Discovery of Inorganic Electrides from an Automated Screening. *Matter*, 1:1293, 2019.

[20] Lauren M. McRae, Rebecca C. Radomsky, Jacob T. Pawlik, Daniel L. Druffel, Jack D. Sundberg, Matthew G. Lanetti, Carrie L. Donley, Kelly L. White, and Scott C. Warren. Sc_2C, a 2D Semiconducting Electride. *Journal of the American Chemical Society*, 144:10862, 2022.

[21] Daniel L. Druffel, Kaci L. Kuntz, Adam H. Woomer, Francis M. Alcorn, Jun Hu, Carrie L. Donley, and Scott C. Warren. Experimental Demonstration of an Electride as a 2D Material. *Journal of the American Chemical Society*, 138:16089, 2016.

[22] Eugene S. Kadantsev and Pawel Hawrylak. Electronic structure of a single MoS_2 monolayer. *Solid State Communications*, 152:909, 2012.

[23] Songtao Zhao, Zhenyu Li, and Jinlong Yang. Obtaining Two-Dimensional Electron Gas in Free Space without Resorting to Electron Doping: An Electride Based Design. *Journal of the American Chemical Society*, 136:13313, 2014.

[24] Shan Guan, Shengyuan A. Yang, Liyan Zhu, Junping Hu, and Yugui Yao. Electronic, Dielectric, and Plasmonic Properties of Two-Dimensional Electride Materials X_2N (X=Ca, Sr): A First-Principles Study. *Scientific Reports*, 5:12285, 2015.

[25] M. Kitano, Y. Inoue, Y. Yamazaki, F. Hayashi, S. Kanbara, S. Matsuishi, T. Yokoyama, S. W. Kim, M. Hara, and H. Hosono. Ammonia synthesis using a stable electride as an electron donor and reversible hydrogen store. *Nature Chemistry*, 4:934, 2012.

[26] Tuğbey Kocabaş, Ayberk Özden, İlker Demiroğlu, Deniz Çakır, and Cem Sevik. Determination of Dynamically Stable Electrenes toward Ultrafast Charging Battery Applications. *The Journal of Physical Chemistry Letters*, 9:4267, 2018.

[27] Takeshi Inoshita, Seiji Takemoto, Tomofumi Tada, and Hideo Hosono. Surface electron states on the quasi-two-dimensional excess-electron compounds Ca_2N and Y_2C. *Physical Review B*, 95:165430, 2017.

[28] Xiongzhi Zeng, Songtao Zhao, Zhenyu Li, and Jinlong Yang. Electron-phonon interaction in a Ca_2N monolayer: Intrinsic mobility of electrene. *Physical Review B*, 98:155443, 2018.

[29] A. K. Geim and Novoselov K. S. The rise of graphene. *Nature Materials*, 6:183, 2007.

[30] Jinwoong Chae, Junsu Lee, Youngtek Oh, and Gunn Kim. First-principles study of two-dimensional electron gas on a layered Gd_2C electride surface. *Physical Review B*, 104:125403, 2021.

[31] Ye Ji Kim, Sun Min Kim, Eun Jin Cho, Hideo Hosono, Jung Woon Yang, and Sung Wng Kim. Two dimensional inorganic electride-promoted electron transfer efficiency in transfer hydrogenation of alkynes and alkenes. *Chemical Science*, 6:3577, 2015.

[32] Mini Mol Menamparambath, Jong-Ho Park, Ho-Sung Yoo, Shashikant P. Patole, Ji-Beom Yoo, Sung Wng Kim, and Seunghyun Baik. Large work function difference driven electron transfer from electrides to single-walled carbon nanotubes. *Nanoscale*, 6:8844, 2014.

[33] Sera Kim, Seunghyun Song, Jongho Park, Ho Sung Yu, Suyeon Cho, Dohyun Kim, Jaeyoon Baik, Duk-Hyun Choe, K. J. Chang, Young Hee Lee, Sung Wng Kim, and Heejun Yang. Long-Range Lattice Engineering of $MoTe_2$ by a 2D Electride. *Nano Letters*, 17:3363, 2017.

[34] Ki-Beom Kim, Maiko Kikuchi, Masashi Miyakawa, Hiroshi Yanagi, Toshio Kamiya, Masahiro Hirano, and Hideo Hosono. Photoelectron Spectroscopic Study of C12A7:e^- and Alq_3 Interface: The Formation of a Low Electron-Injection Barrier. *The Journal of Physical Chemistry C*, 111:8403, 2007.

[35] Junping Hu, Bo Xu, Shengyuan A. Yang, Shan Guan, Chuying Ouyang, and Yugui Yao. 2D Electrides as Promising Anode Materials for Na-Ion Batteries from First-Principles Study. *ACS Applied Materials & Interfaces*, 7:24016, 2015.

[36] Fouad Kaadou, Jesse Maassen, and Erin R. Johnson. Improved Charge Transfer and Barrier Lowering Across a Au-MoS_2 Interface Through the Insertion of a Layered Ca_2N Electride. *The Journal of Physical Chemistry C*, 125:11656, 2021.

[37] P.H. Tai, C.H. Jung, Y.K. Kang, and D.H. Yoon. Electrical and optical properties of $12CaO{\cdot}7Al_2O_3$ electride doped indium tin oxide thin film deposited by RF magnetron co-sputtering. *Thin Solid Films*, 517:6294, 2009.

[38] Changgu Lee, Xiaoding Wei, Jeffrey W Kysar, and James Hone. Measurement of the Elastic Properties and Intrinsic Strength of Monolayer Graphene. *Science*, 321:385, 2008.

[39] Emiliano Cadelano, Pier Palla, Stefano Giordano, and Luciano Colombo. Nonlinear Elasticity of Monolayer Graphene. *Physical Review Letters*, 102:235502, 2009.

[40] Keliang He, Charles Poole, Kin Mak, and Jie Shan. Experimental Demonstration of Continuous Electronic Structure Tuning via Strain in Atomically Thin MoS_2. *Nano Letters*, 13:2931, 2013.

[41] Sujay Desai, Gyungseon Seol, Jeong Kang, Hui Fang, Corsin Battaglia, Rehan Kapadia, Joel Ager, Jing Guo, and Ali Javey. Strain-Induced Indirect to Direct Bandgap Transition in Multilayer WSe_2. *Nano Letters*, 14:4592, 2014.

[42] Yanlong Wang, C. Cong, Ruixiang Fei, Yang Weihuang, Yu Chen, Bingchen Cao, Li Yang, and Ting Yu. Remarkable anisotropic phonon response in uniaxially strained few-layer black phosphorus. *Nano Research*, 8:3944, 2015.

[43] Hongliang Shi, Hui Pan, Yong-Wei Zhang, and Boris Yakobson. Quasiparticle band structures and optical properties of strained monolayer MoS_2 and WS_2. *Physical Review B*, 87:155304, 2012.

[44] Wu Meng, Jun-Jie Shi, Min Zhang, Yimin Ding, Hui Wang, Yu-lang Cen, and Jing Lu. Enhancement of photoluminescence and hole mobility in 1- to 5-layer InSe due to the top valence-band inversion: strain effect. *Nanoscale*, 10:11441, 2018.

[45] Gui Wang, Zhuang Ma, Jing-Wen Jiang, Jing-kai Yang, Yi-Ling Sun, Zheng-Fang Qian, Pu Huang, Peng Zhang, and Su-Huai Wei. Crystal Structures and Physicochemical Properties of Be_2N and Mg_2N as Electride Materials. *Physical Review Applied*, 19:034014, 2023.

[46] Gui Wang, Yongle Zhong, Yiguo Xu, Zhengfang Qian, Jingwen Jiang, and Zhuang Ma. Transition from semiconductor to conductor of a Mg_2N electride induced by strain. *Physical Chemistry Chemical Physics*, 25:17300, 2023.

[47] Zenner S. Pereira, Giovani M. Faccin, and E. Z. da Silva. Strain-induced multigap superconductivity in electrene Mo_2N: a first principles study. *Nanoscale*, 14:8594, 2022.

[48] Yanfeng Ge, Shan Guan, and Yong Liu. Two dimensional superconductors in electrides. *New Journal of Physics*, 19:123020, 2017.

[49] Bohayra Mortazavi, Golibjon R. Berdiyorov, Masoud Shahrokhi, and Timon Rabczuk. Mechanical, optoelectronic and transport properties of single-layer Ca_2N and Sr_2N electrides. *Journal of Alloys and Compounds*, 739:643, 2018.

[50] Xiao-Le Qiu, Jian-Feng Zhang, Huan-Cheng Yang, Zhong-Yi Lu, and Kai Liu. Superconductivity in monolayer Ba_2N electride: First-principles study. *Physical Review B*, 105:165101, 2022.

[51] Felix Bloch. Über die Quantenmechanik der Elektronen in Kristallgittern. *Zeitschrift für Physik*, 52:555, 1929.

[52] P. Hohenberg and W. Kohn. Inhomogeneous Electron Gas. *Physical Review*, 136:B864, 1964.

[53] W. Kohn and L. J. Sham. Self-Consistent Equations Including Exchange and Correlation Effects. *Physical Review*, 140:A1133, 1965.

[54] Paolo Giannozzi, Stefano Baroni, Nicola Bonini, Matteo Calandra, Roberto Car, Carlo Cavazzoni, Davide Ceresoli, Guido L. Chiarotti, Matteo Cococcioni, Ismaila Dabo, Andrea Dal Corso, Stefano Fabris, Guido Fratesi, Stefano de Gironcoli, Ralph Gebauer, Uwe Gerstmann, Christos Gougoussis, Anton Kokalj, Michele Lazzeri, Layla Martin-Samos, Nicola Marzari, Francesco Mauri, Riccardo Mazzarello, Stefano Paolini, Alfredo Pasquarello, Lorenzo Paulatto, Carlo Sbraccia, Sandro Scandolo, Gabriele Sclauzero, Ari P. Seitsonen, Alexander Smogunov, Paolo Umari, and Renata M. Wentzcovitch. Quantum Espresso: a modular and open-source software project for quantum simulations of materials. *Journal of Physics: Condensed Matter*, 21:395502, 2009.

[55] D. D. Johnson. Modified Broyden's method for accelerating convergence in self-consistent calculations. *Physical Review B*, 38:12807, 1988.

[56] R. P. Feynman. Forces in Molecules. *Physical Review*, 56:340, 1939.

[57] O. H. Nielsen and Richard M. Martin. Quantum-mechanical theory of stress and force. *Physical Review B*, 32:3780, 1985.

[58] A. van de Walle and G. Ceder. Correcting overbinding in local-density-approximation calculations. *Physical Review B*, 59:14992, 1999.

[59] A. D. Becke. Density-functional exchange-energy approximation with correct asymptotic behavior. *Physical Review A*, 38:3098, 1988.

[60] John P. Perdew, Kieron Burke, and Matthias Ernzerhof. Generalized Gradient Approximation Made Simple. *Physical Review Letters*, 77:3865, 1996.

[61] Jianmin Tao, John P. Perdew, Viktor N. Staroverov, and Gustavo E. Scuseria. Climbing the Density Functional Ladder: Nonemperical Meta-Generalized Gradient Approximation Designed for Molecules and Solids. *Physical Review Letters*, 91:146401, 2003.

[62] Axel D. Becke. Density-functional thermochemistry. III. The role of exact exchange. *The Journal of Chemical Physics*, 98:5648, 1993.

[63] Henrik Rydberg, Bengt Lundqvist, David Langreth, and Maxime Dion. Tractable nonlocal correlation density functionals for flat surfaces and slabs. *Physical Review B*, 62:6997, 2000.

[64] Stefan Grimme, Jens Antony, Stephan Ehrlich, and Helge Krieg. A consistent and accurate ab initio parametrization of density functional dispersion correction (DFT-D) for the 94 elements H-Pu. *The Journal of Chemical Physics*, 132:154104, 2010.

[65] Axel D. Becke and Erin R. Johnson. A unified density-functional treatment of dynamical, nondynamical, and dispersion correlations. *The Journal of Chemical Physics*, 127:124108, 2007.

[66] A. Otero-de-la Roza and Erin R. Johnson. Application of XDM to ionic solids: The importance of dispersion for bulk moduli and crystal geometries. *The Journal of Chemical Physics*, 153:054121, 2020.

[67] Axel D. Becke and Erin R. Johnson. Exchange-hole dipole moment and the dispersion interaction. *The Journal of Chemical Physics*, 122:154104, 2005.

[68] Stefan Grimme, Stephan Ehrlich, and Lars Goerigk. Effect of the damping function in dispersion corrected density functional theory. *Journal of Computational Chemistry*, 32:1456, 2011.

[69] Hendrik J. Monkhorst and James D. Pack. Special points for Brillouin-zone integrations. *Physical Review B*, 13:5188, 1976.

[70] Nicola Marzari, David Vanderbilt, Alessandro De Vita, and M. C. Payne. Thermal Contraction and Disordering of the Al(110) Surface. *Physical Review Letters*, 82:3296, 1999.

[71] Peter E. Blöchl, O. Jepsen, and O. K. Andersen. Improved tetrahedron method for Brillouin-zone integrations. *Physical Review B*, 49:16223, 1994.

[72] J. C. Slater and G. F. Koster. Simplified LCAO Method for the Periodic Potential Problem. *Physical Review*, 94:1498, 1954.

[73] Richard M. Martin. *Electronic structure: basic theory and practical methods.* Cambridge University Press, 2010.

[74] Christopher J. Cramer. *Essentials of Computational Chemistry.* John Wiley & Sons, second edition, 2004.

[75] William C. Topp and John J. Hopfield. Chemically Motivated Pseudopotential for Sodium. *Physical Review B*, 7:1295, 1973.

[76] Andrea Dal Corso. Pseudopotentials periodic table: From H to Pu. *Computational Materials Science*, 95:337, 2014.

[77] David Vanderbilt. Soft self-consistent pseudopotentials in a generalized eigenvalue formalism. *Physical Review B*, 41:7892, 1990.

[78] Jianjun Wang, Lin Li, Ziting Shen, Peng Guo, Meng Li, Bin Zhao, Lili Fang, and Linfeng Yang. Ultralow Interlayer Friction of Layered Electride Ca_2N: A Potential Two-Dimensional Solid Lubricant Material. *Materials*, 11:2462, 2018.

[79] Raseong Kim, Supriyo Datta, and Mark S. Lundstrom. Influence of dimensionality on thermoelectric device performance. *Journal of Applied Physics*, 105:034506, 2009.

[80] Damien Voiry, Aditya Mohite, and Manish Chhowalla. Phase engineering of transition metal dichalcogenides. *Chemical Society Reviews*, 44:2702, 2015.

[81] Kin Fai Mak, Changgu Lee, James Hone, Jie Shan, and Tony F. Heinz. Atomically Thin MoS_2: A New Direct-Gap Semiconductor. *Physical Review Letters*, 105:136805, 2010.

[82] B. Radisavljevic, A. Radenovic, J. Brivio, V. Giacometti, and A. Kis. Single-layer MoS_2 transistors. *Nature Nanotechnology*, 6:147, 2011.

[83] Lina Liu, Juanxia Wu, Liyuan Wu, Meng Ye, Xiaozhi Liu, Qian Wang, Siyao Hou, Pengfei Lu, Lifei Sun, Jingying Zheng, Lei Xing, Lin Gu, Xiangwei Jiang, Liming Xie, and Liying Jiao. Phase-selective synthesis of 1T' MoS_2 monolayers and heterophase bilayers. *Nature Materials*, 17:1108, 2018.

[84] Dipankar Saha and Peter Kruse. Editors' Choice—Review—Conductive Forms of MoS_2 and Their Applications in Energy Storage and Conversion. *Journal of The Electrochemical Society*, 167:126517, 2020.

[85] Hai He, Pengfei Lu, Liyuan Wu, Chunfang Zhang, Yuxin Song, Pengfei Guan, and Shumin Wang. Structural Properties and Phase Transition of Na Adsorption on Monolayer MoS_2. *Nonoscale Research Letters*, 11:330, 2016.

[86] Wei Xu, Shiming Yan, and Wen Qiao. Magnetism in monolayer 1T-MoS_2 and 1T-MoS_2H tuned by strain. *RSC Advances*, 8:8435, 2018.

[87] Qing Tang and De-en Jiang. Stabilization and Band-Gap Tuning of the 1T-MoS_2 Monolayer by Covalent Functionalization. *Chemistry of Materials*, 27:3743, 2015.

Appendix A

Poisson's Ratios

Material	-5%	-4%	-3%	-2%	-1%	+1%	+2%	+3%	+4%	+5%
Ca_2N	2.34	2.35	2.36	2.37	2.37	2.38	2.38	2.39	2.39	2.39
Sr_2N	2.28	2.28	2.28	2.28	2.29	2.28	2.29	2.30	2.30	2.30
Sr_2P	1.47	1.46	1.44	1.42	1.41	1.36	1.33	1.30	1.27	1.24
Ba_2N	2.58	2.57	2.55	2.53	2.52	2.47	2.45	2.42	2.39	2.37
Ba_2P	1.48	1.46	1.44	1.42	1.40	1.36	1.34	1.31	1.28	1.26
Ba_2As	1.37	1.36	1.34	1.32	1.30	1.26	1.24	1.21	1.18	1.15
Ba_2Sb	1.14	1.12	1.10	1.09	1.06	1.01	0.99	0.96	0.92	0.90

Table A.1: Poisson's ratios of all monolayer electrenes versus strain. Calculated as the negative ratio of in-plane strain to out-of-plane strain.

Material	-5%	-4%	-3%	-2%	-1%	+1%	+2%	+3%	+4%	+5%
Ca_2N	1.06	1.05	1.04	1.03	1.02	1.01	1.00	0.98	0.97	0.96
Sr_2N	1.12	1.11	1.11	1.10	1.09	1.06	1.06	1.05	1.04	1.03
Sr_2P	0.65	0.64	0.64	0.63	0.62	0.60	0.59	0.58	0.57	0.55
Ba_2N	0.92	0.92	0.92	0.92	0.91	0.93	0.93	0.93	0.93	0.93
Ba_2P	0.67	0.67	0.66	0.65	0.64	0.63	0.62	0.61	0.60	0.59
Ba_2As	0.63	0.62	0.62	0.61	0.60	0.58	0.58	0.57	0.56	0.54
Ba_2Sb	0.53	0.53	0.52	0.51	0.50	0.49	0.47	0.46	0.45	0.43

Table A.2: Poisson's ratios of all bilayer electrenes versus strain. Calculated as the negative ratio of in-plane strain to out-of-plane strain.

Appendix B

Electrostatic Potential Energy

The electric potentials in Fig. B.1 all have the same response to strain as Ca_2N, and it is clear that the biggest factor affecting electric potential is the choice of pnictogen. Nitrogen has the deepest potential well, which then shrinks as you go to heavier elements. The results for the bilayer electric potential in Fig. B.2 are much the same.

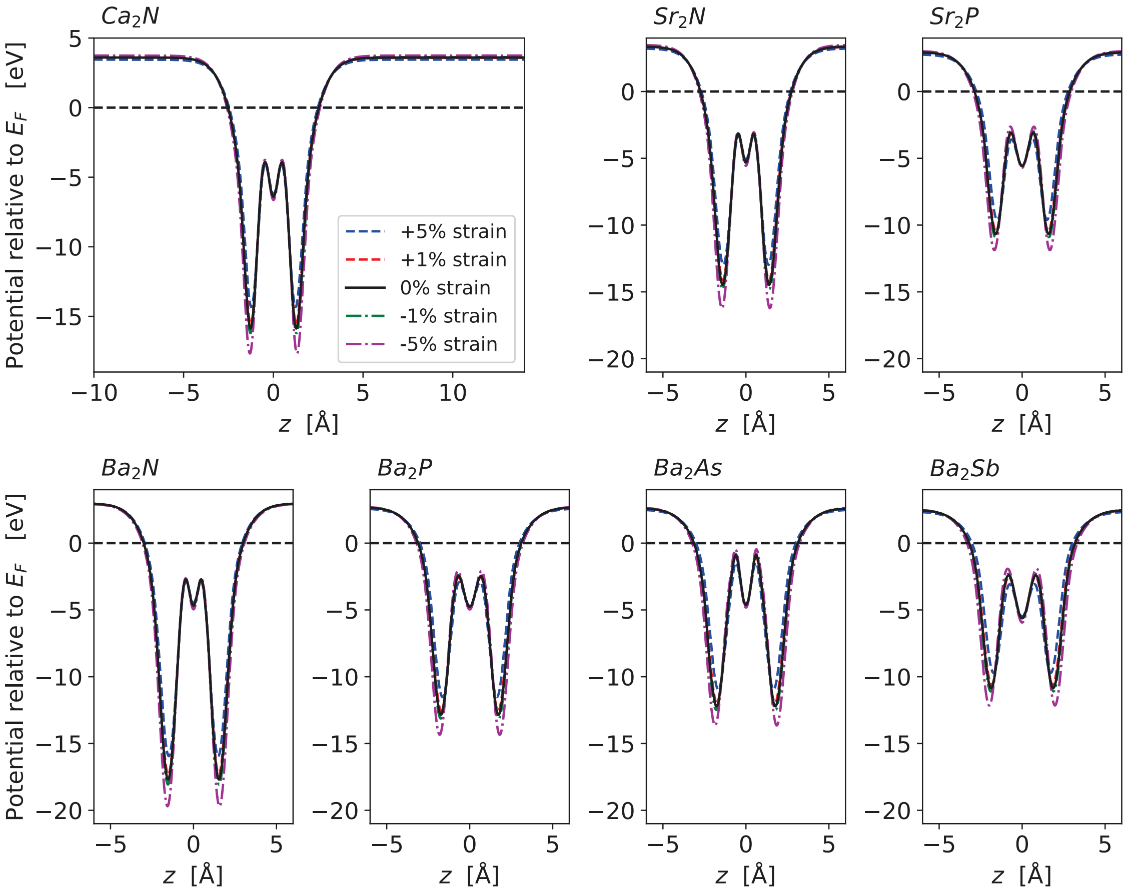

Figure B.1: Planar averaged electrostatic potential energy relative to the Fermi level for all monolayer electrenes as a function of strain.

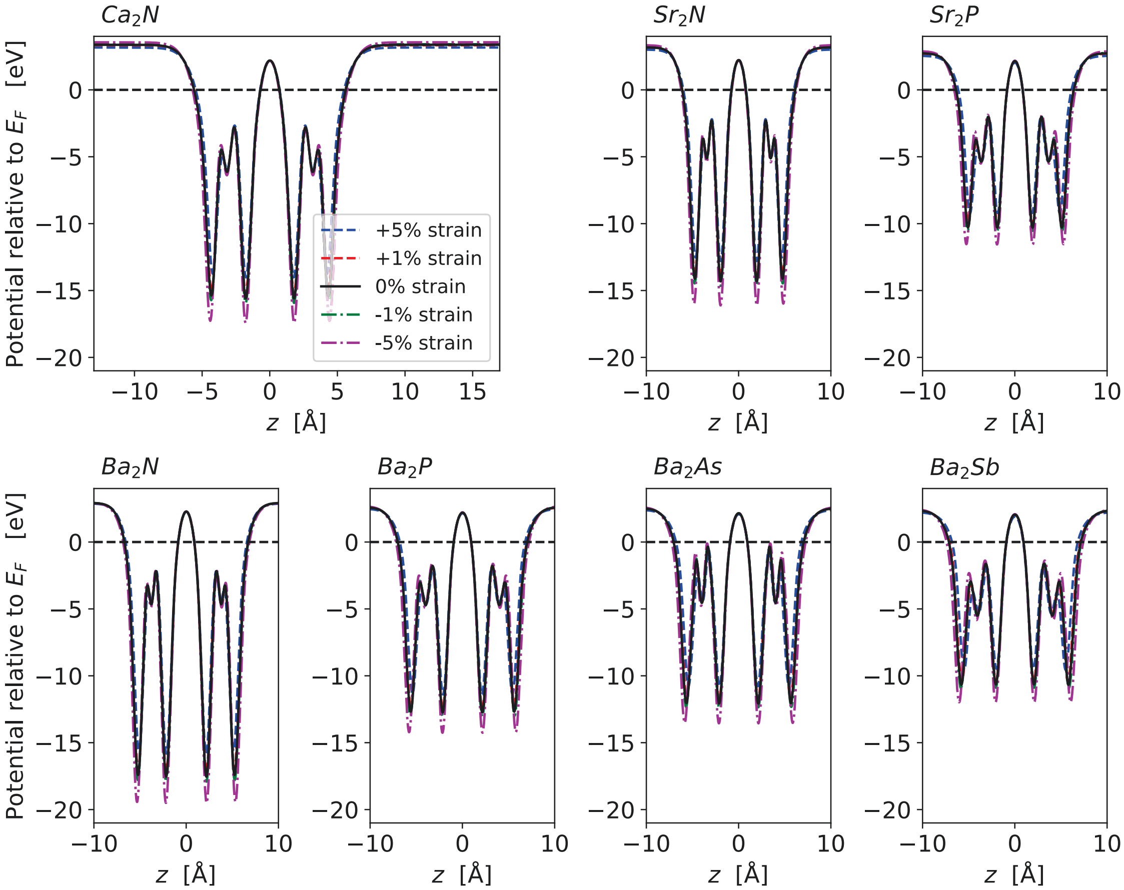

Figure B.2: Planar averaged electrostatic potential energy relative to the Fermi level for all bilayer electrenes as a function of strain.

Appendix C

k-Resolved Electron Density

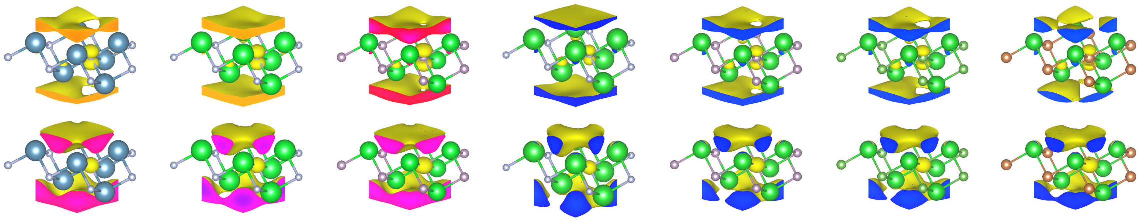
(a) Ca_2N (b) Sr_2N (c) Sr_2P (d) Ba_2N (e) Ba_2P (f) Ba_2As (g) Ba_2Sb

Figure C.1: The **k**-resolved charge distribution of all unstrained monolayer materials at the Γ point. The top and bottom images correspond to the upper and lower energy surface bands, respectively.

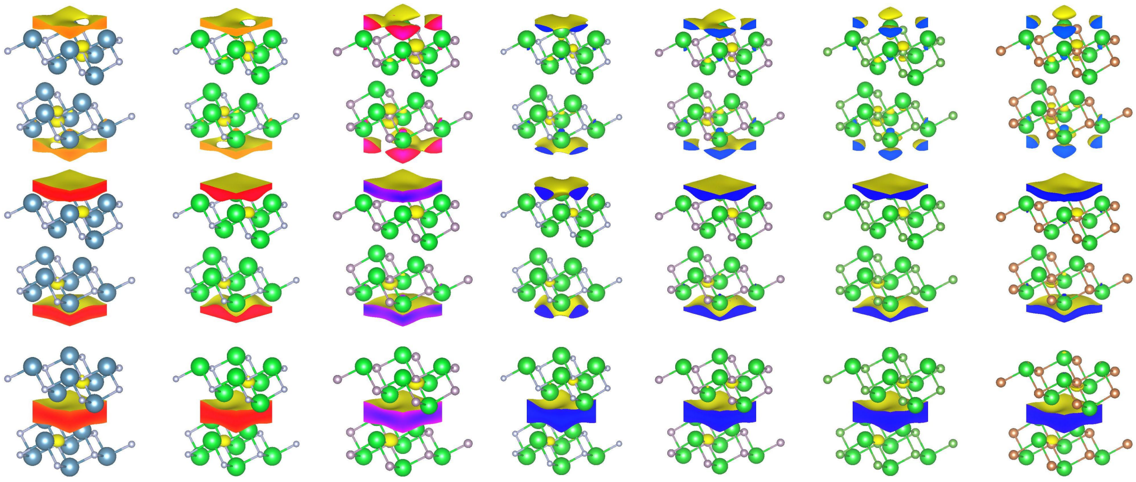
(a) Ca_2N (b) Sr_2N (c) Sr_2P (d) Ba_2N (e) Ba_2P (f) Ba_2As (g) Ba_2Sb

Figure C.2: The **k**-resolved charge distribution of all unstrained bilayer materials at the Γ point. The top, middle, and bottom images correspond to the upper surface, lower surface, and interstitial bands, respectively.

Figures C.1 and C.2 show the **k**-resolved electron density for the surface and interlayer bands at the Γ point. The Ba_2X series have 2DEG-FS layers that are less continuous than other materials, indicating that the Ba_2X series has less effective conductive states than Ca_2N or Sr_2X.

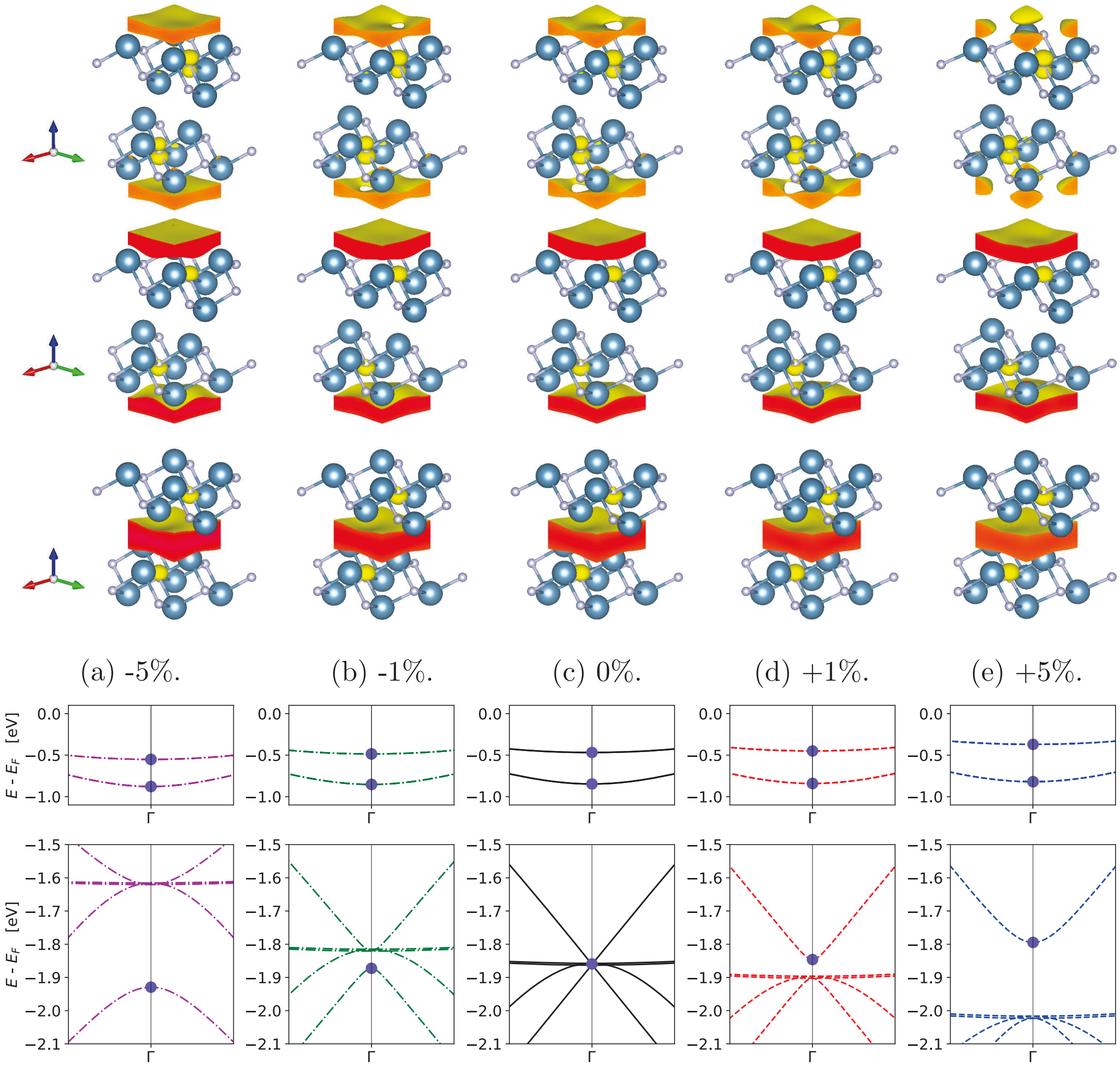
(a) -5%. (b) -1%. (c) 0%. (d) +1%. (e) +5%.

Figure C.3: The **k**-resolved state distribution of bilayer Ca_2N at the Γ point versus strain.

Figure C.3 shows how the **k**-resolved charge density evolves with strain in bilayer Ca_2N. Of note is how the top most surface state becomes discontinuous by +5% strain, though the most dramatic change is the shift in the interlayer band character. For strain ≥0%, the interlayer 2DEG character is the third Fermi-crossing band, but when negative strain is applied that character shifts to the concave band at -2 eV. The cause of this radical change in band character is uncertain, but may be related to the fact all bands between those of 2DEG-FS character in negative strain cases are degenerate with another band at the Γ point.

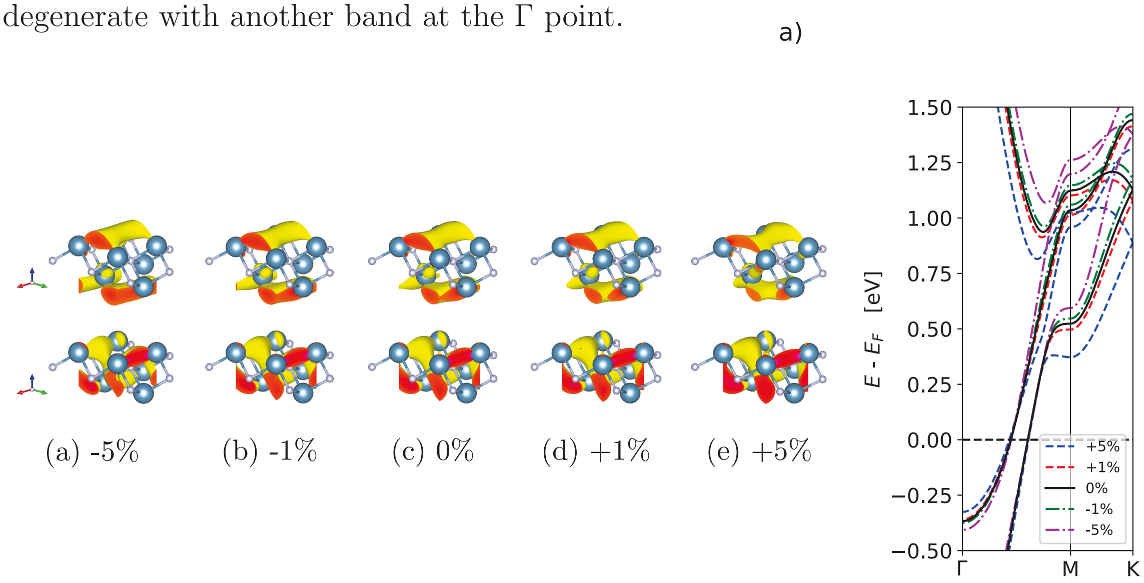

Figure C.4: Ca_2N monolayer **k**-point resolved charge distribution for bands at the M point. Images correspond to order of bands shown on the right.

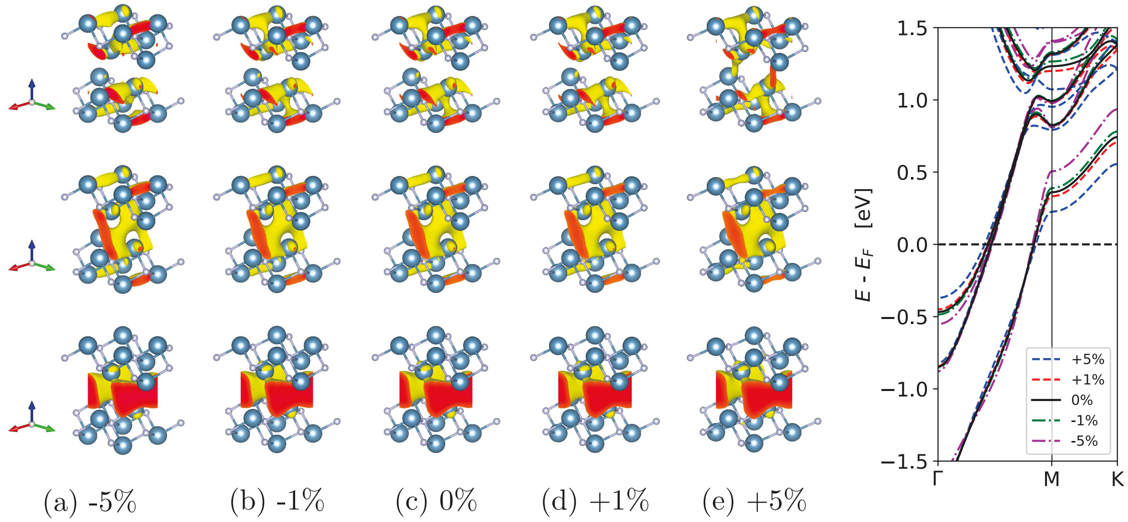

Figure C.5: Ca_2N bilayer **k**-point resolved charge distribution for bands at the M point. Images correspond to order of bands shown on the right.

The most amount of energy shift in the bands is observed at the M point, so the states at this point have been evaluated. Figure C.4 and Fig. C.5 show the **k**-resolved electron density of the surface and interlayer bands at the M point for

Ca_2N monolayer and bilayer. They show a very different density character than the 2DEG-FS that is expected for electrenes.

The Fermi-crossing bands no longer fill the free space layers and now exist at least in part or entirely within the atomic lattice. The states that exist in the lattice seem to take on the characteristics of p-orbital bonds. The interlayer band of the bilayer seems to no longer be those of a 2D confined electron gas, but is partitioned into seemingly 1D channels. This is also seen in the monolayer band. This might produce asymmetric transport properties in these states. The middle bilayer band also now has states which connect the two atomic layers, giving it more interlayer character than surface layer character previously observed at the Γ point. What these results demonstrate is that the electron density evolves dramatically over the length of a band.

What is noticeable about the 1D channels is that they appear to be orientated along the cell vector $\mathbf{a}$. This anisotropy seems to arise from the nature of the M-point, which lies directly on the k_y axis of reciprocal space. The cell vector $\mathbf{a}$ lies directly on the x axis in real space, indicating that the momentum of electron states at the M-point is exactly perpendicular to the orientation of the 1D channels seen in the figures.

Appendix D

Total Energy Under Strain

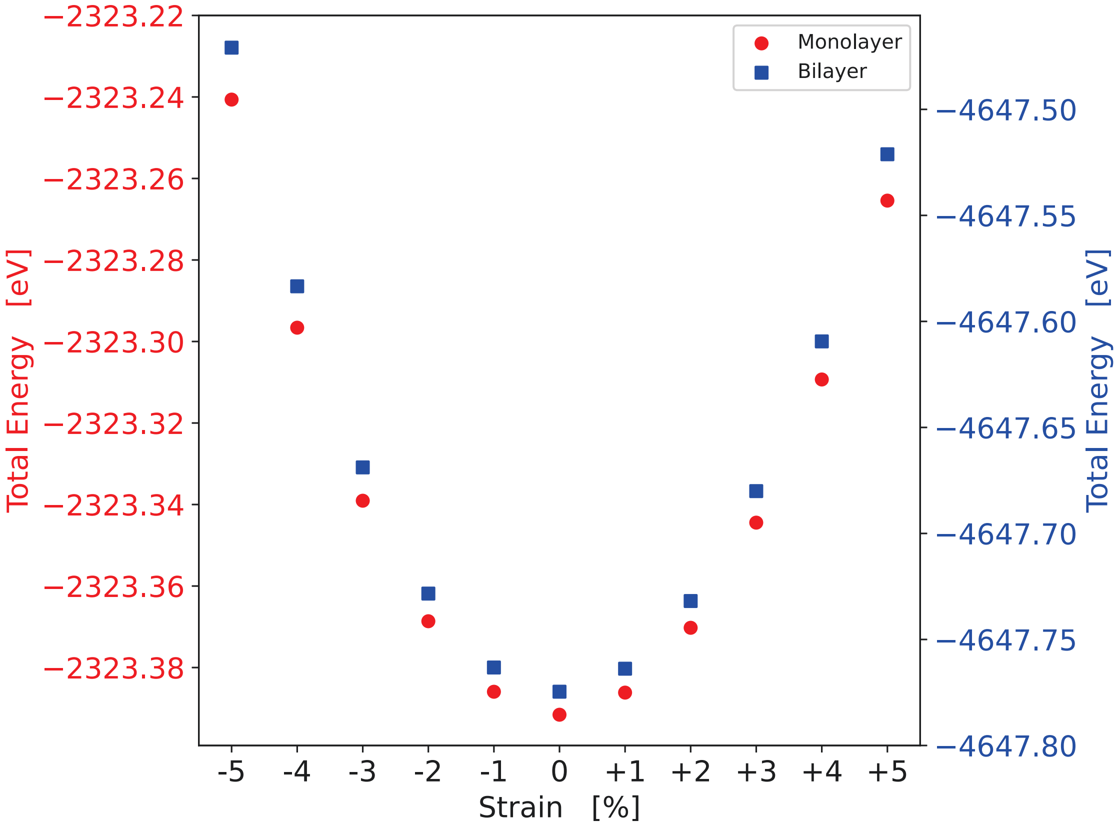

Figure D.1: The calculated total energy of Ca_2N monolayer (left axis) and bilayer (right axis) at tested strain values.

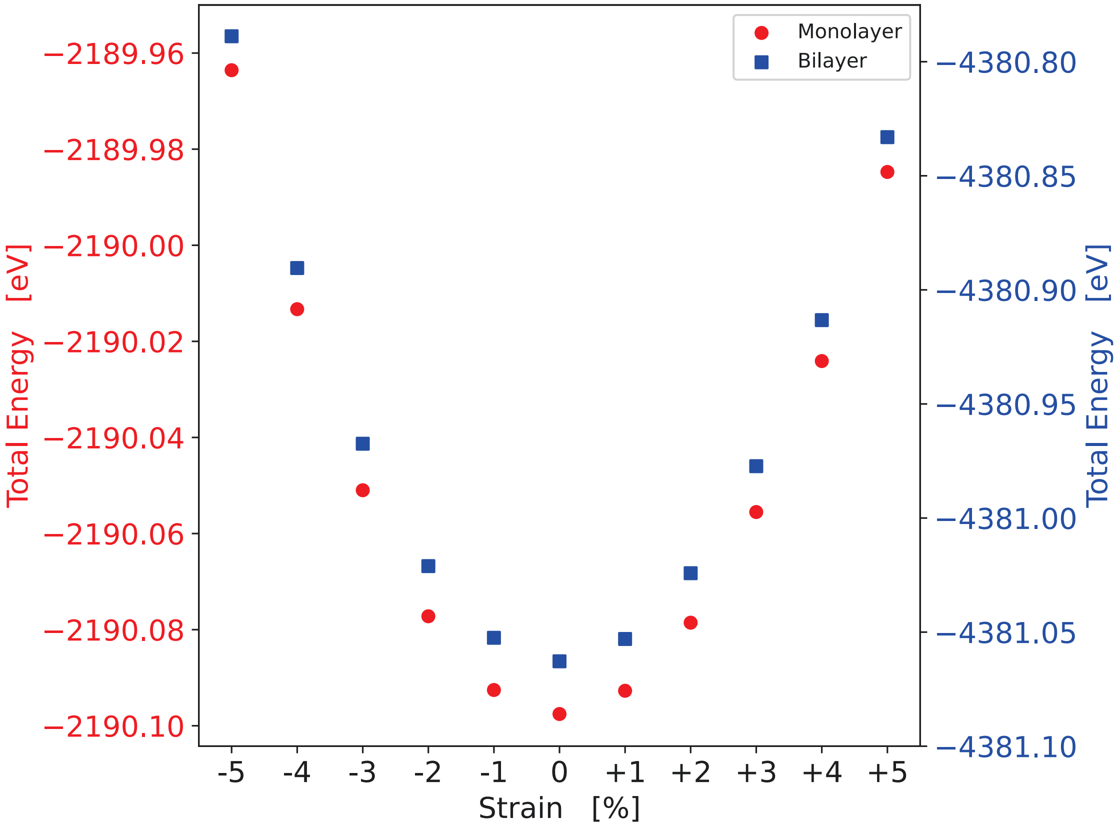

Figure D.2: The calculated total energy of Sr_2N monolayer (left axis) and bilayer (right axis) at tested strain values.

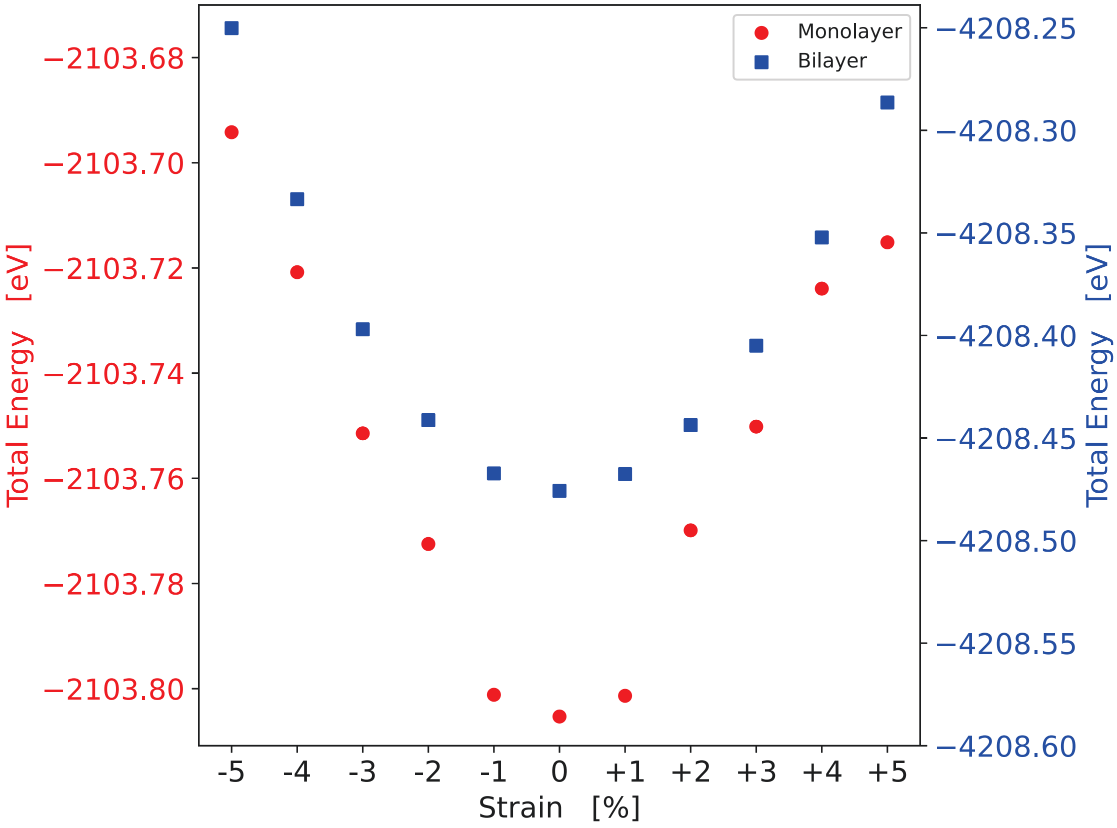

Figure D.3: The calculated total energy of Sr_2P monolayer (left axis) and bilayer (right axis) at tested strain values.

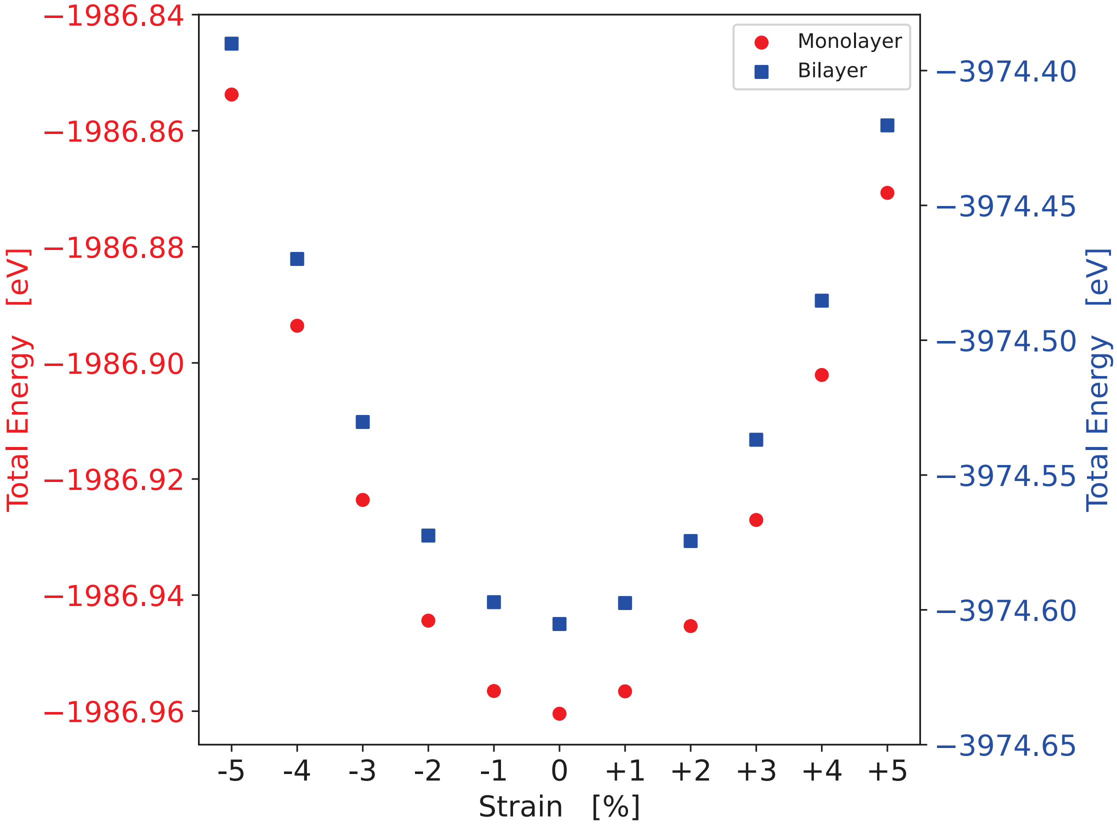

Figure D.4: The calculated total energy of Ba_2N monolayer (left axis) and bilayer (right axis) at tested strain values.

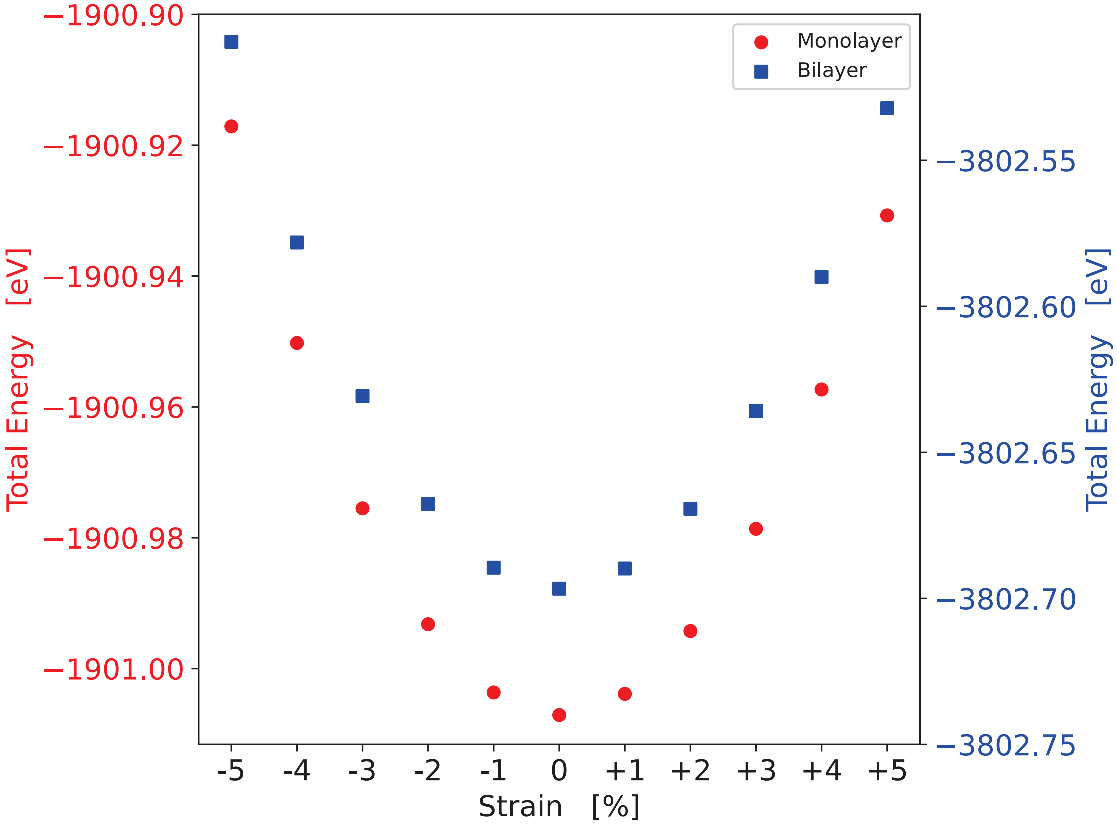

Figure D.5: The calculated total energy of Ba_2P monolayer (left axis) and bilayer (right axis) at tested strain values.

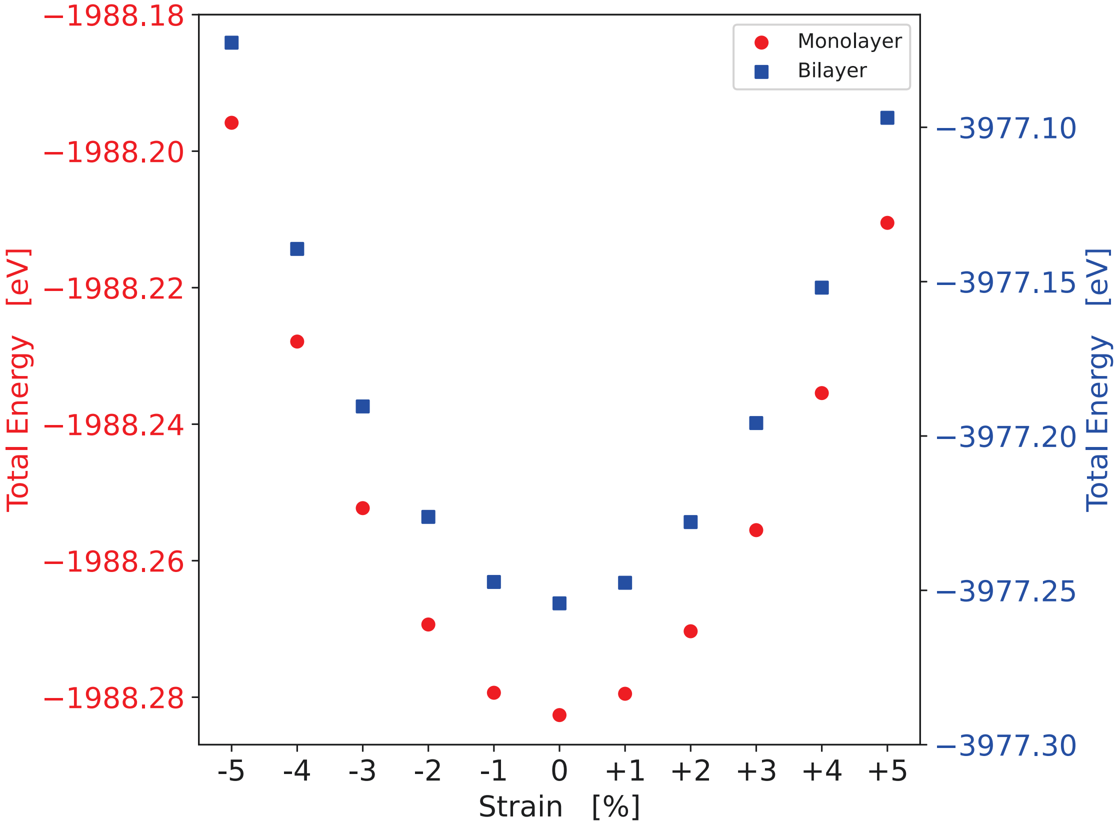

Figure D.6: The calculated total energy of Ba_2As monolayer (left axis) and bilayer (right axis) at tested strain values.

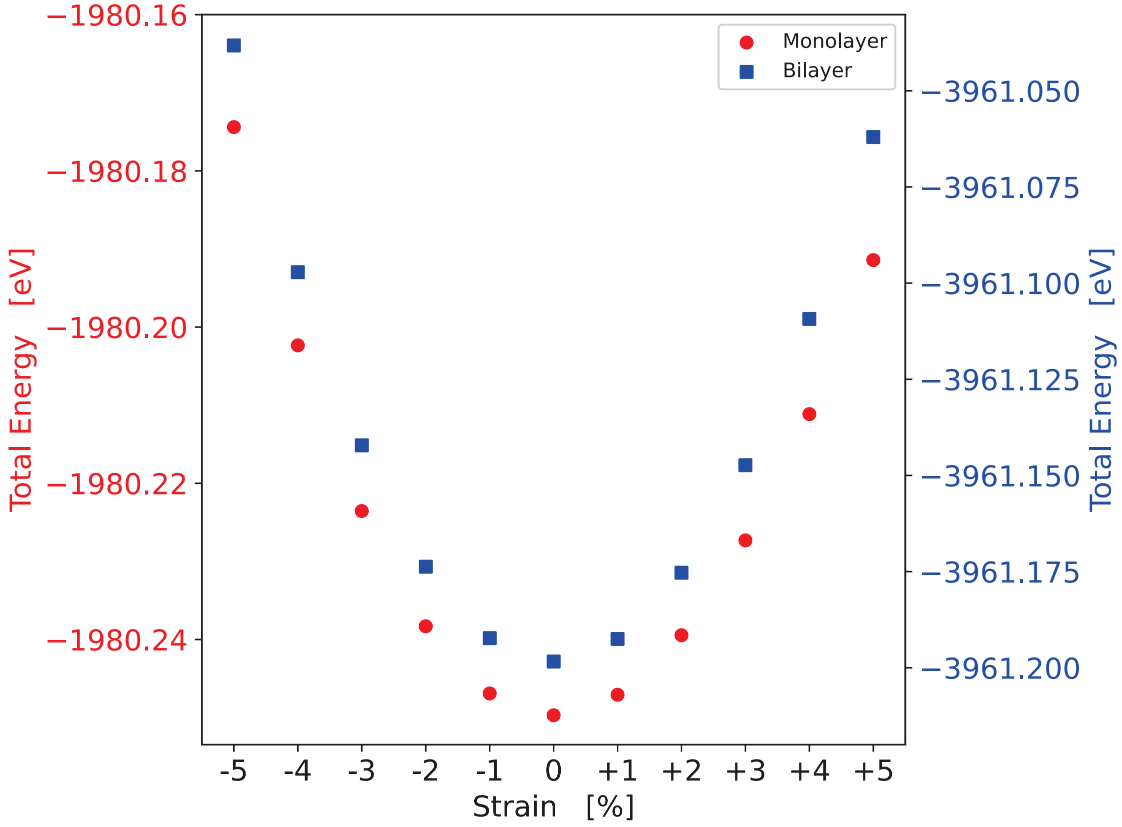

Figure D.7: The calculated total energy of Ba_2Sb monolayer (left axis) and bilayer (right axis) at tested strain values.